

AN ABSTRACT OF THE DISSERTATION OF

Izabela Gutowska for the degree of Doctor of Philosophy in Nuclear Engineering presented on June 18, 2015.

Title: Study on Depressurized Loss of Coolant Accident and its Mitigation Method Framework at Very High Temperature Gas Cooled Reactor

Abstract approved: _____

Brian G. Woods

Piotr Furmanski

To understand how a Depressurized Loss of Forced Convection (D-LOFC) initiated from a double-ended guillotine break may affect further operation of a High Temperature Gas Cooled Reactor (HTGR), thorough understanding of each specific stage of this event is required. Key considerations that need to be determined is the amount of air that will ingress into the reactor vessel during a Depressurized Conduction Cooldown (DCC) accident as well as the time scale of each events stage. Reactor components constructed of graphite will, at sufficiently high temperatures produce exothermic reactions in the presence of air while undergoing oxidation reaction. There is a danger that it may cause loss of core structural integrity via oxidation or surface corrosion. Thus, without any mitigation systems, this accident might result in exothermic chemical reactions of graphite and oxygen depending on the accident scenario and the design. Having

the knowledge on the amount of air inside the vessel one can investigate how to reduce air concentration via specifically designed mitigation system. The main idea of the applied mitigation method is to replace air in the core with buoyancy force by insertion of secondary gas: helium, nitrogen or argon into the reactor's lower plenum. This can help to mitigate graphite oxidation inside the reactor core by reducing air volume mass fraction in the reactor components and by lowering the core and lower plenum temperatures. This dissertation presents design framework for a secondary gas insertion system that will mitigate the potential core/structure damage during DCC event. Obtained results will serve as a guidelines for future design engineers while applying the concept to existing design.

©Copyright by Izabela Gutowska

June 18, 2015

All Rights Reserved

Study on Depressurized Loss of Coolant Accident and its Mitigation Method
Framework at Very High Temperature Gas Cooled Reactor

by

Izabela Gutowska

A DISSERTATION

submitted to

Oregon State University

in partial fulfillment of

the requirements for the

degree of

Doctor of Philosophy

Presented June 18, 2015

Commencement June, 2016

Doctor of Philosophy dissertation of Izabela Gutowska presented on June 18, 2015.

APPROVED:

Major Professor, representing Nuclear Engineering

Head of the Department of Nuclear Engineering and Radiation Health Physics

Dean of the Graduate School

I understand that my dissertation will become part of the permanent collection of Oregon State University libraries. My signature below authorizes release of my dissertation to any reader upon request.

Izabela Gutowska, Author

ACKNOWLEDGEMENTS

I wish to express my sincere thanks to my advisor, Dr Brian G. Woods and to my co-advisor Prof. Piotr Furmanski, whose encouragement, guidance and support from the initial to the final level of this research enabled me to develop an understanding of the subject and fulfill the doctoral program requirements.

I am also very grateful to Dr Kathryn Higley for providing me with the necessary support and facilities to provide me with the opportunity to study at Oregon State University.

The cooperation between Warsaw University of Technology and Oregon State University would not take place without the tremendous help of Prof. Tomasz Giebultowicz, Prof. Roman Domanski, and Prof. Konrad Swirski.

I would also like to express thanks to my committee members: Dr Quiao Wu, Dr Leah Minc and Prof. Andrzej Teodorczyk, for their continuous interest, comments and questions that have helped guide me during all stages of my work.

I take this opportunity to express gratitude to all of the Radiation Center Department and Institute of Heat Engineering faculty members for their help and support.

Most importantly, none of this would have been possible without the love and patience of my family. Heartiest thanks to my Mum, Barbara, and Dad, Adam, for being supportive whenever I was in Poland or in Oregon and encouraging me with their endless belief in my abilities. I am also very grateful to Magdalena Garlinska, who has always been an example of an excellent scientist and loving sister.

I offer my deepest gratefulness to my husband Piotr Kossakowski for his understanding and patience over the last several years and for motivating me to keep reaching for my goals.

Lastly, I offer my regards to all my OSU and WUT colleagues, who shared the PhD adventure with me or provided support in any respect during the completion of this dissertation.

TABLE OF CONTENTS

	<u>Page</u>
1. Introduction	1
1.1. Problem background	2
1.2. Motivation	4
1.3. Objectives.....	6
1.4. Assumptions and Limitations	7
1.5. Outline	9
2. Literature review.....	11
2.1. Development of gas cooled reactors technology	11
2.1.1 Current commercial designs	13
2.1.2. Research facilities.....	17
2.2. Initial DCC studies	18
2.3. DCC mitigation concepts.....	25
2.4. Graphite oxidation	28
2.5. Computational methods applied to DCC analysis.....	36
2.6. CFD model validation and verification methodology.....	40
3. High Temperature Test Facility	47
3.1. Scaling analysis.....	47
3.2. HTTF design.....	48
4. DCC theory and physics	55
4.1. Depressurization	56
4.2. Lock exchange flow.....	59
5. CFD modeling	63
5.1. Governing Equations	63
5.2. Solver settings	64
5.3. Geometry	66

TABLE OF CONTENTS (CONTINUED)

	<u>Page</u>
5.4. Initial and boundary conditions.....	67
5.5. Porous body model	70
5.6. Mesh model and refinement.....	80
5.7. Turbulence sensitivity analysis	88
5.7.1. K-Epsilon Models	90
5.7.2. K-Omega Models	91
5.7.3. Menter SST	92
5.7.4. Turbulence sensitivity study results	92
6. CFD simulations results	100
6.1. Depressurization	100
6.2. Lock exchange flow –porous bodies approach.....	115
6.3 Lock exchange flow - detailed lower plenum model.....	124
6.4. Mitigation concept.....	130
6.4.1. Helium injection.....	131
6.4.2. Nitrogen injection	136
6.4.3. Argon injection.....	138
6.5. Comparative study of considered mitigation methods	143
7. D-LOFC mitigation method implementation	146
8. Conclusions	149
9. Future work	152
References	153

LIST OF FIGURES

<u>Figure</u>	<u>Page</u>
Figure 1 Operational temperatures in various industries versus coolant temperatures in different nuclear reactor designs (taken from [25] with no changes).....	2
Figure 2 Generations of gas cooled reactors.	11
Figure 3 Scheme of GT-MHR (taken from [60] with no changes).....	14
Figure 4 MHTGR module. [taken from 52 with no changes]	16
Figure 5 Sketch of the typical horizontal gravity current front propagation. [50]	21
Figure 6 Simple analysis of the counter-current flow.....	22
Figure 7 Flow depth of heavy current as a function of the density ratio (taken from [44] with no changes).....	23
Figure 8 Conceptual helium injection port in the schematic view of VHTR reactor vessel.....	26
Figure 9 Root causes of air ingress accident. [58].....	29
Figure 10 Graphite oxidation regimes. The upper graph shows the change in rate of the carbon gasification reaction with temperature. The lower chart shows the concentration changes of reactant gas in the graphite, varying with the rate controlling zone [taken from Marsh (1989) with no changes].....	31
Figure 11 Geometry of the HTTF reactor core	50
Figure 12 Helium flow path in HTTF.	51
Figure 13 HTTF core block and core block cross section.	52
Figure 14 HTTF lower plenum channel and support posts arrangement.	52
Figure 15 D-LOFC flow path in VHTR.	55
Figure 16 Pressure changes in the HTTF vessel (blue line) and cavity (green line) from Matlab simulation	59
Figure 17 Gravity current flow with nomenclature used in the text.....	60
Figure 18 Stratified flow time scale and velocities as a function of normalized current depth.	62
Figure 19 CFD geometry model.....	67
Figure 20 Core and vessel temperatures during D-LOFC with RCCS Cooldown (left) and without operating RCCS (right). [69].....	68
Figure 21 Placement of the lower plenum secondary gas injections, schematic view.	70

LIST OF FIGURES (CONTINUED)

<u>Figure</u>	<u>Page</u>
Figure 22 HTTF core internal flow patch.	73
Figure 23 Schematic view of the staggered tube arrangement. [96].....	75
Figure 24 Fitting curve for the core porous body model implementation, Moody diagram.....	77
Figure 25 Fitting curve for the lower plenum porous body model implementation, Moody diagram.....	77
Figure 26 Fitting curve for the lower plenum porous body model implementation, Zakauskas diagram.....	78
Figure 27 Friction factor (f) for the use in vertical channel flow arrangement.	79
Figure 28 Friction factor (f) and the correction factor (Z) for the use for staggered tube arrangement.	79
Figure 30 Detailed volume mesh on the selected domains (medium mesh).	84
Figure 31 Surface average air mass fraction at Rake plane section for different meshes along with the extrapolate solution.....	85
Figure 32 Extrapolated error between applied grids.....	86
Figure 33 Fine solution uncertainty bands.	86
Figure 36 Volume average mass fraction of air in the core, turbulence models comparison.....	94
Figure 37 Volume average mass fraction of air in the LP, turbulence models comparison.....	94
Figure 38 Surface average mass fraction of air at Rake cross section, turbulence models comparison.....	95
Figure 39 Surface average mass fraction of air at break cross section, turbulence models comparison.....	95
Figure 40 X-Y velocity profile at Rake cross section, Standard K-Epsilon model.	98
Figure 41 X-Y velocity profile at Rake cross section, Laminar model.	98
Figure 42 X-Y velocity profile at Rake cross section, SST K-Omega model.	99
Figure 43 X-Y velocity profile at Rake cross section, Wilcox K-Omega model.....	99
Figure 44 X-Y velocity profile at Rake cross section, Realizable K-Epsilon model.	99
Figure 45 Placement of the depressurization line-probe (centerline).....	101
Figure 46 Depressurization pressure solution, $t = 0.7$ msec.....	102

LIST OF FIGURES (CONTINUED)

<u>Figure</u>	<u>Page</u>
Figure 47 Depressurization pressure solution, $t = 385$ msec.....	103
Figure 48 Depressurization velocity solution, $t = 385$ msec.....	103
Figure 49 Density distribution during depressurization phase, at $t=385$ msec....	104
Figure 50 Depressurization pressure solution, $t = 694$ msec.....	104
Figure 51 Depressurization velocity solution, $t = 694$ msec.....	105
Figure 52 Temperature distribution during depressurization phase, at $t=694$ msec.....	105
Figure 53 Depressurization pressure solution, $t = 826$ msec.....	106
Figure 54 Depressurization velocity solution, $t = 826$ msec.....	107
Figure 55 Depressurization pressure solution, $t = 981$ msec.....	108
Figure 56 Depressurization velocity solution, $t = 981$ msec.....	108
Figure 57 Depressurization air mass fraction solution, $t=981$ msec.....	109
Figure 58 Air mass fraction distribution during depressurization phase, at $t=981$ msec.....	109
Figure 59 Depressurization pressure solution, $t = 1.58$ sec.....	110
Figure 60 Depressurization velocity solution, $t = 1.58$ sec.....	111
Figure 61 Depressurization air mass fraction solution, $t = 1.58$ sec.....	111
Figure 62 Depressurization pressure solution, $t = 1.78$ sec.....	112
Figure 63 Depressurization velocity solution, $t = 1.78$ sec.....	113
Figure 64 Volume average of absolute pressure in the entire reactor system during blowdown simulation.....	114
Figure 65 Onset of the exchange flow, air mass fraction.....	115
Figure 66 Stratified flow velocity magnitude distribution in the coaxial pipe at 1.0 s from the beginning of the transient.....	116
Figure 67 Velocity and density distributions at Rake section.....	116
Figure 68 Exchange flow streamlines at the end of simulation, $t=30$ sec.....	117
Figure 69 Stratified flow time scale as a function of the normalized current depth with reference to the stratified flow time scale obtained from CFD results, marked with the dashed line.....	119
Figure 70 Volume average air mass fractions in different zones.....	120
Figure 71 Comparison of volume average air mass fractions in the lower plenum in the HTTF and MHTGR.....	121

LIST OF FIGURES (CONTINUED)

<u>Figure</u>	<u>Page</u>
Figure 72 X-Y velocity profile at Rake cross section at 20 sec from the beginning of the transient.	122
Figure 73 Density (left) and temperature (right) distribution in the lower plenum at t=30 sec, baseline study.	123
Figure 74 Onset of Stage 2 stratified flow indicated by volume average mass fraction of air in the core as a function of time.	124
Figure 75 Sequence of lock-exchange flow events in the detailed lower plenum geometry simulation: figure a) shows cold plume propagation at 1.5 sec from the beginning of the transient, figure b) presents progress 5 sec later) while final stage at 35 sec is shown in figure c).	126
Figure 76 Comparison of volume average air mass fractions in the lower plenum in the baseline HTTF simulation with porous domain approach, MHTGR and detailed lower plenum simulation.	127
Figure 77 X-Y velocity profile at Rake cross section in detailed lower plenum model.	127
Figure 78 Detailed lower plenum cross sections, used to investigate velocity and air concentration distributions.	128
Figure 79 Volume average mass fraction of air as a function of time in the Lower Plenum.	133
Figure 80 Distribution of mass fraction of air in the baseline model and in the case with helium injection, $v_{inj}=2$ m/s, t=30 sec.	134
Figure 81 Mass fraction of helium at the lower plenum - Core interface ($v_{inj} = 2$ m/s, t=35 s).	134
Figure 82 Comparison of volume average mass fraction of air in the LP between helium, LP side injection with D=0.1 m and D=0.05m at v=2 m/s.	135
Figure 83 Distribution of mass fraction of air in the baseline model and in the case with dual argon injection, t=30 sec.	135
Figure 84 Comparison of volume average mass fraction of air in the LP between helium and nitrogen, LP side injection at v=2 m/s.	137
Figure 85 Distribution of mass fraction of air in the baseline model and in the case with side nitrogen injection, $v_{inj}=2.0$ m/s, t=30 sec.	137

LIST OF FIGURES (CONTINUED)

<u>Figure</u>	<u>Page</u>
Figure 86 Comparison of volume average mass fraction of air in the LP between argon and nitrogen, LP side injection at $v=2$ m/s.	138
Figure 87 Comparison of volume average mass fraction of air in the LP between argon, LP side injection at $v=2$ m/s and LP bottom injection at $v=1$ m/s and 2 m/s.	139
Figure 88 Comparison of volume average mass fraction of air in the LP between argon, LP bottom injection, LP side injection and LP bottom & side injection simultaneously at $v=1$ m/s.	140
Figure 89 Distribution of mass fraction of air in the baseline model and in the cases with argon injection, $v_{inj}=2.0$ m/s, $t=30$ sec.	141
Figure 90 Argon flow streamlines indicating mixing with air (mass fraction of air), top and side views, $t=30$ sec.	142
Figure 91 Argon flow streamline, velocity distribution, side view, $t=30$ sec.	143
Figure 92 Comparison of the efficiency of the analyzed mitigation concepts.	144
Figure 93 Cross sections placement for the local surface maximum analysis.	145
Figure 94 Maximum local surface air mass fraction, comparison between mitigation concepts.	145
Figure 95 Comparison of mitigation system efficiency (dual argon injection) after closing the injection valve at 30 sec.	147

LIST OF TABLES

<u>Table</u>	<u>Page</u>
Table 1 The main properties of the two main types of the nuclear graphite.	33
Table 2 Overall channel distribution in the particular HTTF segments.	53
Table 3 Gas concentration instrumentation (GCI) placement and number.	54
Table 4 Depressurization case initial conditions.	69
Table 5 Details of porous body modeling: lower plenum and reactor core.	78
Table 6 MHTGR porous model parameters.	80
Table 7 Face validity and volume change statistics	83
Table 8 Mesh sensitivity study details.	83
Table 9 Details of cell quantity and placement, medium mesh, HTTF.	87
Table 10 Details of cell quantity and placement, medium mesh, MHTGR.	88
Table 11 Sequence of events in lock-exchange study – baseline model.	118
Table 12 Velocity and air concentration distributions at particular lower plenum cross sections in the case with detailed lower plenum geometry modeled.	129
Table 13 Details of the mitigation method sensitivity study simulations.	131
Table 14 Approximate times for air current to reach instrumentation Rake.	132

Abbreviations

CFD	Computational Fluid Dynamics
D-LOFC	Depressurized Loss of Forced Convection
DCC	Depressurized Conduction Cooldown
DEGB	Double Ended Guillotine Break
DOE	US Department of Energy
EM2	Energy Multiplier Module
GCR	Gas-Cooled Reactor
GT-MHR	Gas Turbine-Modular Helium Reactor
HTGR	High Temperature Gas Cooled Reactor
HTR-PM	High Temperature Pebble Bed Modular Nuclear Reactor
HTTF	High Temperature Test Facility
INL	Idaho National Laboratory
JAERI	Japan Atomic Energy Research Institute
LOFC	Loss of Forced Convection
MCSS	Metallic Core Support Structure
MHTGR	Modular High Temperature Gas Cooled Reactor
NGNP	Next Generation Nuclear Plant
OSU	Oregon State University
PBMR	Pebble Bed Modular Reactor
P-LOFC	Pressurized Loss of Forced Convection
PCC	Pressurized Conduction Cooldown
PIRT	Phenomenon Identification and Ranking Table
RCCS	Reactor Cavity Cooling System
RPV	Reactor Pressure Vessel
SCAD	Sustained Counter Current Air Diffusion
THTR	Thorium High-Temperature Reactor
TRISO	Tristructural-Isotropic Fuel
VHTR	Very High Temperature Gas Reactor

Nomenclature

A - linear pre-exponential coefficient

A_{brk} is the break cross section area

C_{ij} - tensor, internal resistance factor

C^μ - dimensionless constant = 0.09

D - diameter of the hot duct

D_{ij} - tensor, viscous resistance factor

d - depth of the channel

D_v - volumetric hydraulic diameter

E - effective activation energy [J/mol]

e_g - specific internal energy

F_h - modified Froude number

G_{max} - maximum mass flux

g - gravitational constant

g' - modified gravitational constant

h_g - gas enthalpy

I - turbulent intensity

k - turbulent kinetic energy

k_o - oxidation rate constant [1/s]

L - length of the separated hot duct on the reactor vessel side

l - mixing length

\dot{m}_{Brk} is the mass flow rate through the break

$M_{g,vessel}$ is the mass of gas in the vessel

N - number of the tube rows in the direction of the flow

P - pressure [Pa]

P_i - internal resistance coefficient

P_v - viscous resistance coefficient

p_r - pressure coefficient

Re - Reynolds number

S_i - source term for the i th (x,y,z) momentum equation

t - time [s]

u – velocity [m/s]

u_H - helium velocity flowing counter-current to the cold air plume

u_{LP} - helium velocity approaching the cold plume

V - volume

v_j - velocity component in the j th (x,y,z) direction

v_{mag} - velocity magnitude

v - superficial velocity through the medium (actual velocity times volume porosity)

Z - correction factor depending on the array arrangement

ε - eddy diffusivity

ϑ - is the kinematic viscosity (momentum diffusivity)

v_g - specific volume

γ – density ratio

γ_g - ratio of the specific heats

γ^* refers to the Boussinesq critical density ratio

α_{brk} is the orientation of the break with respect to the vertical

α - porous region permeability ($D_{ii} = \frac{1}{\alpha}$).

ρ - density

μ – dynamic viscosity

1. Introduction

Approximately one third of the global primary energy consumption is used for electricity generation; around 55% is consumed to produce hot water, steam and heat for households and industrial applications, and the remaining 15% is used in transportation. The contribution of nuclear energy in the overall electricity production share is around 11% (2012). This means that significant potential exists for nuclear power to not only cover the continuous electricity demand by increasing its share in the global electricity market but also to follow the tendency for highly efficient cogenerated, heat and power production. [50, 32, 25]

The U.S. Department of Energy (DOE) program to develop the Very High Temperature Gas Cooled Reactor (VHTR) with a helium coolant is a technological cornerstone for advanced applications that further expands the safe use of nuclear energy. A new program for future nuclear energy systems, Generation IV (GENIV), has been created in an effort to provide next-generation technologies that will compete in all markets with the most cost-effective technologies expected to be available over the next three decades [24, 23]

Gas-cooled reactor systems have several fundamental characteristic features that distinguish them from other types of reactors and provide significant operational advantages. In particular, the fuel is in the form of small ceramic-coated particles capable of operating in very high temperatures; the moderator is solid graphite, and the coolant is neutronicly inert helium or carbon dioxide. [24, 23, 25]

VHTR are designed with average coolant outlet temperatures above 900°C or operational fuel temperatures above 1250°C. These designs provide the potential for increased energy conversion efficiency and for high-temperature process heat

applications, such as coal gasification or thermochemical hydrogen production (Figure 1). [31]

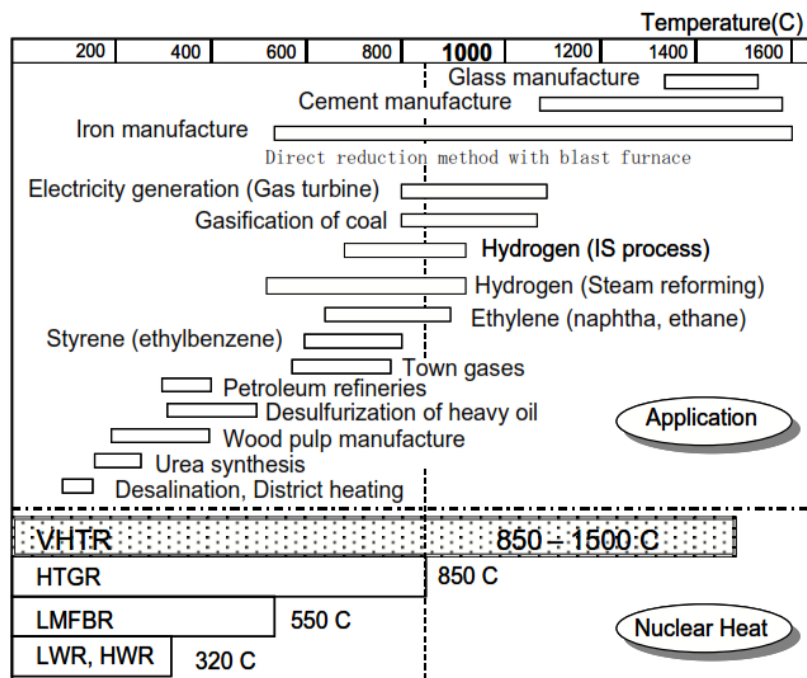


Figure 1 Operational temperatures in various industries versus coolant temperatures in different nuclear reactor designs (taken from [25] with no changes).

One unique characteristic of the VHTR is its ability to cool the reactor entirely by passive heat transfer mechanisms following postulated accidents. Passive removal of residual heat through the reactor vessel surface to the cavity cooling system occurs by radiation, convection and thermal conductivity without fuel temperature exceeding 1600 °C, in particular, in the case of forced cooling. [52]

1.1. Problem background

Nuclear safety undergoes constant examination. It is essential for the development of the safety analysis of GENIV technology to create the Phenomena Identification and Ranking Table (PIRT), and to establish the event classification and acceptance criteria for the VHTR. The air ingress event following a VHTR depressurization

is ranked as important to core safety by the United States Nuclear Regulatory Commission. [74]

In the case of the D-LOFC (Depressurized Loss of Forced Convection, also named DCC – Depressurized Conduction Cooling), following a break in the system pressure boundary, the system will depressurize releasing the helium coolant into the reactor cavity. The reactor cavity will nominally be filled with air prior to any break. For a large enough break with a high enough rate of depressurization, air ingress into the reactor core may occur. The most important concern coupled with air ingress is the graphite structure weakening that can lead to core structure degradation and to fission product release if the core is exposed to oxygen for an extended period of time. [90]

There are a number of uncertainties when determining the extent and timing of air ingress accident in the VHTR. One of the questions concerns the air movement into the lower plenum after the system depressurizes to confinement pressure [94]. Early research focused on the air ingress scenario dominated only by molecular diffusion. Recent studies prove that the main air ingress stage after the double ended guillotine break (DEGB) is the stratified flow phase (duct exchange flow). For instance, if the break were to occur in the inlet-outlet duct, lock-exchange flow could occur due to the density differences between the cooler air in the cavity and the hotter helium exiting the vessel. This exchange flow can significantly reduce the time needed to allow a significant amount of air to enter the vessel itself. In the study conducted by Oh et al. (2011), it has been proved by computational simulation, as well as by analytical models, that molecular diffusion is over 600 times longer than the density driven exchange flow. In case of thermally stratified flow, diffusion process is 2000 times longer [66, 39]. It is complicated to numerically calculate counter current natural circulation flow and experimental

data may be needed for codes validation purpose. This phenomenon is therefore ranked of high importance and medium knowledge [90]. There are also uncertainties as to the design of the reactor cavity gas which would drive the amount of oxygen introduced into the core. [89]

1.2. Motivation

The Next Generation Nuclear Power Plant (NGNP) Methods Technical Program Plan first described the possibility of density-driven stratified air ingress into the high temperature reactor after the D-LOFC occurs.

The United States Nuclear Regulatory Commission has identified this event in the NGNP Phenomena Identification and Ranking Tables (PIRTs) and has stated that:

“The most significant phenomena (those assigned an importance rank of “high” with the corresponding knowledge level of “low” or “medium”) in the thermal-fluids area include primary system heat transport phenomena which impact fuel and component temperatures, reactor physics phenomena which impact peak fuel temperatures in many events, and postulated air ingress accidents that, however unlikely, could lead to major core and core support damage.” [89]

However, the NGNP Methods Technical Program Plan describes the DCC event scenario in three accident phases, which are blowdown, molecular diffusion and natural convection. It omits the important exchange flow stage. Each stage of the D-LOFC event: diffusion, stratification and natural convection are viable mechanisms for investigation of air ingress into the system over long time scales. [74, 75]

As the D-LOFC event proceeds in time, peak core temperature will be reached. Reactor components constructed of graphite will, at high temperatures produce

exothermic reactions in the presence of oxygen. High potential of losing core structural integrity via oxidation or surface corrosion exist.[47] If core support columns placed in the lower plenum would structurally fail, it will not only incur system degradation but will also hinder the ability to remove heat from the core by natural circulation because of additional flow restrictions. Thus, without mitigation features, this accident might lead to severe exothermic chemical reactions of graphite and oxygen depending on the accident scenario and the design. In the research done by Haque (2008), it is shown that delay of air ingress to the reactor core will reduce graphite oxidation within its structures. [26]

There are several mitigation concepts presented in the literature, but none of them has been selected as a standard. Those concepts are described in the Literature Review section. The general idea is to replace the air in the core by secondary helium injection [58]. There are still a number of questions related to the effectiveness of these mitigation concepts, including the placement of the injection and injection parameters such as velocity or temperature.

Another important feature of this phenomenon is the presence of a time varying air ingress to the reactor vessel that creates a scenario that is not well modeled by existing system codes such as RELAP. Thus proper CFD analysis is required in the studies that take into account the air ingress scenario in the VHTR.

CFD modeling has been used in nuclear reactor studies for over 30 years. Increased interest in CFD tools stems not only from the improving computing power availability but also from the need to properly anticipate and reduce the computational uncertainty of such phenomena as: boron mixing, two phase flow, etc. Available CFD tools allow one to optimize the design process, thereby reducing the costs of the necessary on site tests and experiments. On the other hand, the total reliance on the results from numerical analysis is only possible if

the analyzed model or physical phenomena were introduced in the source code on the basis of validated and verified data. Even though, there is still a margin of error that is bounded with each numerical analysis. Those errors are bounded with uncertainties in the formulation of the model physics, geometry simplifications, spatial and temporal discretization of the fluid domain, truncation error, iterative convergence error or computer round-off error. The full-scale, three dimensional model of the nuclear reactor vessel requires advanced computing power to introduce appropriate spatial discretization of the model and also to run the simulation. Actual computational time in the context of available computing power should be taken into account. Thus, CFD simulations of nuclear reactors require engineering judgment on simplifications and optimization of the analysis.

1.3. Objectives

Aspects of the safety of nuclear power plants and associated systems is one of the major issues in every discussion on the advantages and risk of the nuclear energy. The crucial point is to improve the understanding of the existing accident scenarios and develop efficient mitigation concepts.

To understand how a D-LOFC initiated from a double-ended guillotine break may affect further operation of a high temperature gas cooled reactor, one needs to thoroughly understand each specific stage of this event. Studies on the accident should include creation of appropriate numerical models of depressurization and lock exchange phenomena that will be verified for further validation with experimental data. Key considerations that need to be determined are the time extent of the analyzed event stages and the amount of air that will ingress into the reactor vessel during a DCC accident (or respectively identification of the amount of helium leaving the vessel). Having the knowledge on the amount of air inside the lower plenum and reactor core one can investigate how to reduce air

concentration via secondary helium injection. The main idea of the helium secondary insertion method is to replace air in the core with buoyancy force. This can help to mitigate graphite oxidation damage in the reactor core and support structures. It is also important that examined time scale of D-LOFC event is crucial to evaluate operator response time for such accident. To fulfill objective statements the following research will be performed:

1. Preliminary investigation on the physics of the D-LOFC in the VHTR: depressurization and lock-exchange flow (analytical models).
2. Development of advanced air ingress thermalhydraulic models of HTTF (STAR-CCM+ code), that will include sensitivity studies on the turbulence modeling and mesh refinement.
3. Thermalhydraulic model of air ingress mitigation concept.
4. Quantitative and qualitative analysis of the obtained results in the view of phenomena modeling verification in the CFD tool and of recommendations for:
 - numerical modeling of postulated D-LOFC scenarios in the VHTR,
 - numerical modeling of potential D-LOFC mitigation system,
 - data for validation of computer codes (CFD and system analysis codes).

1.4. Assumptions and Limitations

Air ingress accident scenario in the MHTGR, even if possible to occur with very low probability, has always raised significant concerns. The scenario considered in this work is with extremely low probability and assumes a complete double guillotine break of the concentric duct connecting the reactor vessel and steam generator. Even though, such case might not seem credible to become initiated without any influence on the reactor vessel internal components, it can serve as an

upper margin for the potential loss of forced cooling scenarios, setting bounding consequences [68, 69]. Therefore it was assumed, that due to the catastrophic failure of the cross duct, it will remain fully open for the air to enter reactor flow paths.

General Atomics MHTGR was used in this work as a reference design (prototype). All calculations concerning air ingress mitigation study were made with reference to the HTTF. Only baseline model for the exchange flow simulation was run for both: prototype and scaled test facility. Once comparable results were obtained for the baseline scenario it was decided to run the sensitivity study on mitigation method only on the scaled model to save the computational time.

Considering limitations that arise with using specific computational tools and limited computational power it has to be underlined that CFD solver used in this analysis has trouble obtaining fully converged solutions for the large pressure difference between the reactor and the confinement in the blowdown phase in the reasonable computational time. Therefore, the CFD grid independence study and turbulence modeling were conducted at the pressure equalization in the system, following the depressurization stage. The STAR CCM+ baseline results on the exchange flow can therefore be applied to predict the air ingress behavior because of the density driven stratified flow, buoyant flow by temperature gradients, and hydraulic flow interrupted by system geometry.

Another constrains arise from the simplifications applied in the CFD models. The following simplifications were applied to increase the efficiency of calculations without losing significant solution data at the same time: constant temperatures in the modeled regions (no conjugate heat transfer modeled), porous body implemented in the lower plenum and core regions (in the core region, bypass flow

is not included in the model), geometry is simplified to capture the main fluid flow paths (for instance, no instrumentation controls modeled) and finally in the exchange flow simulation, the initial condition is 100% of air the confinement region. All these simplifications are justified in the CFD modeling section (ref. chapter 5. CFD modeling).

1.5. Outline

The remainder of this document will present air ingress phenomena in the VHTR reactor as a consequence of DEGB and proposed mitigation method concept to meet the objectives of this work.

- Chapter 2 contains a literature review on the development of gas cooled reactors along with a survey of current commercial designs and research facilities. Included herein are also a revision of previous DCC studies, proposed D-LOFC mitigation concepts, nuclear graphite oxidation research along with a literature review of computational methods applied to DCC analyses and CFD model validation methodology.
- Chapter 3 discusses the HTTF design and applied scaling methodology.
- Chapter 4 contains details of analytic models of depressurization and exchange flow phases.
- Chapter 5 details the CFD modeling: governing equations, solver settings, applied geometry, initial and boundary conditions, porous body model and results from grid independence study and turbulence sensitivity analysis.
- Chapter 6 shows results obtained from the CFD analyses for depressurization, lock exchange flow and mitigation concepts. It ends with the comparative study of the considered mitigation methods.
- Next chapter (chapter 7) presents brief discussion on the scope and limitations of mitigation concept implementation.

- Rest of the document contains study conclusions (chapter 8), suggestions for future work (chapter 9) and lists dissertation bibliography.

2. Literature review

2.1. Development of gas cooled reactors technology

Interest in the HTGR continues today, with the advancement of technologies in the United States, Japan, China, and South Africa. The goal was to obtain high gas temperatures and thus more efficient electricity production, coupled with the vision of leading to broader applications of nuclear energy such as providing industrial process heat. That motivated the development of the high temperature gas cooled reactor with its characteristic reactor core of graphite moderator and ceramic fuel and its use of a gas as coolant. The chart below shows the sequence of gas cooled reactors development (Figure 2). [50]

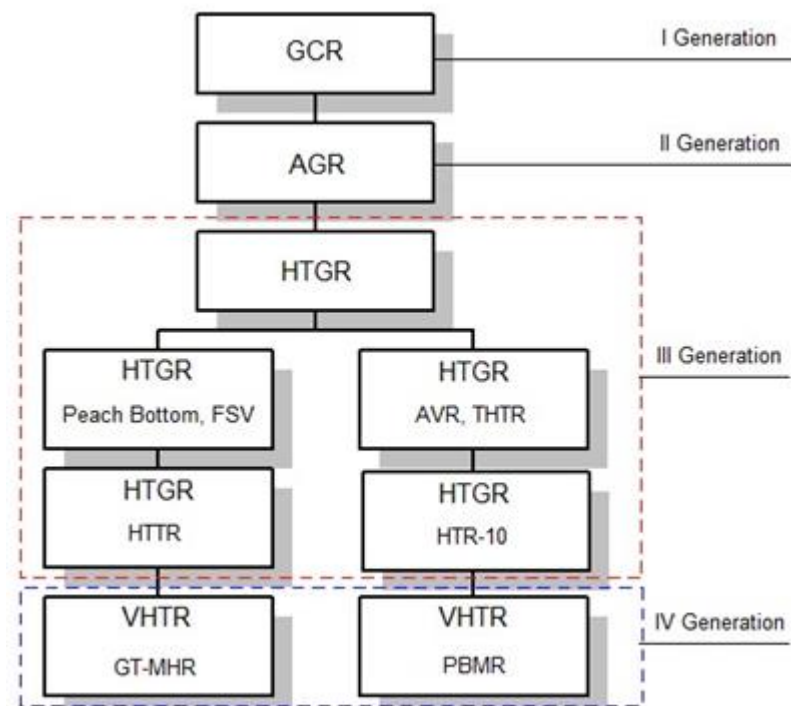


Figure 2 Generations of gas cooled reactors.

Gas cooled reactors have had a long and varied history which dates back to the very early days of nuclear energy development. Most of the early

development centered on low temperature systems using a graphite moderator, metal clad metallic fuel and carbon dioxide coolant. In 1956, the Calder Hall in England, world's first industrial nuclear power unit was launched. This was the beginning of the development of GCR (Gas-Cooled Reactor). GCR reactors are commonly called "Magnox". This name derives from the material (Magnox - magnesium alloy), from which fuel cladding is made. The fuel in these reactors is metallic uranium, and the coolant carbon dioxide (CO₂). These reactors were the first generation of nuclear power gaseous reactors. In total, 26 blocks of GCR were built (between 1956-1968) in the power range 60-550 MWe. [50]

The second generation of gaseous reactors are AGR (Advanced Gas-Cooled Reactor). There are five examples of power plants with such units, built in late 70's to early 80's of last century in Great Britain: Dungeness B, Hinkley Point B, Hartlepool, Hunterston B, Heysham. Each of these plants produce power around 1250 MW and have related operational parameters. Disability to obtain satisfactory high-temperature of coolant in the GCR was solved by using different materials in AGR. In AGR reactors, the fuel is low enriched uranium dioxide (UO₂), the graphite moderator is used, coolant is carbon dioxide (CO₂) and fuel elements and claddings are made of stainless steel or zirconium alloys. The outlet temperature of the reactor is 675 °C and the pressure in the primary circuit 34 bars. [78]

There was no possibility of further increase the temperature of carbon dioxide, so development of GCR and AGR reactors was not continued. As a new solution, United Kingdom initiated a program of high temperature reactor HTGR in the late 50's and 60's. New idea was the combination of helium coolant and graphite moderator. The graphite moderator provided enhanced neutronic and thermal efficiencies. Nowadays seven high temperature gas reactor plants have been built

and operated. The first was the Dragon reactor in the United Kingdom with nominal power of 20 MWt. Thanks to reactors operated in United States, the helium gas has a significant technical base due to the experience gained from the 40 MWe Peach Bottom and 330 MWe Fort St. Vrain reactors, and from Germany, which built and operated the 15-MWe AVR and the 300-MWe thorium high-temperature reactor (THTR) power plants. The German AVR operated at the 900°C level for several years. The U.S. experience was based on reactors designed by General Atomics (GA) and involved coolant temperatures below 750°C. The AVR, THTR, Peach Bottom and Fort St. Vrain all used fuel containing thorium in different forms (i.e., carbides, oxides, thorium particles) and mixtures with highly enriched uranium. [78]

2.1.1 Current commercial designs

Next generation nuclear power (NGNP) plan consider modular designs that incorporate passive safety features. The VHTR is one of the six reactor concepts under evaluation by Gen IV. The VHTR is a thermal design that will be able to operate at temperatures at or above 1000°C, to enable production of hydrogen through thermo-chemical reactions for splitting water. The reactor core may be either a prismatic graphite block type core or a pebble bed. [78]

One idea was developed by an international consortium led by the South African utility, ESKOM. They designed high temperature reactor using a helium coolant with a direct gas turbine power cycle (i.e., Brayton cycle). This technology bases on the high-temperature reactor (HTR) German designs using circulating graphite pebbles containing ceramic-coated oxide fuel micro particles. The design is referred to as the Pebble Bed Modular reactor (PBMR). [50]

The Japan Institute that performs research on HTGR is called Japan Atomic Energy Research Institute (JAERI). JAERI carrying out a research program on the design and development of the Gas Turbine High Temperature Reactor of 300 MW_e (600MW_{th}), called the GTHTR300. Basic characteristic of this reactor is that it is helium cooled, graphite-moderated and based on pin-in-block fuel element. The GTHTR300 has operated at 850°C core outlet temperatures, while the inlet temperature is around 587°C. Coolant pressure and flow rate are respectively: 7 MPa and 438 kg/s. The fuel assembly is a so called pin-in-block type, which is composed of fuel rods and a hexagonal fuel block. [41]

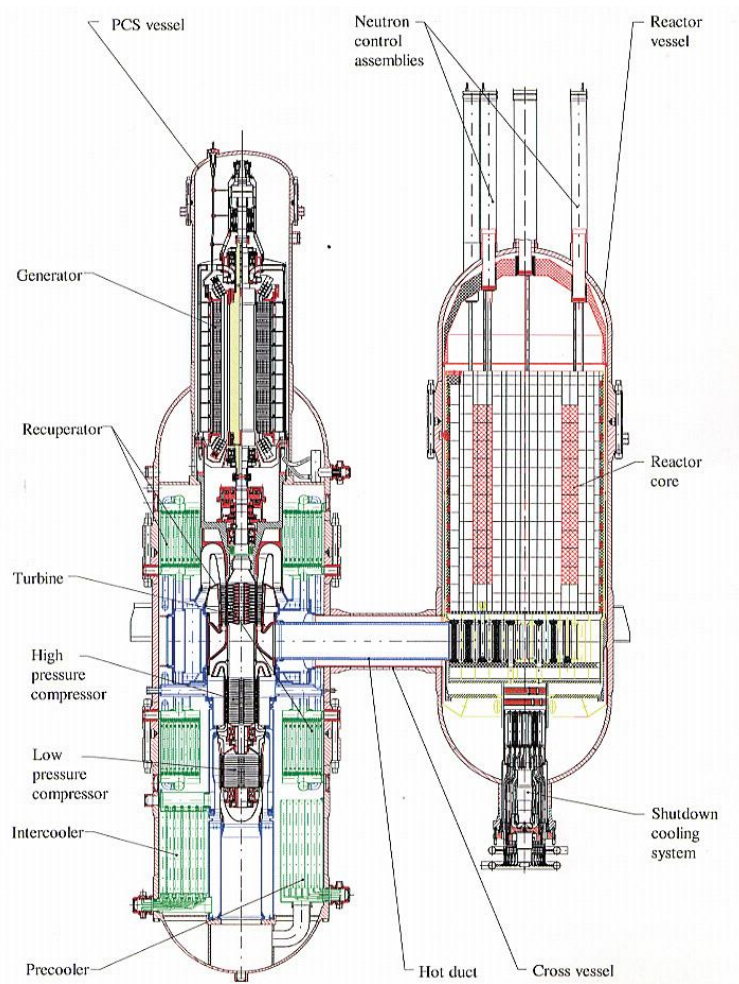


Figure 3 Scheme of GT-MHR (taken from [60] with no changes)

Gas turbine – modular helium reactor (GT-MHR, Figure 3) is developed by General Atomics in collaboration with Russia. This reactor uses (single phase) helium coolant, a stationary graphite moderator with high strength and stability at high temperatures, and refractor-coated particle fuel that retains fission products to high temperatures. GT-MHR is expected to have a core outlet temperature of 850°C and is designed to generate 285 MW_e (600 MW_t). This design include the concept of Reactor Cavity Cooling System (RCCS) that serves to remove heat from the reactor pressure vessel during normal and accident conditions. Heat is radiated from the exterior of the RPV to a series of heat exchangers, placed vertically around the vessel. [22]

The modified version of GT-MHR is called Energy Multiplier Module (EM2). EM2 is a gas cooled fast reactor which again uses helium as a coolant. This is a small-modular reactor model, expected to produce 240 MW_e (500 MW_{th}). This project assumes capability of converting used nuclear fuel into electricity and industrial process heat. [21]

The modular high temperature gas reactor (MHTGR, Figure 4), is another project proposed by General Atomics. MHTGR contains prismatic core that is made of prismatic graphite blocks which role is to moderate the reactor. The core features annular inner and outer graphite reflectors. TRISO coated fuel type is used. It is embedded in the graphite and placed in the prismatic blocks. Normal operations is assumed when the fuel is designed to operate at temperatures less than 1250°C. The temperature of gaseous helium coolant enters the core is around 259°C through a concentric inlet-outlet duct. Then forced convection causes the gas to flow up through the upcomer, a space between the outer reflector and the inner vessel wall. This helps maintain the vessel wall temperature within allowable limits. The helium exits the upcomer and then enters the upper plenum. Coolant

is then forced downward through the upper core supports and pushed into the fuel elements and coolant channels of the prismatic blocks. Finally, helium enters the lower plenum where it is forced out the concentric inlet-outlet duct. It is predicted that the average temperature rise across the core will be around 428°C causing well mixed coolant to exit the vessel around 687°C. Due to the nature of forced convection the inside of the vessel is pressurized to 6.39 MPa. [52, 89]

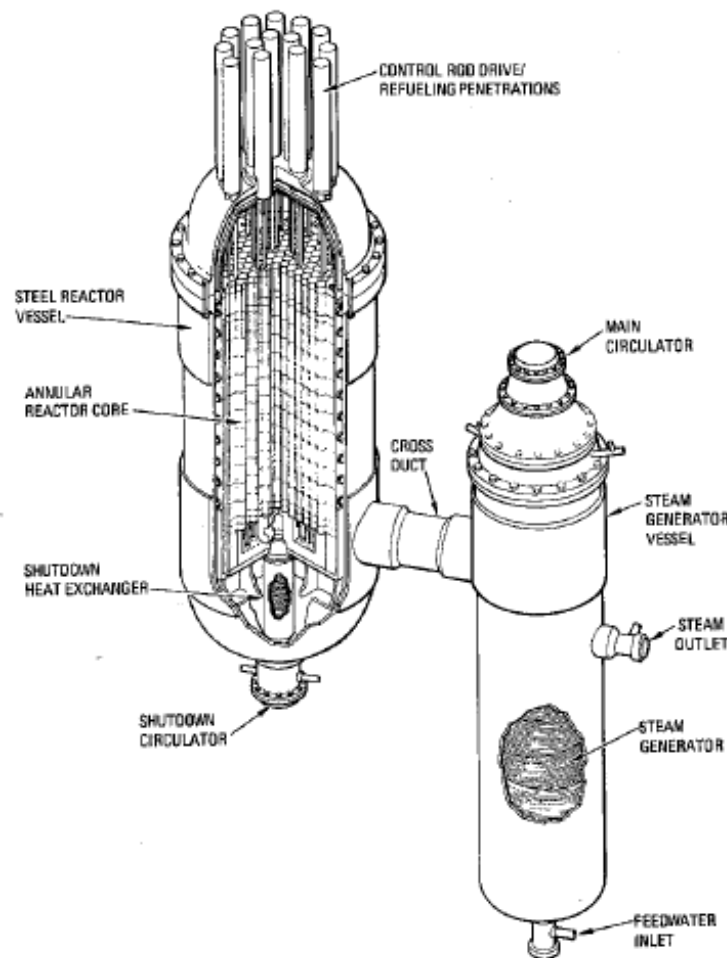


Figure 4 MHTGR module. [taken from 52 with no changes]

The Very High Temperature Reactor (VHTR), referred as the Next Generation Nuclear Plant, is an extension of the GT-MHR project. The VHTR mainly differs in

the target coolant outlet temperature which supposed to be higher than 1000°C. This design is dedicated to produce hydrogen in addition to electricity.

2.1.2. Research facilities

Each commercial design of nuclear reactor has its predecessor in research or test facility. This is a necessary step in development of new complicated systems to start from smaller scaled models and receive test data.

HTR-10 is a 10 MWth prototype of Pebble Bed Reactor and was introduced at Tsinghua University in China. This design incorporates helium coolant with pressure around 3 MPa and inlet/outlet temperatures respectively: 250°C /700°C. The main features of this design are the use of spherical fuel elements containing enriched uranium fuel with TRISO coated particles. HTR-10 facility is a prototype for HTR-PM (High Temperature Pebble Bed Modular Nuclear Reactor) design. China begins construction of first HTR-PM Unit in January 2013. Original design includes twin reactor modules of 100 MW, each driving a single steam turbine.

High Temperature Test Reactor (HTTR) was introduced by Japan Atomic Energy Agency. Unlike competing pebble bed reactor project, this design uses prismatic block (hexagonal) fuel elements. HTTR again incorporates helium as a reactor coolant. Coolant pressure and temperatures are as follows: 4 MPa and 395°C /850-950°C. Thermal output reaches 30 MW. [48]

Based on the HTTR project, JAERI is developing the Gas Turbine High Temperature Reactor of thermal power up to 600 MWt per module. One of the studies performed by JAERI on HTTR was the investigation of DEGB (Double ended guillotine break) in the coaxial pipe connected vertically to the bottom of the reactor vessel. In this design the main phenomena leading to air ingress into

reactor core is molecular diffusion and subsequent natural circulation (lack of density gradients that cause stratified exchange flow). [27, 81]

2.2. Initial DCC studies

Thermal stratification and gravity currents are common phenomena occurring both in the nature and in the engineering designed systems. Examples include thunderstorms outflows and sea-breeze fronts (gravity currents driven by differences in temperature), and avalanches of airborne snow, plumes of pyroclasts from volcanic eruptions and sand storms (driven by density gradients) [13]. Early studies of the mechanisms causing air ingress into the reactor vessel were focused on diffusion as described by Fick's Law (Takeda 1997, Takeda and Hishida 1991, Oh et al. 2006, Kim et al. 2007) and did not account for the effects of density gradients between helium (low density) and air or helium-laced air (high density) flow that leads to exchange flow [28, 82, 54, 38]. Oh et al. (2008) described gravity driven exchange as an important stage of air ingress in VHTR during D-LOFC accident [60]. After the depressurization of the reactor, when the pressure equilibrium is reached, subsequent exchange flow driven by density difference among gases will occur. The onset of the phenomena starts with the intrusion of a "nose" of cold air that enters at the bottom of the hot duct [56]. This creates a counter-current flow in the duct: cold air travels along the bottom of the hot duct forming a cold plume into the lower plenum while hot helium travels along the top of the duct out the break. The governing mass and momentum conservation equations for the exchange flow process are shown in equations (1) and (2).

$$\frac{\partial \rho}{\partial t} + u_j \frac{\partial \rho}{\partial x_j} = \kappa_m \frac{\partial^2 \rho}{\partial x_j \partial x_j} \quad (1)$$

$$\frac{\partial(\rho u_i)}{\partial t} + u_j \frac{\partial(\rho u_i)}{\partial x_j} = -\frac{\partial P}{\partial x_i} + \rho g_i + \mu \frac{\partial^2 u_i}{\partial x_j \partial x_j} \quad (2)$$

Where κ_m is the mass diffusion coefficient and is assumed to be constant. These governing equations (1) and (2) are applicable to any type of buoyant jet, including an inlet plenum break above the core, and are not limited to gas ingress following a double-ended break.

The earliest research on prediction of velocity and shape of heavy fluid intruding into a lighter fluid was provided by von Karman (1940). Results obtained by von Karman were obtained with the assumption of energy conserving current propagating in an ambient fluid of infinite depth [95]. Formation of a wedge of dense gas at the lower portion of the analyzed medium, which will propagate towards less-dense gas is well characterized by the modified Froude number. The modified Froude number, so called: the densimetric Froude number, correlates the densities of fluids to a constant value that represents flow conditions at different time scenarios (scales the inertia of the denser fluid with respect to the buoyancy force according to the fluids density difference) [63]. It can be used to predict the advancing current front speed:

$$F_h = \frac{u}{\sqrt{g'h}} = \frac{\sqrt{2}}{\gamma} \quad (3)$$

Where $g' = \frac{g(\rho_2 - \rho_1)}{\rho_2} = g(1 - \gamma)$ is the reduced gravity, h is the depth of the current and γ is the density ratio [77]. The buoyancy induced by the density difference of the two fluids requires to use the reduced gravity instead of standard one.

Oh et al. (2008) expected that densimetric Froude number during the stratified flow stage will be a function of:

$$F_h = f\left(\alpha, \frac{L}{D}, \frac{V_{vessel}}{V_{vault}}, p_r, Re\right) \quad (4)$$

where α is the orientation of the break with respect to the vertical direction, L - length of the separated hot duct on the reactor vessel side, D - diameter of the hot duct, V - volume, p_r - Pressure coefficient, and Re = Reynolds number. [77]

Benjamin (1968) provided alternate theory for the front propagation considering energy dissipation rate as an essential factor in gravity current dynamics and compare results with analysis of energy-conserving flow [5]. The theory shows different solutions for the speed of the front depending on the depth of the current. In case of flow with no energy loss, results corresponds to that derived by von Karman. It was found that if $h < 0.5d$, where d is the depth of the channel, the current is not energy-conserving and the maximum energy flux was obtained when $h = 0.347d$. [77]

According to Simpson (1982), gravity current at a horizontal plate has a characteristic front at the current leading edge which depth is larger than the following flow. At this current head area, intense mixing occurs that has an impact on the overall current behavior: its velocity and profile. Mixing arises because of billows, lobes and clefts, being created right behind the current nose (Figure 5). In the horizontal gravity current, leading edge remains in a quasi-steady, which means that it propagates with almost constant speed, depending on the fluids density difference. [50, 79]

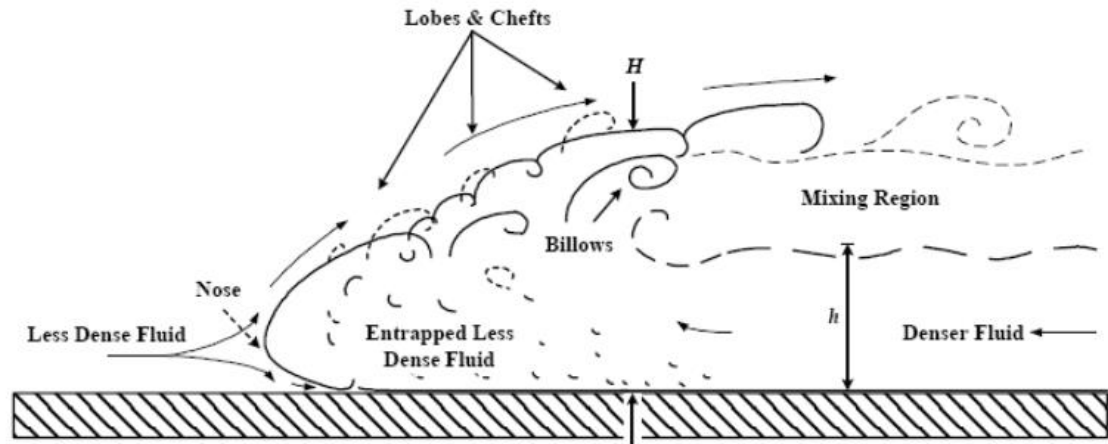


Figure 5 Sketch of the typical horizontal gravity current front propagation. [50]

Discussed studies focused on the analysis of front shape and speed. Yih and Guha (1955) on the other hand developed models to predict the interface between the two fluid layers of stratified flow [100]. They investigated that the formation of hydraulic jump can be described by a change in depth of the propagating front. The conservation of momentum and hydrostatic pressure distribution were assumed to model changes in layer depth due to hydraulic jump. Further analysis performed by Keller & Chyou (1991) included density ratios among 0 to 1 range [35]. They suggested two configurations of the current front, depending on the density ratio: half-depth heavy current depth with shallow tail (according to Simpson (1982)) and shallow heavy current front if fluids densities are below the critical density ratio. Lowe et al. (2005) investigated both: shape of the front and interface of layers in case of small and large density differences called respectively: Boussinesq and non- Boussinesq lock exchange (for water and either a sodium iodide or sodium chloride) [44]. Boussinesq lock exchange refers to Boussinesq approximation which states that the density variation is only important in the buoyancy term (ρg_i) in the Navier-Stokes equation. This approximation is valid provided that density changes remain small comparing to the reference density

(for example volume average density of the fluid in the considered medium) and whether temperature changes are insufficient to cause major fluid properties deviation comparing to their reference (mean) values.

According to Turner (1973) and Reyes et al. (2010), applying the continuity equation and Bernoulli's equation under the assumption of frictionless flow yields the following theoretical result for the helium velocity approaching the cold plume (for nomenclature please refer to Figure 6):

$$u_{LP} = 0.5\sqrt{g'd} \quad (5)$$

Experiments show that better predictions are obtained while $F_H=0.44$ instead of $F_H=0.5$ is used. Helium velocity flowing counter-current to the cold air plume can be modeled by the following expression: [71] [88]

$$u_H = \sqrt{2g'h} \quad (6)$$

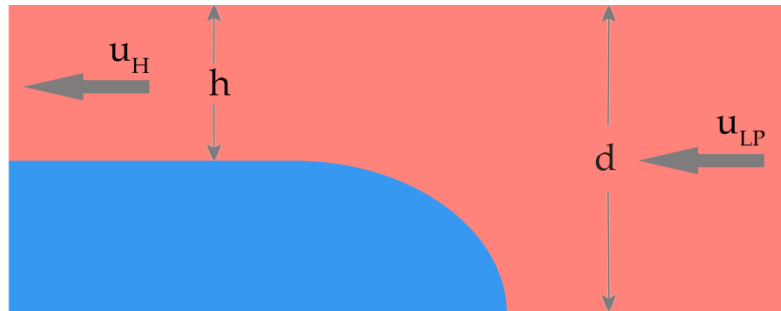


Figure 6 Simple analysis of the counter-current flow.

Expressions (5) and (6) are valid under the Boussinesq approximation, when density ratio (γ) of considered fluids stays within the limit:

$$\gamma^* < \gamma \leq 1 \quad (7)$$

where γ^* refers to the critical density ratio, approximated by Lowe et al. to be 0.3. Below that value, Boussinesq approximation is not applicable. Therefore, for:

$$0 < \gamma \leq \gamma^* \quad (8)$$

helium velocity approaching the cold plume is equal to:

$$u_{LP} = \sqrt{(1 - \gamma)gd} \left[\frac{1}{\gamma} \frac{h}{d} \left(2 - \frac{h}{d} \right) \frac{1 - h/d}{1 + h/d} \right]^{1/2} \quad (9)$$

Due to Lowe et al. the flow depth of the heavy current follows the distribution showed in Figure 7.

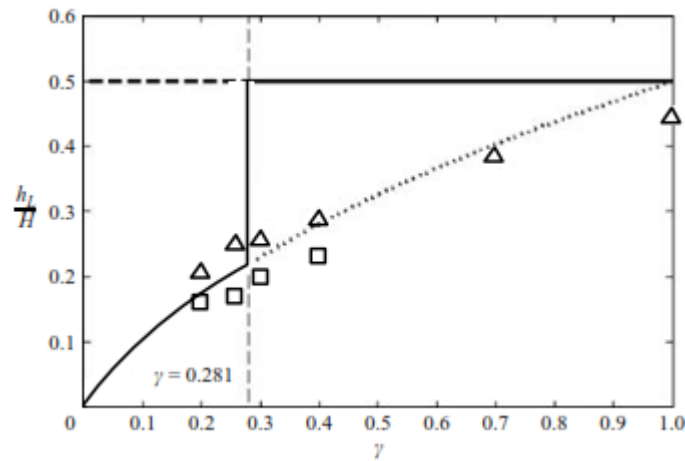


Figure 7 Flow depth of heavy current as a function of the density ratio (taken from [44] with no changes).

Lowe et al. (2005) used liquids in the lock exchange problem experiment. The question that arises is how those results can be applied in the gaseous lock exchange analysis. According to [40], the Boussinesq equations for liquids and gases are essentially similar, except for the thermal energy equation (which in case of liquids contains the additional adiabatic temperature gradient, and c_v is replaced by c_p).

Considering gaseous reactors in particular, the subsequent stage of air ingress into the reactor core arises when air-helium interface in lower plenum is established. In this state, air will start slowly diffuse into the helium and reversely. According to Oh et al. (2011) once the thermal stratified layer is created in the lower plenum, some air may flow into the reactor core by convection because of the temperature gradients among reactor internals and the vessel (local natural circulation flow) [56]. This phase is named by Oh et al. as Stage 2 stratified flow. If cold air plume will reach hot core and lower plenum structures, then it will be heated and will expand, which in turn will also reduce its density. This way, buoyancy force will exist between 'fresh', dense air and the heated one. If the kinetic energy of this buoyant flow is enough high to overcome hydrostatic head of the core, air inflow into the core will occur due to the local natural circulation rather than via molecular diffusion. On the other hand, when pressure build-up caused by buoyancy force will be less than the core hydrostatic head, the air inflow to the core will be dominated by molecular diffusion and turbulence mixing. To analytically describe the condition for air to enter the core due to local natural circulation in Stage 2 stratified flow, Oh et al. derived the following equation:

$$\frac{d}{H_{core}} > \frac{8\rho_{core}}{\rho_{LP}} \left(\frac{\gamma^3}{1-\gamma} \right) \quad (10)$$

Equation (10) was derived using velocities described by equations (6) and (9) and inserting them into the standard equation for the total kinetic energy of the flow and comparing with core hydrostatic head. If the core hydrostatic head is less than the buoyancy force, local natural circulation dominates over the molecular diffusion.[60]

2.3. DCC mitigation concepts

There are various potential mitigation schemes proposed in literature that include design features and operator actions which might prevent core or fuel structure damages caused by D-LOFC accident. One design was proposed by JAERI [81]. This approach includes insertion of a tank with helium inside the reactor vessel. During DCC, the helium leaks out of the tank creating reconditioned helium bubble at the top of the vessel, delaying the start of air ingress flow. Another design is suggested by PBMR Pty. Ltd. and includes 'diving bell' feature. The idea is to trap helium in the cavity such that after DCC, the gas intrusion into reactor vessel will be only helium. Yan et al. (2008) recommend method of oxidation mitigation following air ingress by helium injection at the top of the VHTR vessel. It appears that this concept provide reasonable results when air ingress is provided mostly by molecular diffusion which happens in HTTR. There are doubts about effectiveness of such approach in VHTR where density-gradient driven flow exists in the coaxial horizontal pipe. Other concepts focus on foam substance injection into the reactor cavity to block subsequent air ingress or injection of substance reactive to oxygen or absorbent of oxygen [58, 81]. Graphite (carbon) powder was proposed as a good candidate, because it can deposit on the core structures and be the first one to react with oxygen before gas will reach internal core graphite pores. Also silicon carbide (SiC) can be used as a protective coating, to reduce the possibility for oxygen to come into contact with support structures. Besides those proposed concepts, there are two main ideas of mitigation methods that were evaluated as the most promising methods [58]:

- *Direct in-vessel injection*: inject helium directly into lower plenum (Figure 8). Buoyancy of the injected helium replaces the air in the core (dilutes oxygen concentration) and the upper part of lower plenum. This prevents air from

moving into the reactor core and shows the most potential for mitigating graphite oxidation within the vessel.

- *Reactor enclosure*: surround the reactor with a non-pressure boundary with an opening at the bottom. Air ingress is limited by molecular diffusion through the opening at the enclosure bottom, a very slow process that allows sufficient time for the core to cool.

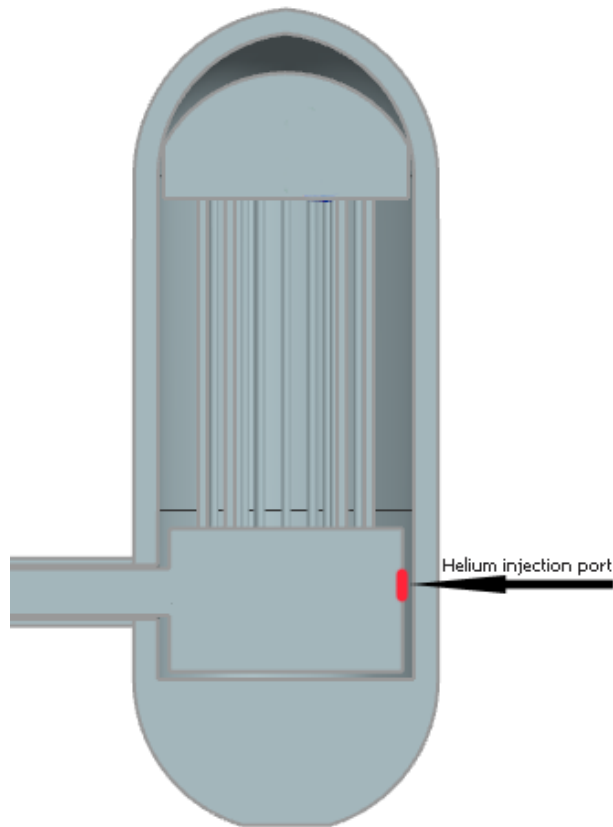


Figure 8 Conceptual helium injection port in the schematic view of VHTR reactor vessel.

Air ingress mitigation studies were computationally or experimentally investigated by several researchers. Epiney et al. (2010) investigated the cooling capabilities of different heavy gases in gas-cooled fast reactor under depressurized conditions during loss of coolant accident. Nitrogen, CO₂, argon and a nitrogen–helium mixture were tested. In the proposed solution, they applied additional dedicated reservoirs (top and bottom sides of the vessel) with heavy gas create

additional cooling capabilities by natural circulation of the mixture of helium and injected gas. The secondary gas in the additional tanks was assumed to be pressurized at 75 bar at 50 °C. Along with different types of heavy gases and injection location, various mass flow rates were investigated (controlled by valve opening area). Obtained results show CO₂ to be the best choice in terms of achieving satisfactory core temperature distribution without using additional Decay Heat Removal blowers. On the other hand, injection of CO₂ can contribute to additional graphite oxidation, thus N₂ was proposed as a possible alternative. [17]

Yurko (2010) analyzed the effect of helium injection on diffusion dominated air ingress accidents in pebble bed reactors [102]. Objective of this work was to validate the method on sustained counter current air diffusion (SCAD), developed by Yan et al. (2008), to prevent natural circulation onset in diffusion dominated air ingress accidents in HTGR [100]. Vertically oriented rupture of coaxial pipe was considered thus air was entering the reactor vessel mainly by molecular diffusion. The SCAD method assumes injection of small amounts of helium at the top of the reactor vessel. Results show that without injection, natural circulation would start after 117 min from the beginning of the transient. Helium injection delays this process by more than 120 min.

Study performed by Takeda et al. (2014) involved experimental investigation of the control method of natural circulation of air by injection of helium gas. Experimental apparatus consisted of four connected, circular, copper pipes: two horizontal and two vertical. At the beginning system was filled with air and one vertical pipe was heated and the second one was simultaneously cooled. This created natural circulation in the loop. Helium was injected (once steady state

conditions were established), from the upper part of the horizontal pipe. Different volumes of injected helium were taken into consideration, starting from 5.9 m, up to 56.0 ml. It was concluded that the velocity of natural circulation of air can be decreased by this methodology. Effectiveness of the mitigation system depends on the volume of injected helium and temperature difference among two vertical pipe passages. [84]

2.4. Graphite oxidation

As it was mentioned in the previous chapters, following a break in the VHTR pressure boundary, air will enter lower plenum and core internal structures. Even though this accident scenario is characterized by very low probability, it has always raised significant concerns while graphite oxidation was considered. Graphite, in contrast to its excellent thermal, mechanical and neutron physical properties, possesses relatively low resistance to oxidation. Since reactor internal components (lower plenum posts, core reflectors, blocks, matrix of the coated particles in the fuel compacts) are made of graphite, its gasification could compromise the structure integrity of the entire reactor system and lead to increase in local stresses (load). Oxidative weight loss can also degrade material isotropy (nuclear graphite requires very low anisotropy, less than 1.1). [15]

Figure 9 shows root causes for the air ingress accident and the eventual consequences of this event.[58]

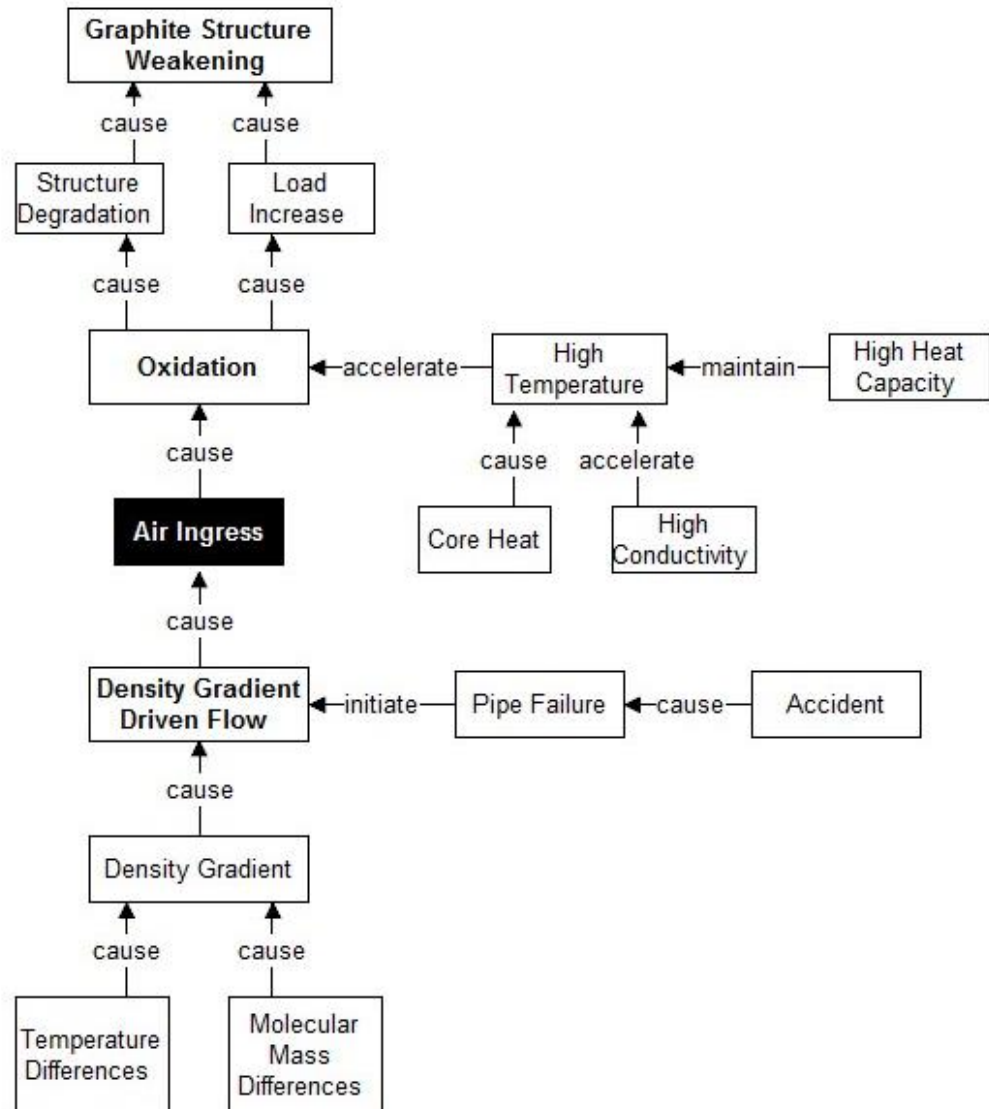


Figure 9 Root causes of air ingress accident. [58]

The rate and mechanism of graphite oxidation depend on several factors, including temperature, total and partial pressures of reactants and their availability, weight loss fraction, nuclear graphite grade, flow distribution and available reaction sites. Graphite oxidation involves complex phenomena and without experimental test results, is difficult to predict [16]. The possible graphite gasification reactions are as follows:

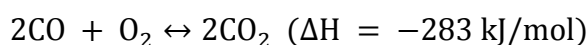




Boudouard reaction (oxidation increases due to additional CO production, it then reacts with oxygen on the graphite surface and then subsequently CO₂ further oxidizes graphite):



CO₂ combustion reaction:



where ΔH is the standard enthalpy of formation at 298 K.

During oxidation, graphite properties degradation occurs as a function of burn-off (oxidative weight loss). To quantify the scope of carbon burn-off, local partial pressures (or concentrations) of oxygen within the structure along with the kinetics of oxidation reactions over the range of temperatures need to be known. [29]

The reactions may be described as occurring in few major steps. At the beginning of the process, oxygen must be transported to the graphite surface. Subsequently, gas diffusion into the graphite pores (oxidation location) takes place. After adsorption and diffusion, actual chemical reaction must occur and carbon-oxygen bond will form. Last, the reaction products must diffuse out of the graphite thus allowing 'fresh' reactant to enter material structure [16]. In general, the reactions of carbon with oxidizing gases are controlled by the following processes:

1. Adsorption of oxygen on the graphite surface,
2. Formation of carbon-oxygen bonds,
3. Breaking of carbon-carbon bonds,

4. Desorption of CO and CO₂ gases.

Relationship between factors that influence graphite oxidation rate is not straightforward. For instance, increase in temperature enhances the oxidation rate, but response will be affected by the multiple possible oxidation pathways. In the presence of air, graphite temperatures have to be at least 350°C before any appreciable reaction will take place. Then, with temperature increase, the oxidation of graphite can be broken down into three regions. Figure 10 is used to explain the oxidation mechanism and was adapted from Marsh (1989) [46].

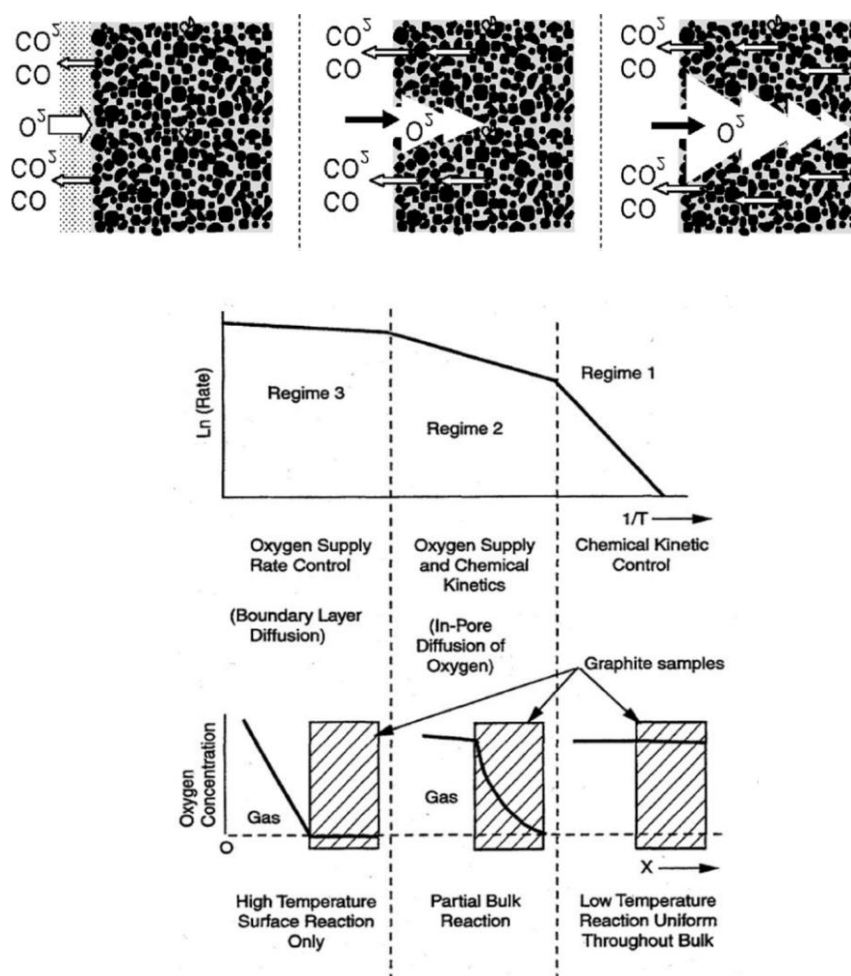


Figure 10 Graphite oxidation regimes. The upper graph shows the change in rate of the carbon gasification reaction with temperature. The lower chart shows the concentration changes of

reactant gas in the graphite, varying with the rate controlling zone [taken from Marsh (1989) with no changes]

At lower temperatures (Regime 1), $T < 650^{\circ}\text{C}$, in-pore gasification takes place which means that reaction occurs at the surface of pores in the graphite. In the Regime 1, nuclear graphite grade plays significant role because differences in the oxidation rate between different graphite grades result from differences in the material microstructures. This regime is controlled by the reaction kinetics since the chemical reaction kinetics are limited. Oxidation rates are relatively low due to lower temperatures and increase exponentially with temperature. Uniform changes in the graphite porosity occur while the surface of the material remains mostly unchanged. It has to be underlined that negligible oxidation would occur below 450°C . At the temperature around 400°C , reaction rate is around $3 - 8 \cdot 10^{-10} \frac{1}{\text{s}}$. The overall reaction rate in lower temperature region can be estimated by a simple Arrhenius expression:

$$k_o = A \exp\left(\frac{-E}{RT}\right) \quad (11)$$

where:

k_o - oxidation rate constant [1/s],

A - linear pre-exponential coefficient,

E - effective activation energy [J/mol].

Second oxidation region (Region 2), refers to temperature range between around $650-750^{\circ}\text{C}$ and is called: transition region. As temperature increases, so does the reaction rate and oxygen is more likely consumed by the reactions adjacent to the graphite surface instead of diffusing into internal volume pores.

Region 3 ($T > 750^{\circ}\text{C}$) of graphite gasification is also named as the mass transfer or boundary layer region. Reaction rate is dominated by reactant and product diffusion rates through the gaseous boundary layer to and from the reactant sites.

There are several factors that graphite has to fulfill to make it applicable in nuclear systems: high purity, density, irradiation stability, thermal conductivity, strength, oxidation resistivity and low anisotropy, thermal expansion, elastic modulus and cost. Nuclear grade graphite is an excellent moderator, reflector and core structural material in high temperature gas-cooled reactors. [14, 19]

Table 1 The main properties of the two main types of the nuclear graphite.

Property	Unit	IG-110	NBG-18
Density	g/cm^3	1.78	1.85
Grain size (average)	μm	20	300
Anisotropic ratio		1.05	1.03
Tensile	MPa	25	24
Elastic Modulus	GPa	9.04	11.5
Thermal Conductivity	W/mK	144.43	140
Filler		Petroleum coke	Pitch coke

Nuclear graphite oxidation was investigated by a number of researchers. Xiaowei et al. (2004) investigated the effect of temperature (in the range between 400°C - 1200°C) on graphite oxidation behavior for the IG-110 (Toyo Tanso Co., Ltd) [98]. This type of graphite is of particular interest because of its application in the 10 MW HTR-10, located in Tsinghua University in China (60 t of graphite and 27 000 fuel elements). The oxidation experiment lasted for 4 hours with dry air flow rate equal to 20 ml/min. Xiaowei et al. concluded that the oxidation quantity (weight decrease of graphite normalized with the initial specimen mass) increases with

initial temperature. The maximal oxidation quantity was 34.4 % at 1200°C. They also concluded that the changes of oxidation rate depend on different temperature regimes. In each considered temperature, oxidation rate increases after 90 sec from the beginning of the experiment. It is because at that time, oxidation chamber was completely filled with air. Oxidation rate is the highest at 900°C. Differences among oxidation rates stem from the change in the total reaction surface. At higher temperatures, graphite porous microstructure changes: closed, small pores extend to micro- and subsequently meso-pores and reaction surface increases and sharp increase in reaction rate occurs due to the larger available surface area. Fuller et al. (1997) found that the maximum reaction surface (for IG-110 at 750°C) is around 35-40% burn-off. After this peak occurs, walls are being gradually consumed and the reaction rate decreases along with the decrease in the available reaction surface. [19]

Oh et al. (2009) carried out research on the graphite oxidation at the test station at the Idaho National Laboratory (INL). The investigated graphite sample was also IG-110, cylindrically shaped (1 inch height and diameter with inner hole with diameter equal to 0.5 inch). The experiment was performed at 650°C. [64]

Kim et al. (2008) studies focused on the estimation of graphite density and mechanical strength variation of VHTR during air-ingress accident. Graphite burn-off model was developed on the basis of analogy of graphite oxidation process to parallel electrical circuit. This model was then implemented into the GAMMA code. Calculations for GT-MHR 600MW were undertaken for 11 days after the accident and result in 4.5% decrease in density and a 25% reduction of mechanical strength, mainly in the bottom reflector. To implement data on graphite density changes due to oxidation process, experiments on IG-110 graphite oxidation were carried out in an electrical furnace at different temperature ranges. [37]

Due to Kim et al., (2007) the 10 % weight loss of graphite due to transient gasification, can decrease the mechanical strength of the graphite structure by as much as 50%, particularly if oxidation occurs in Regions 1 and 2. [36, 37]

El-Genk et al. (2012) have significantly contributed to the development of knowledge on graphite oxidation in HTR accident conditions. Despite the work done on the validation of gasification model for NBG-18 nuclear graphite and further experiments on the graphite oxidation, they performed transient gasification of NBG-18 nuclear graphite in a VHTR flow channel and thermal-hydraulics analyses of 1/6 prismatic VHTR core and of fuel element with bypass flow. The transient gasification analysis performed by El-Genk et al., of VHTR fuel channel (800 mm long, inner void diameter = 15.875 mm, wall thickness = 5.683 mm), varied the initial temperature from 800 K to 1100 K at Reynolds numbers equal to 5, 10 and 20. The analysis was carried out until reaching a 10% graphite weight loss at the entrance of the flow channel. It was concluded that below 840 K, uniform gasification along the channel length occurs and gasification time is almost independent of the Reynolds number. On the other hand, the effect of flow velocity is more significant at higher temperatures: increased graphite weight loss is observed with increased oxygen supply and also with increased oxygen supply, gasification time is shortened. Alternatively, decrease in total graphite weight loss is observed with increasing air inlet temperature due to the exponential effect of temperature on the gasification rate (graphite gasification is limited to inlet section of the channel due to the high local gasification rate and the fast depletion of oxygen in the bulk gas flow). After 4.8 h of the gasification transient, the graphite weight loss at the entrance of the channel reaches 10% (at the exit of the channel is only 1.2%). Results show that at a high initial temperature, $T=1100$ K, gasification time increases from 0.5 h to 1.25 h as Reynold number decreases from 20 to 5. At a

lower temperature of 800 K, graphite loss occurs all along the flow channel, and t is as much as ~ 100 h, regardless of initial oxygen supply. Results demonstrated that the heat of formation of CO and CO₂ gases should not be neglected in the analysis of graphite gasification. Neglecting these heats of formation could significantly over estimate the total graphite loss and the transient gasification time. [14, 15, 16]

2.5. Computational methods applied to DCC analysis.

Validation of CFD codes such as Ansys Fluent, applicability to analyze the air ingress phenomena, was an essential part of the work done by Oh et al. (2010) [57]. The results obtained from Ansys Fluent and experimental data on a lock exchange flow (collected by ETH Zurich, Grobelbauser et al.(1993)) showed very good agreement for density-gradient driven air ingress stratified flow (4.8% deviation). Oh et al. (2008) also conducted preliminary CFD analysis for density-difference induced stratified flow accounts for hot gas duct and reactor vessel of GT-MHR. Two codes were applied in the air ingress analyzes: GAMMA and Ansys Fluent 6.3. GAMMA is a multidimensional, multi-component mixture analysis code to predict air ingress phenomena in an HTGR. Depressurization and diffusion/natural convection stages were solved by the GAMMA code (it takes much less CPU time compared with that of CFD code) and stratified flow was simulated in Fluent (GAMMA does not have turbulence models to calculate complicated fluid fields required for horizontal stratified flow). Geometry of the analyzed system was meshed using GAMBIT software. The total number of mesh cells for the reactor and the cavity is 31 232, and they are all hexagonally meshed. The solver was set up as segregated, first order implicit and unsteady. They adopted a noniterative time-advanced scheme that does not need the outer iterations (it uses only single outer iteration per time-step), which significantly

speeds up transient simulations. Air and helium were the two gas species considered and density calculation was made under assumption of incompressible ideal gas law. The core and lower plenum were simplified to be porous bodies. [63]

Ferng et al. (2012) also adopted CFD methods to simulate air ingress phenomena. He modeled HTR-10 pebble-bed core. To model the reactor core, Ferng assumed porous approach. Very large amount of grid cells are needed to model thousands of pebbles in the reactor core in realistic manner. The huge computational time and cost are not reasonable for the CFD work, especially in performing the transient simulation. In this study, depressurization period was not considered because of its relatively short time comparing to the rest of D-LOFC stages. The turbulence model used for simulations was K-Epsilon. Number of mesh cells in the system was 75 040. The result of this work shows that the coolant maximum temperature is predicted to increase from 1084 K (maximum at normal operation) to 1100 K at time = 60 sec after the occurrence of D-LOFC. This is the initial increase in order to exothermic oxidation reactions. After that, temperature will gradually decrease due to the power decay. [18]

The thermal-hydraulic design for the HTTR was carried out by using codes named FLOWNET and TEMDIM. FLOWNET flow network analysis code, was used to evaluate coolant flow rate and temperature distributions. It accounts for all flow paths that may affect the fuel temperature, such as bypass flow between fuel blocks or horizontal cross flows among stacked fuel blocks. The effective coolant flow rate calculated in fuel blocks is used as an input data for the TEMDIM code. TEMDIM provides fuel temperature distribution with multi-cylindrical model using hot spot factors. The maximum fuel peak temperature obtained by TEMDIM at the beginning of the full power operation of HTTR is 1398 °C. Further analysis shows that by using multiple fuel enrichments zones, the peak fuel operating temperature

can be reduce to 1216°C while fuel design limit for anticipated operational occurrences and fuel temperature limit for normal operation are specified at 1600°C and 1495°C, respectively based on experimental results. [41, 48]

The RELAP5 series of codes has been developed at the Idaho National Laboratory for over 25 years under sponsorship of the U. S. Department of Energy, the U. S. Nuclear Regulatory Commission. Riemke et al. (2006) presented version 2.3 of the RELAP5-3D code that includes all models previously available only in ATHENA version of this code. ATHENA was a code developed for Gen IV nuclear reactor design and licensing procedures. Most of the necessary models for pebble bed fuel were implemented in this code such as heat transfer and pressure drop correlations for porous media or oxidation of graphite in steam and air. [72]

Davis et al. (2005) analyzed the assessment of RELAP5-3D code for analysis of VHTR. This work focused on validation of pressure loss across pebble bed and molecular diffusion models. The results obtained via RELAP5-3D and experimental data showed very good agreement. Data for molecular diffusion were collected from inverted U-tube experiments (Hishida and Takeda 1991) while code capability to model natural circulation of air through pebble bed was investigated using data from NACOK facility [12]. Unfortunately it is difficult to model the exchange flow phase using RELAP5-3D code. It does not contain appropriate correlations for gaseous counter current flow. The ways to simulate the D-LOFC using this tool are:

- splitting the pipe model: instead of introducing concentric inlet-outlet duct one should model two separate pipes with single gases: air and helium,
- addition of new correlations into the system code,

- linking the results of exchange flow simulation obtained via CFD software with RELAP5-3D that will cover the molecular diffusion phase.

Reasonable work was performed also on coupling RELAP5-3D and Fluent to analyze VHTR. Anderson (2006) modeled thermal mixing of the coolant exiting the core to lower plenum by codes coupling. Anderson used RELAP5 VHTR model outlet conditions to provide the inlet boundary conditions to the FLUENT outlet plenum model. This approach allows to save computational expense which would become a problem when only FLUENT would be used to model three-dimensional effect in lower plenum as a part of entire reactor. [1]

The need for HTGR analysis tools led to further development of MELCOR code (developed at Sandia National Laboratories for the U.S. Nuclear Regulatory Commission) which original capabilities include progression of severe accidents in light-water reactors. Corson (2010) provided study on new input techniques for MELCOR HTGR analysis that accounts for [11]:

- radiation heat transfer model between solid surfaces in an HTGR,
- fuel and cladding geometric parameters calculation for pebble bed /prismatic block-type HTGR,
- appropriate input parameters selection.

Corson applied above methods to input decks for RCCS, PBMR and HTTF. RCCS results show that MELCOR accurately predicts radiation heat transfer rates from the vessel but can over predict convective heat transfer rates and RCCS coolant flow rates. In case of PBMR, results show that thermal striping from hot jets in the lower plenum during steady-state operation, and in the upper plenum during P-LOFC, may be a major design concern. Hot jets might potentially melt control rod

drive mechanisms or cause thermal stresses in plenum structures. HTTF results are reasonable and might be used to validate MELCOR for HTGR analyses. [11]

R. Schultz (2008) underlines that CFD codes such as FLUENT or STAR-CCM+ are an ideal tool for simulating mixing and three-dimensional flow in system components, whereas system analysis tool such as RELAP5-3D is appropriate for entire system models. [75]

2.6. CFD model validation and verification methodology

Some of the basic concerns regarding the CFD techniques are whether the computational solution assure credibility according to the exact solution of the governing partial differential equations and if so under what conditions. Before CFD simulation results can be considered as a reliable outcome for the analysis of DCC event in VHTR, there is a necessity to establish the validity of obtained numerical results. Considerations on the solution behavior of the applied model are implicated by the following properties: consistency, stability, convergence, accuracy and efficiency. [87]

Numerical solution is considered as consistent if the truncation error becomes equal to zero as the grid spacing and time step \rightarrow zero (obtained solution is represented by the system of algebraic equations which exhibits equivalency to the original governing equations). Truncation error quantifies the difference among discretized equation and the exact one (higher order terms in the Taylor series expansion about a single nodal point). Fullfilling the consistency condition, even if necessary, does not mean that the exact solution of the partial differential equations is followed [87].

In addition to consistency, stability property have to be covered by the computational solver. Stability means: errors decay as the numerical method

proceeds. Unfortunately, no stability checking methodology has yet been considered universal. However, some analysis techniques usually provide sufficient indications on avoiding solution instabilities, for instance: setting time step below certain limits, usage of under-relaxation factors, application of the von Neumann method for stability analysis. Majority of CFD codes employs the implicit-type solution procedure that ensures inherent solver stability (unconditionally stable procedures). In this case, instability can arise from the usage of the segregated solver approach (transport properties calculated sequentially) instead of being a result of insufficient temporal discretization as in the explicit-type approach (conditionally stable).

The convective Courant number (ratio of the physical time-step to the mesh convection time scale) is a helpful indicator to select the time-step size for unsteady simulations. For time-accurate simulations, the convective Courant number should be 1.0 on average in the zone of the interest (Courant-Friedrichs-Levy condition). This value implies that the fluid moves by about one cell per time step. [85]

If the numerical method satisfies consistency and stability criteria, the numerical procedure can be considered as convergent. Iterative convergence is achieved when discretized governed equations (monitored as residuals) reach desirable tolerance level at every node and solution does not change with iteration progress. Residuals should be at least three orders of magnitude decreased for each equation solved over the entire domain. Grid convergence on the other hand seeks for the grid size independent results.

Importance of solution accuracy is coupled with the level of approximation applied in the numerical method. It can be expected that higher-order

approximations or grid refinement in conjunction with sufficiently small time step can lead to solution accuracy. Nevertheless, accurate results are not necessarily reached once convergence is accomplished. There are sources of computational errors that can affect accuracy of obtained solution:

- discretization error that arises from the application of the order of time discretization and grid refinement,

- round-off error that exists due to the computer accuracy and approximation of true value of the variable (single precision account for a number of 7 significant digits),

- iteration or convergence error occurs because of the discrepancies among fully converged and not fully achieved residuals tolerance level.

- physical-modeling error arises when uncertainties exist about the formulation of the model physics and applied simplifications are over estimated,

- human error that involve computer programming errors (can be assessed with code verification and validation) and improper application of CFD code, for instance: inappropriate boundary conditions, turbulence model, low quality mesh or invalid geometry.

The most convenient way to verify CFD simulations is to compare analysis outcomes with experimental data. ASME V&V20-2009 document describes the procedures to assess the accuracy of computational simulation, focusing on the validation and verification approaches [85].

This document defines the validation process as the: “process of determining the degree to which a model is an accurate representation of the real world from the

perspective of the intended uses of the model". Validation process must be preceded by code and solution verification. [85]

In general code verification assesses code correctness and specifically involves error evaluation for a known solution. By contrast, solution verification, involves error estimation, since the exact solution to the specific problem is unknown.

Code and solution verification are mathematical activities, with no concern whatsoever for the agreement of the simulation model results with physical data from experiments; that is the concern of validation. On the other hand, solution and code verification will be used in the validation process and this way they are coupled together to assess the accuracy of the computed solution.

Code verification can only be done by systematic discretization convergence tests and monitoring the convergence of the solutions towards a known "benchmark" solution (i.e., a standard of comparison). The best benchmark solution is an exact analytical solution.

Systematic grid refinement is the cornerstone for solution verification process and provide an estimate of error. The most widely used methods to estimate the error is the Richardson Extrapolation. Uncertainty estimates in the grid independence analysis can be calculated by Roache's Grid Convergence Index (GCI) [73]. In this research, Richardson Extrapolation with GCI will be implemented. This method requires at least three systematic high-quality grids. According to Celik et al. (2008), recommended procedure for estimation of discretization error is as follows [10]:

1. Define a representative grid size:

$$h_k = \frac{1}{N} \left[\sum_{i=1}^N (\Delta V_i) \right]^{1/3} \quad (12)$$

where:

N - total number of cells used in the model,

ΔV_i - volume of the i_{th} cell.

2. Calculate grid refinement factors (r) for coarse, medium and fine meshes:

$$r_{CF} = \frac{h_{coarse}}{h_{fine}} \quad (13)$$

$$r_{CM} = \frac{h_{coarse}}{h_{medium}} \quad (14)$$

$$r_{MF} = \frac{h_{medium}}{h_{fine}} \quad (15)$$

Grid ratio has to be carefully selected. To avoid significant differences in resolving the flow physics inside the computational domain, the magnitude of the refinement factor cannot be too high. On the other hand, too small r value (~ 1.0), is not recommended since it will bring difficulties to differentiate among grid and for instance iterative convergence errors or computer round-off. This is why, the grid refinement ratio should be a minimum of $r \geq 1.1$ and the value that comes from experience and recommended by Celik et al. (2008) is $r \sim 1.3$.

3. If $h_{fine} < h_{medium} < h_{coarse}$ and $r \geq 1.1$, apparent order p of the method can be derived using the following expression:

$$p = \frac{1}{\ln(r_{MF})} |\ln|\varepsilon_{CM}/\varepsilon_{MF}| + q(p)| \quad (16)$$

$$q(p) = \ln \left(\frac{r_{MF}^p - s}{r_{CM}^p - s} \right) \quad (17)$$

$$s = 1 \cdot \text{sgn}(\varepsilon_{CM}/\varepsilon_{MF}) \quad (18)$$

where:

$$\varepsilon_{CM} = \varphi_{coarse} - \varphi_{medium}$$

$$\varepsilon_{MF} = \varphi_{medium} - \varphi_{fine}$$

φ_k - solution on the k^{th} grid (for instance velocity, temperature, pressure, etc.).

Equations (16), (17) and (18) can be solved using fixed-point iteration. Value of equation (18) should be positive, otherwise it will indicate oscillatory convergence.

4. Find extrapolated solution:

$$\varphi_{ext}^{MF} = \frac{r_{MF}^p \varphi_{fine} - \varphi_{medium}}{r_{MF}^p - 1} \quad (19)$$

$$\varphi_{ext}^{CM} = \frac{r_{CM}^p \varphi_{medium} - \varphi_{coarse}}{r_{CM}^p - 1} \quad (20)$$

5. Calculate the following relative errors:

-approximate relative error:

$$e_a^{MF} = \left| \frac{\varphi_F - \varphi_M}{\varphi_F} \right| \quad (21)$$

-extrapolated relative error:

$$e_{ext}^{MF} = \left| \frac{\varphi_{ext}^{MF} - \varphi_F}{\varphi_{ext}^{MF}} \right| \quad (22)$$

6. Determine the Grid Convergence Index:

$$GCI_{fine}^{MF} = \frac{1.25e_a^{MF}}{r_{MF}^p - 1} \quad (23)$$

GCI will provide information on the percentage deviation of the computed value from the asymptotic numerical value. It provides an error band on how the obtained solution differs from the asymptotic value and how the results will change with further mesh refinement.

3. High Temperature Test Facility

3.1. Scaling analysis

The objective of the scaling methodology is to model the test facility in such way that it will be able to determine the physical dimensions and operating characteristics and be capable of simulating the important flow and heat transfer behavior of the MHTGR during DCC event. [76]

Scaling methodology used in the design of the HTTF, the Hierarchical Two Tiered scaling methodology, is fully described in the USNRC's Severe Accident Scaling Methodology presented in Appendix D of NUREG/CR-5809 [103].

The steps in scaling process are as follows [76]:

1. Identify the thermal fluid processes that should be modeled.
2. Determine similarity groups to be preserved between the test facility and the full-scale prototype.
3. Establish priorities for preserving these similarity.
4. Ensure that important phenomena have been identified and addressed through the similarity groups.
5. Provide design specifications for the test facility and test program.
6. Quantify biases due to scaling distortions since it is unlikely that all similarity groups will be preserved.
7. Identify the critical attributes of the test facility that must be preserved to meet Quality Assurance requirements.

The following are the characteristic ratios for the exchange flow phenomena of the air ingress phase of the DCC event derived in the HTTF Scaling Report:

1. Exchange Flow Density Ratio

$$\left(\Pi_{\Delta\rho,EF}\right)_R = \left(\frac{\rho_{cavity,0} - \rho_{vessel,0}}{\rho_{cavity,0}}\right)_R \quad (24)$$

2. Exchange Flow Turbulent Peclet Number Ratio

$$\left(\Pi_{Pe,EF}\right)_R = \frac{u_{Brk} d_{Brk}}{\kappa_t} = 1 \quad (25)$$

3. Exchange Flow Reynolds Number Ratio

$$\left(\Pi_{Re,EF,H}\right)_R = \left(\frac{\rho_{cavity,0} u_{Brk,H} d_{Brk}}{\mu_{cavity,0}}\right)_R = \left(\frac{\left[\rho_{cavity,0} (\rho_{cavity,0} - \rho_{vessel,0})\right]^{\frac{1}{2}} d_{Brk}^{\frac{3}{2}}}{\mu_{cavity,0}}\right)_R \quad (26)$$

4. Exchange Flow Velocity Ratio

$$\left(u_{Brk,H}\right)_R = \left(\frac{d_{Brk} (\rho_{cavity,0} - \rho_{vessel,0})}{\rho_{cavity,0}}\right)_R^{\frac{1}{2}} \quad (27)$$

5. Exchange Flow Time Scale Ratio

$$\left(t_{EF,H}\right)_R = \left(\frac{V}{Q_{Brk,H}}\right)_R = \left(\frac{\rho_{cavity,0}}{\rho_{cavity,0} - \rho_{vessel,0}}\right)_R^{\frac{1}{2}} \left(\frac{V}{d_{Brk}^{\frac{5}{2}}}\right)_R \quad (28)$$

3.2. HTTF design

Design work and scaling analyses were successfully performed for the construction of an integral High Temperature Test Facility (HTTF) at Oregon State University (OSU). The HTTF is a reduced scale model of the Modular High

Temperature Gas Reactor (prototype). The facility is capable of operation at 850°C with a maximum operating pressure of 0.8 MPa. The nominal working fluid is helium although other gases can be used as well. Amongst the main reasons for the use of helium are the inert characteristics of the gas and the good thermodynamic properties (such as high specific heat capacity and thermal conductivity). Application of a gas instead of water as a working fluid removes the requirement to ensure that an undesired fluid phase change could occur in the reactor core. The facility does not use nuclear fuel to produce power; it is equipped with graphite heater rods that produce approximately 2.2 MWth. The graphite prismatic block structure in the prototype is replaced by ceramic blocks in the test facility to capture prototypical temperature profiles. Ceramic blocks are made of GreenCAST94F (density = 2930 kg/m³ and heat capacity = 1200 J/kg K). The facility is configured to simulate a variety of postulated depressurized conduction cooldown, pressurized conduction cooldown events and normal system operation.

The HTTF facility will be used to model the thermal hydraulics of design basis and beyond design basis scenarios, thus providing experimental thermal hydraulic data to validate computational thermal hydraulic codes. The HTTF has been designed to meet certain experimental objectives during each phase of a DCC transient, including: the lower plenum temperature profiles during exchange flow air-ingress, the effects of the lower plenum structures on exchange flow phenomena, the rate of air-ingress. Other parameters that can be validated with experimental data from HTTF are for instance the time to onset of air natural circulation, the radial heat conduction temperature profiles, thermal radiation heat transfer rates, the high temperature loop natural circulation flow rates following the air-ingress phase, and the effect of flow bypass flow areas on the transient behavior.

The HTTF is 1:4 scale in height and diameter. The HTTF also features a 1:8 pressure scale to the MHTGR along with a 1:1 temperature scale. Below figure presents facility vessel geometry and internal core components.

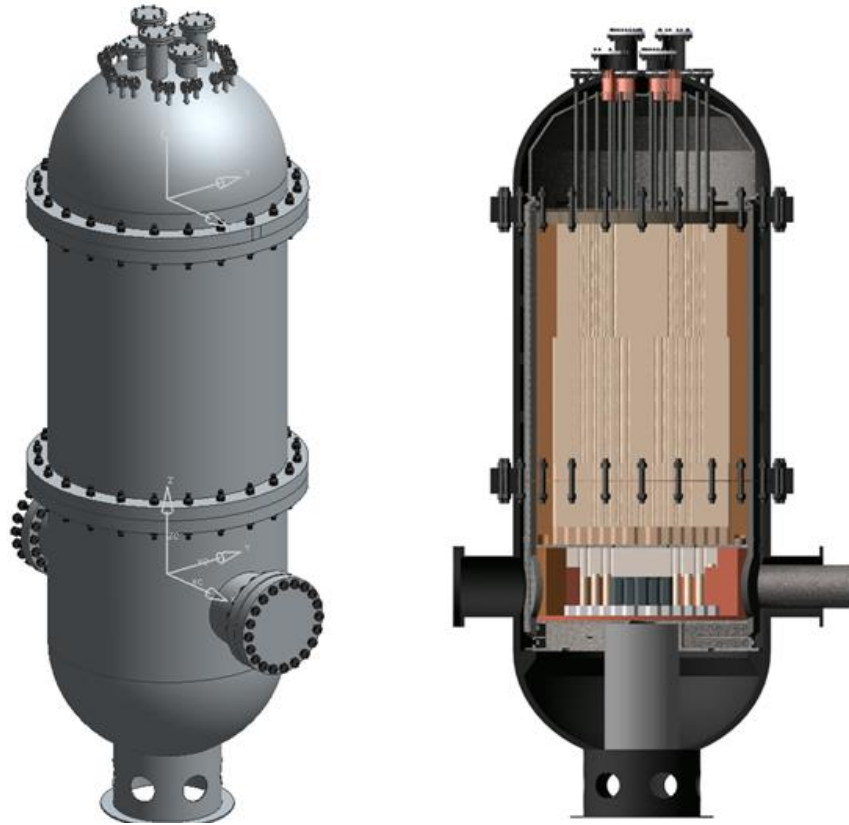


Figure 11 Geometry of the HTTF reactor core

The helium flow path in HTTF is shown in Figure 12. Cold helium enters the vessel through the outer section of the integrated duct and flows downward through the MCSS. During normal operation, coolant exits the MCSS and flows upward between outer and inner core barrels (upcomer). Helium then crosses the upper plenum and flows downward through core coolant channels. Subsequently, hot helium enters the lower plenum and exits the vessel through the inner section of the cross duct.

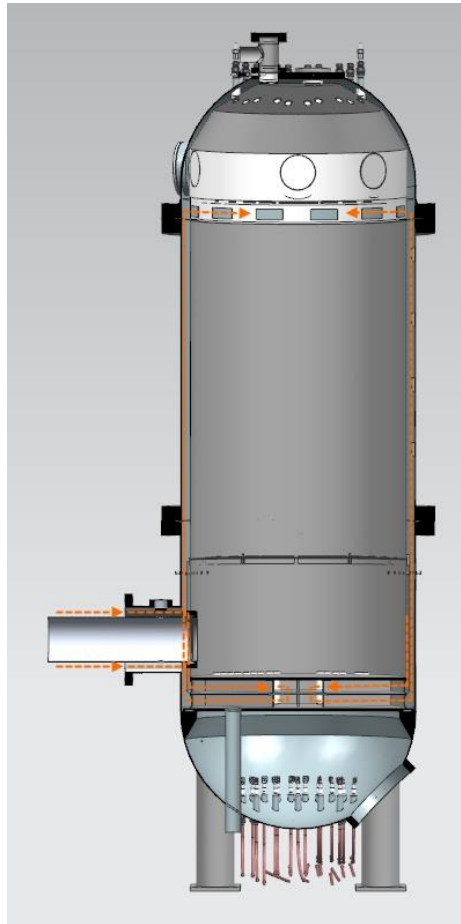


Figure 12 Helium flow path in HTTF.

The HTTF reactor core is built of 10 hexagonal, prismatic core blocks. The core is surrounded by number of reflectors on each side (2 upper reflectors, 3 bottom reflectors and side reflectors). There are also 3 separate blocks designed to model the lower plenum: lower plenum roof, lower plenum and lower plenum floor. The HTTF core block and block cross section are shown in Table 2 and Figure 13. About 700 channels are shown in the core lock cross section view, indicated by three different colors. Coolant flow paths are shown by blue color, the red channels represent the voids where the heater rods are placed, and bypass flow paths are depicted by the green color.

Gas composition measurements can be done within a specific coolant channels. In the HTTF instrumentation plan, six concentration gas instrumentations are located in the heated region in each core block.

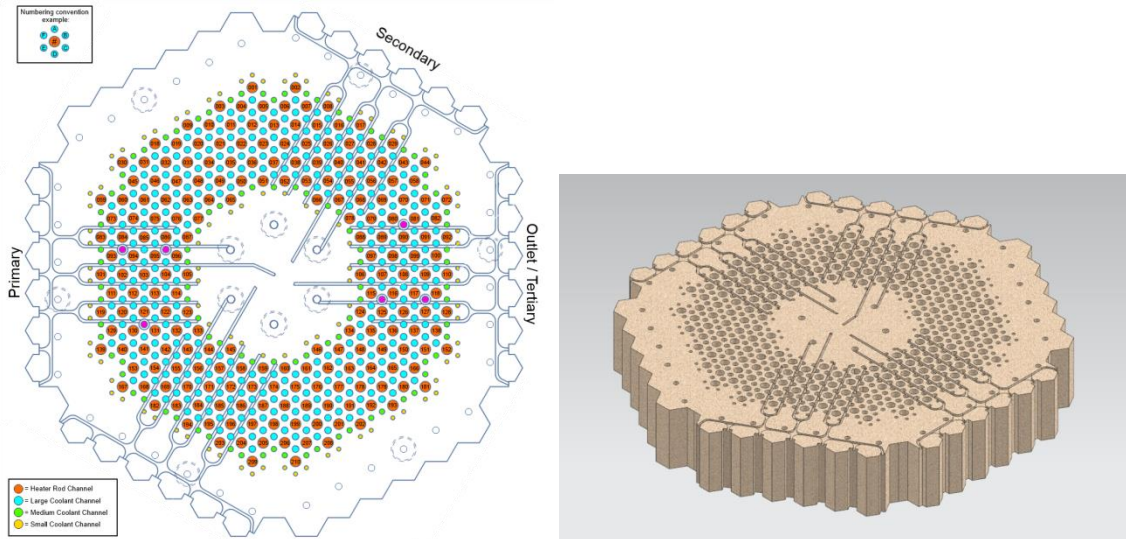


Figure 13 HTTF core block and core block cross section.

HTTF lower plenum serves as a mixing chamber for the hot helium gas leaving reactor core and it also consists of 163 support columns that holds the core structure (Figure 14).

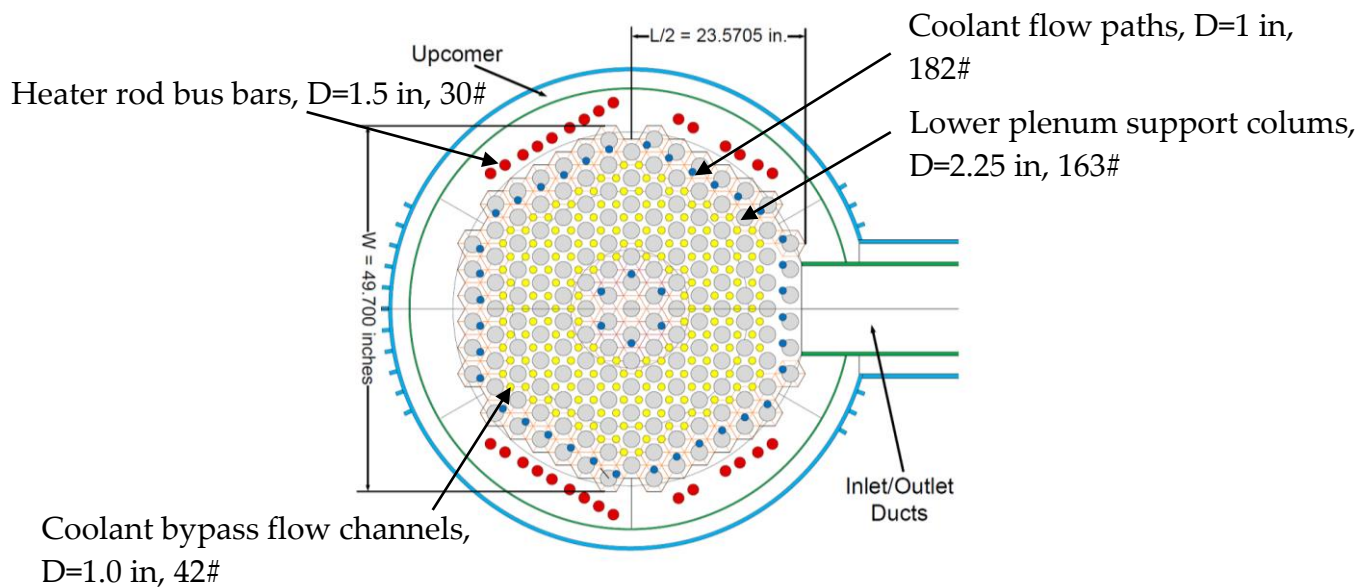


Figure 14 HTTF lower plenum channel and support posts arrangement.

Table 2 Overall channel distribution in the particular HTTF segments.

Channels description	Channel structure	Height [in]			
Core blocks (CB): 6 inner gap 36 outer gap 516 coolant 210 heater rods (HR ^{1,2})	CB, HR ₁	11''	Upper Core Reflector HTTF-415110	Upper Reflector #2 HTTF-415105	Upper Core Reflector HTTF-415110
	CB, HR ₁	4''		Upper Reflector #1 HTTF-415104	
	CB, HR ₁ → HR ₂ ,	7.8''		Core Block #10 HTTF-415202	
Lower Reflector 1 (LR1): 36 outer bypass 6 inner bypass 180 coolant 30 Heater rod buss bars (HRB)	CB, HR ₂	7.8''	Center Core Reflector HTTF-415109	Core Block #9 HTTF-415201	Center Core Reflector HTTF-415109
	CB, HR ₂	7.8''		Core Block #8 HTTF-415201	
	CB, HR ₂	7.8''		Core Block #7 HTTF-415201	
	CB, HR ₂	7.8''		Core Block #6 HTTF-415201	
	CB, HR ₂	7.8''		Core Block #5 HTTF-415201	
	CB, HR ₂	7.8''		Core Block #4 HTTF-415201	
	CB, HR ₂	7.8''		Core Block #3 HTTF-415201	
Lower plenum roof (LPR): 6 inner bypass 36 outer bypass 192 coolant	CB, HR ₂	7.8''	Center Core Reflector HTTF-415109	Core Block #2 HTTF-415201	Center Core Reflector HTTF-415109
	CB, HR ₂	7.8''		Core Block #1 HTTF-415201	
	CB, HR ₂	7.8''		Core Block #1 HTTF-415201	
Lower Plenum: 163 posts	CB, HR ₂	7.8''	Lower Core Reflector HTTF-415108	Core Block #1 HTTF-415201	Lower Core Reflector HTTF-415108
	CB, HR ₂	4''		Lower Reflector #3 HTTF-415103	
	CB→LR1, HRB	4''		Lower Reflector #2 HTTF-415102	
HR ^{1,2} – 1 and 2 refers to different placement or rods	LR1→LPR	4''	HTTF-414034	Lower Reflector #1 HTTF-415101	Lower Plenum Outlet Reflector HTTF-414035
	LPR→LP	7.8''	Lower Plenum Rear Reflector HTTF-414033	Lower Plenum Roof HTTF-414032	
	LP, HRB	14''		Lower Plenum	
	-	3.125''		Lower Plenum Floor HTTF-414031	

The HTTF will be instrumented with measurement devices to collect flow rate, pressure, temperature, and gas concentrations at specific locations throughout the facility. To measure temperature, thermocouples are installed in 300 specific locations in the facility. Differential pressure and flow rate in the system is

measured with the differential pressure transducers. The circulator control system will also provide data on the flow changes in the system. There are also 32 locations where gas concentration is measured (Table 3).

Table 3 Gas concentration instrumentation (GCI) placement and number.

Region	Number of GCI
Lower and upper reflectors	6
Upcomer	4
Upper plenum	4
Lower plenum	4
Inner duct	6
Outer duct	4
Break	2
Cavity	2
Total	32

As can be seen in Table 3, cross-duct will be also equipped with gas concentration instrumentation. This instrumentation is arranged in the form of 'Rakes' that include several vertically aligned thermocouples along with gas concentration measurement devices. The Rake closest to the vessel side (placed 2.6 m away from the break valve location) will be further used in this work as reference plane to gather gas concentration data from the CFD analysis, which in turn can be further used in the validation study among the D-LOFC simulation and tests run at the HTTF. [8]

4. DCC theory and physics

The chart below shows the sequence of events that occurs during D-LOFC in the VHTR. At the onset of the accident scenario, the system will experience a loss of forced circulation after the break in the pressure boundary (flow will depend on the break location and size). The following distinct flow stages will occur after the initiation of the DEGB: depressurization, air ingress by lock-exchange flow, molecular diffusion of air and helium and finally natural circulation (Figure 15). The blowdown phase is very rapid, typically in order of several seconds, and continues until pressure equilibrium in the system is reached. Once the pressure is unified, the air ingress phase driven by the fluid density gradient (horizontal lock-exchange flow) starts. After the ingress of cold air into the lower plenum, the cavity gases will mix with the hot helium. When enough air from the cavity enters the lower plenum and fills it up to the point above cross duct upper elevation, a thermally stratified layer will be created between the cold air and the hot helium from the reactor core. At this interface air slowly diffuses into the helium. When gases concentration begins to equilibrate, natural circulation starts. [45, 66]

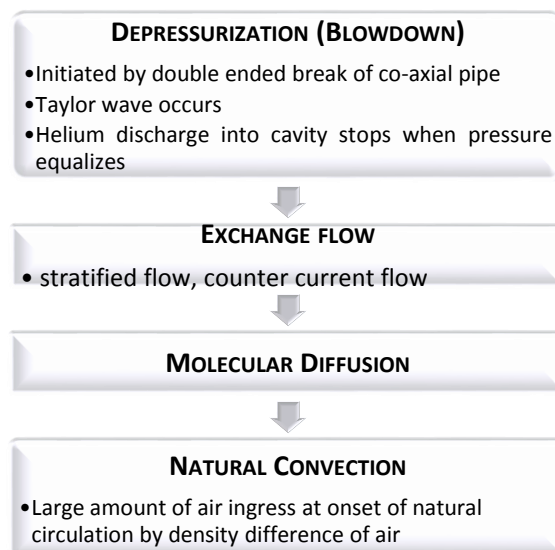


Figure 15 D-LOFC flow path in VHTR.

4.1. Depressurization

In this section a thermodynamic, zero-dimensional model of adiabatic blowdown is presented. Even though, a reversible process assumption is a great simplification of the analyzed phenomena, the purpose of this section is to present the general trends of the pressure changes that the HTTF will face during the depressurization experiment along with equations that describe the phenomena.

The mass conservation equation for the HTGR vessel undergoing a depressurization event as a consequence of double ended guillotine break is given by equation:

$$\frac{dM_{g,vessel}}{dt} = -\dot{m}_{Brk} \quad (29)$$

where \dot{m}_{Brk} is the mass flow rate through the break and $M_{g,vessel}$ is the mass of gas in the vessel.

The energy conservation equation for the gas in the vessel (neglecting heat transfer contribution and assuming isentropic process) is expressed in equation:

$$\frac{dU_{g,vessel}}{dt} = -\dot{m}_{Brk}h_{g,vessel} + P_{vessel}\frac{dV_{g,vessel}}{dt} \quad (30)$$

where h_g is gas enthalpy:

$$h_g = e_g + Pv_g \quad (31)$$

Analogous equations for mass and energy conservation can be written for the cavity.

The specific internal energy and the specific volume of the gas inside the control volume are defined respectively as follows:

$$e_g = \frac{U_g}{M_g} \quad (32)$$

$$v_g = \frac{V}{M_g} \quad (33)$$

The total change in specific internal energy of the gas inside the control volume is written in terms of partial differentials with respect to pressure and specific volume as shown in equation:

$$de_g = \left(\frac{\partial e}{\partial P}\right)_{v,g} dP + \left(\frac{\partial e}{\partial v}\right)_{p,g} dv_g \quad (34)$$

Using the ideal gas equation, partial differentials can be further written in the following form:

$$\left(\frac{\partial e}{\partial v}\right)_{p,g} = \frac{P}{\gamma_g - 1} \quad (35)$$

$$\left(\frac{\partial e}{\partial P}\right)_{v,g} = \frac{v}{\gamma_g - 1} \quad (36)$$

where γ_g is the ratio of the specific heats and v refers to specific volume.

Combining mass and energy conservation equations for vessel depressurization, one can arrive with the following formulae:

$$M_{g,vessel} \left(\frac{\partial e}{\partial P}\right)_{v,g,vessel} \left(\frac{dP}{dt}\right) = -(\dot{m}_{Brk}) \left(h - e + v \left(\frac{\partial e}{\partial v}\right)_p \right)_{g,vessel} \quad (37)$$

Using the ideal gas equation, partial differential equation 37 can be further written in the following form:

$$M_{g,vessel} \left(\frac{v}{\gamma_g - 1} \right) \left(\frac{dP}{dt} \right) = -\dot{m}_{Brk} \left(e + Pv - e + v \left(\frac{P}{\gamma_g - 1} \right) \right)_{g,vessel} \quad (38)$$

Further, simplifying for dP:

$$dP = \frac{-\dot{m}_{Brk} P \gamma_g}{M_{g,vessel}} dt \quad (39)$$

Choked flow occurs for helium flows when the ratio of the absolute upstream pressure to the absolute downstream pressure is equal to or greater than 2.049. A condition was set on the break mass flow rate to take into account whether the flow is choked or unchoked. For a choking condition, starting from the energy conservation equation, helium mass flow rate was found from the following formulas:

$$\dot{m}_{Brk} = A_{brk} \frac{P_{vessel} \sqrt{\gamma_g * \left(\frac{2}{\gamma_g + 1} \right)^n}}{\sqrt{CF_{g,vessel} T_{vessel}}} \quad (40)$$

$$n = \frac{\gamma_g + 1}{\gamma_g - 1} \quad (41)$$

where CF states for the gas compressibility factor and A_{brk} is the break cross section area. For non-choked flow, mass flow rate was derived from Bernoulli equation.

Applying forward Euler method (explicit) to iterate pressure over time, it is possible to follow the pressure changes in the system and extract the time when

the pressures will equalize. An analogous strategy can be applied to derive cavity pressurization equation.

The figure below presents results from the Matlab code simulation. The system pressure equalizes at around 1 sec from the beginning of the transient at pressure equal to 147 kPa.

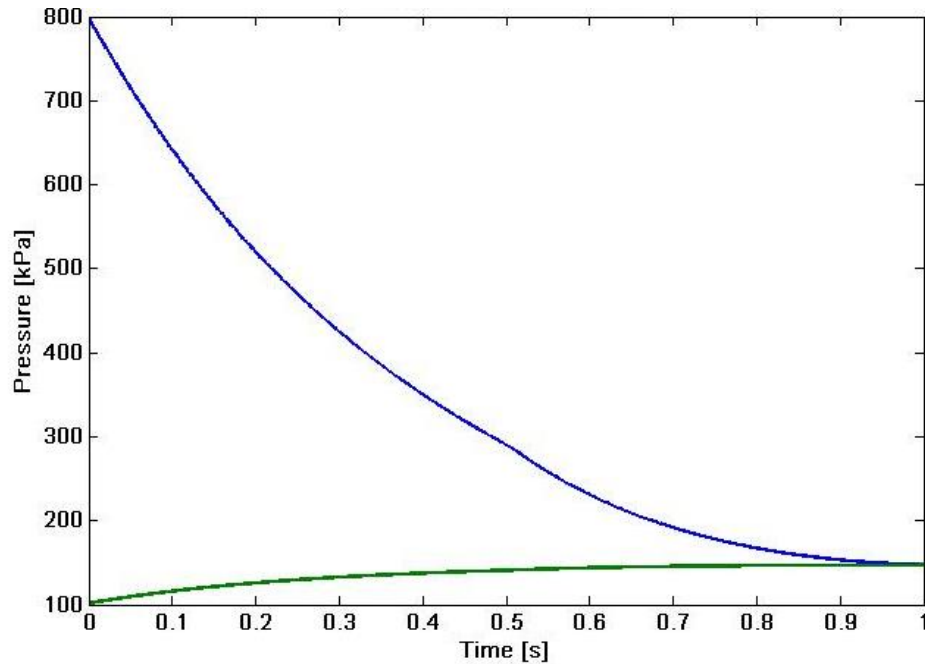


Figure 16 Pressure changes in the HTTF vessel (blue line) and cavity (green line) from Matlab simulation

4.2. Lock exchange flow

An analytical solution was introduced to quantify the time scale of the stratified flow stage and velocity of the air nose (heavy current). To estimate the convective time scale of the gravity current, the simplified convection-diffusion equation (species transport equation) is applicable [66, 96]:

$$\frac{\partial C_{He}}{\partial t} = -v\nabla C_{He} + D_{Air-He}\nabla^2 C_{He} \quad (42)$$

where:

C - gas concentration [$\frac{kmol}{m^3}$], t - time (total time that incorporates convection and diffusion time scales) [s], v - velocity [$\frac{m}{s}$], D - diffusion coefficient [$\frac{m^2}{s}$].

In equation (42) the first term on the right hand side represents the share of convection in the transport equation, which will be gravity current in this case.

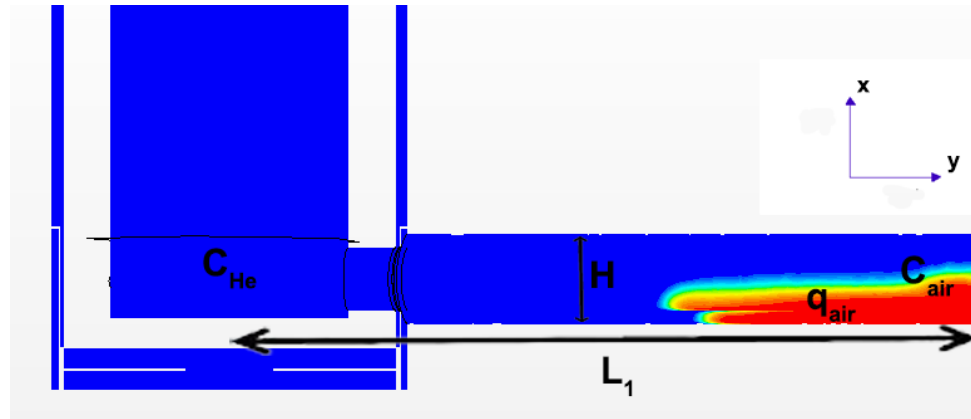


Figure 17 Gravity current flow with nomenclature used in the text.

Neglecting the x and z -directional flow and considering the stage presented in Figure 17, the average time scale for the stratified flow (sf) stage can be approximated as follows [66]:

$$\Delta t_{sf} \sim \frac{L_1}{v_x} \quad (43)$$

where: L_1 - refers to convection length scale [m] (distance between the break and center of the lower plenum, equal to 3.57 m).

Taking into account only inner duct diameter (0.3 m), as a channel height ($H=d$), and gas densities [42, 49]:

$$\rho_{air,cavity} (T = 293 \text{ K}, p = 101325 \text{ Pa}) = 1.206 \frac{\text{kg}}{\text{m}^3} \quad (44)$$

$$\rho_{He,vessel} (T = 960 \text{ K}, p = 101325 \text{ Pa}) = 0.052 \frac{\text{kg}}{\text{m}^3} \quad (45)$$

the density ratio of air and helium is equal to 0.043 that is categorized as non-Boussinesq flow, therefore equation (10) should be used to estimate the current speed.

To estimate the stratified flow time scale, Oh et al. (2011) proposes to use normalized current depth (h/H) to calculate air leading edge velocity and account for the fact that only part of the channel cross section is occupied by air [66]:

$$v_x = \frac{u_x h}{H} \quad (46)$$

Figure 18 presents time scale as a function of the normalized current depth for the calculated approaching current speed. If density ratio is close to zero value, then time scale asymptotically goes to infinite value. Exchange flow CFD simulation results provided in chapter 6. will be compared with this analytical solution. The applicability of the similarity of liquid and gases in the boussinesq/non-boussinesq approach will be investigated.

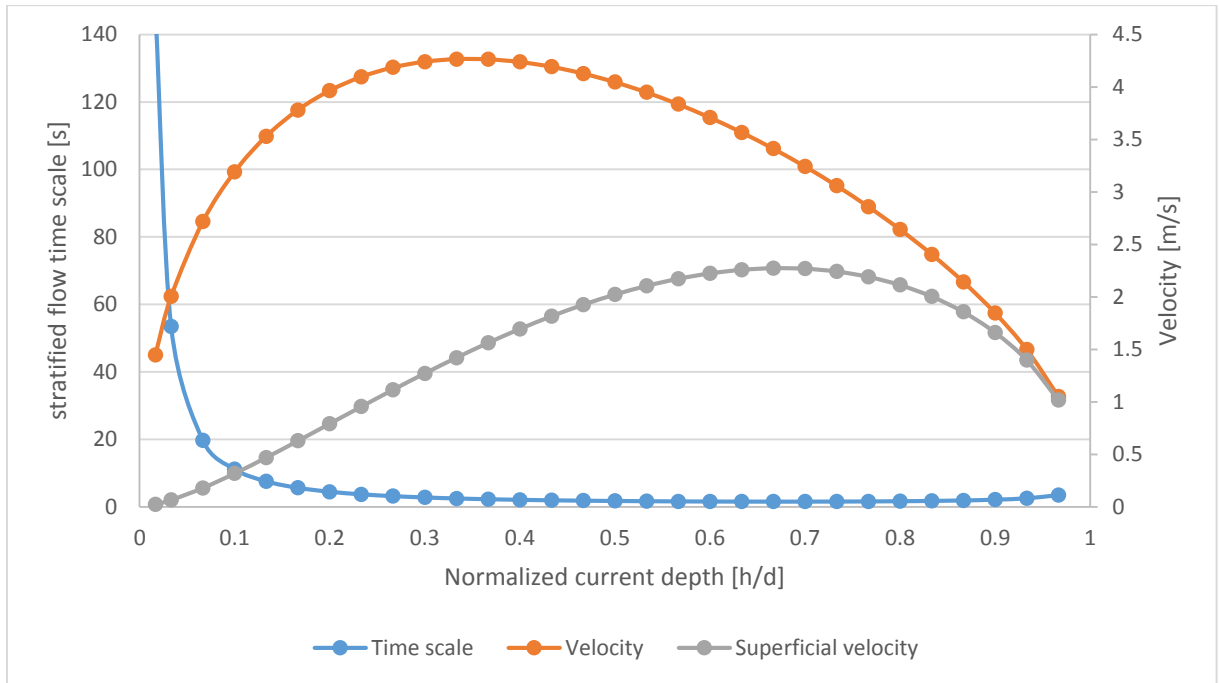


Figure 18 Stratified flow time scale and velocities as a function of normalized current depth.

To examine if portion of air will manage to enter core volume during Stage 2 stratified flow, Oh et al. condition given in equation (10) will be investigated.

5. CFD modeling

5.1. Governing Equations

The basic governing equations solve by the CFD solvers are the continuity equation, momentum conservation equation, an energy conservation equation, and a species conservation equation. The mass conservation or the continuity equation is given by [96]:

$$\frac{\partial \rho}{\partial t} + \nabla \cdot (\rho v) = 0 \quad (47)$$

Mass conservation equation is the general form of the continuity equation and is valid for both compressible and incompressible flows. Secondly, the momentum conservation, or momentum equation, is the concept of Newton's second law of motion. The momentum equation is given by [96]:

$$\frac{\partial \rho v}{\partial t} + \nabla \cdot (\rho v v) = -\nabla P + \nabla \cdot \tau + \rho g + F \quad (48)$$

where ρg and F terms are the gravity force and external force. τ is the shear stress tensor, defined as [96]:

$$\tau = \mu \left[\nabla v + \nabla v^T + \frac{2}{3} \nabla \cdot v I \right] \quad (49)$$

Subsequently, the energy conservation, or energy equation, is described by [96]:

$$\frac{\partial}{\partial t} (\partial q E) + \nabla \cdot (v (q E + P)) = \nabla \cdot (k_{eff} \nabla T - \sum_j h_j J_j + (\tau_{eff} \cdot v)) \quad (50)$$

where the total energy E and entropy h are shown are respectively [96]:

$$E = h - \frac{P}{\rho} + \frac{v^2}{2} \quad (51)$$

$$h = \int_{T_{ref}}^T C_{pj} dT \quad (52)$$

Equation of State is the equation that describes the relationship of density, temperature and pressure. If the fluid is considered as the ideal gas, density will be written in a simple relationship with pressure and temperature as [96]:

$$\rho = \frac{P}{RT} \quad (53)$$

5.2. Solver settings

To set up CFD solver, selection of relevant methods and convergence criteria have to be applied. The solution method includes the way in which the solver will solve governing equations. For the depressurization study, the coupled flow solver was implemented. The Coupled Flow model solves the conservation equations for mass and momentum simultaneously using a time-marching approach. The preconditioned form of the governing equations used by the Coupled Flow model makes it suitable for solving incompressible and isothermal flows. One advantage of this formulation is its robustness for solving flows with dominant source terms, such as rotation. Another advantage of the coupled flow solver is that CPU time scales linearly with cell count; in other words, the convergence rate does not deteriorate as the mesh is refined. [8]

In the blowdown simulation, it is useful to adjust the time-step according to the Courant number, velocity and/or cell size. For example, if the simulation is unstable at the beginning, a smaller time-step can be used for the start, and once the simulation has stabilized, the time-step can be increased. To use a variable

time-step, it must be defined as a field function in the STAR CCM+ solver. From the definition of the Courant number, time step can be derived:

$$CFL = \frac{v\Delta t}{\Delta x} \quad (54)$$

The velocity, Courant number and cell-Size in the above equation can be defined as follows:

1. Velocity: maximum velocity of the regions.
2. Cell-Size: minimum cell size of the regions.
3. Courant Number: define a target Courant number.

Using these definitions, time step adjustment in the depressurization case was implemented.

The Segregated Flow model was selected for exchange flow analysis. This solver solves the flow equations (one for each component of velocity and one for pressure) in a segregated or uncoupled manner. The linkage between the momentum and continuity equations is achieved with a predictor-corrector approach. This model has its roots in constant density flows. Although it is capable of handling compressible flows and low Rayleigh number natural convection, it is not suitable for capturing shock-waves, high Mach number flows, and high Rayleigh number applications. In stratified flow modeling, time step equal to 0.025 sec was selected. [8]

Second order temporal resolution was selected to model time discretization. This way, solution is based on the second order forward prediction by application of the last two time step results. [8]

5.3. Geometry

CFD simulations of an entire Nuclear Power Plant (NPP) or even an entire reactor core, requires powerful computing servers which are still not commonly available. Using available computing power with detailed models of system components, results in very time-consuming simulations [34]. In order to that, computationally feasible assumptions concerning simplifications of the systems geometry were made:

1. Core and Lower Plenum are modeled as porous bodies.
2. Bypass gaps in the core blocks were neglected to avoid computational limit.
3. No jagged edges at wall structures (lower plenum and core are hexagonally shaped).
4. No instrument controls included.

The 3D, full-scale geometry represents the HTTF hot duct, vessel (lower plenum, core, upper plenum, upcomer, MCSS: Metallic Core Support Structure) and cavity (Figure 19). Helium volume in the reactor vessel is around 3.2 m^3 , while cavity volume is equal to 18.5 m^3 . Duct length is set to 3.08 m. Outer duct diameter equals 0.4 m, while inner duct diameter is equal to 0.3 m. Only fluid regions were modeled and exported in the form of parasolid geometry to STAR CCM+.

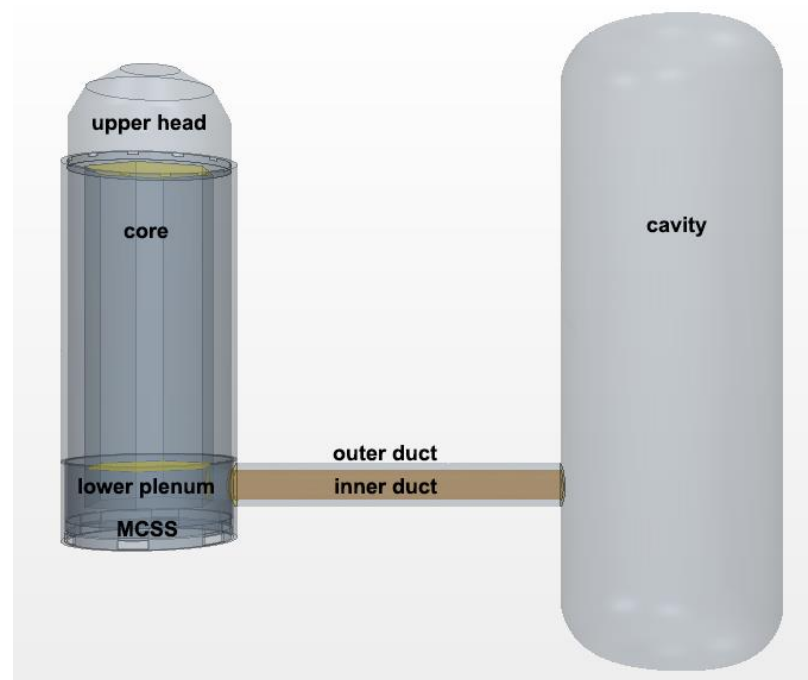


Figure 19 CFD geometry model.

5.4. Initial and boundary conditions

The HTTF operating pressure and temperature are 0.8 MPa and 960 K. The system will depressurize to atmospheric conditions (set in the cavity: $p=1\text{atm}$, $T=293\text{ K}$). At the beginning of the simulation, the vessel contains 100% helium while the cavity stores only air. Originally HTTF will simulate exchange flow with nitrogen instead of air, to prevent facility from structural degradation that would happen if experiments would be performed with air. In this study, air is used to stay with consistency with VHTR working fluids. To initiate double ended guillotine break, field functions are applied to assign different initial conditions for the cavity and vessel parts of the system. These functions simulate interface that divides the system into two domains characterized by different pressures, gases and temperatures. Details of field functions expressions can be seen in Table 4.

Heat transfer model between the reactor internal components and the helium coolant is not implemented in this simulation. The graphite core is characterized

by its high thermal capacity that results in a relatively long thermal response during loss of coolant accidents (the maximum fuel temperature is not reached for approximately 48 hours from the initiation of the accident). Therefore, it is assumed that heat transfer contribution will not have an impact on the system response during sufficiently short time scales. Core and vessel temperature changes as a function of the D-LOFC time (with and without operating RCCS) are presented below [69]. One can notice that temperature changes are measured according to hours from the beginning of the transient (Figure 20). This is way, assuming constant temperatures and neglecting conjugate heat transfer contribution, seems reasonable for the time scale that includes minutes after break initiation.

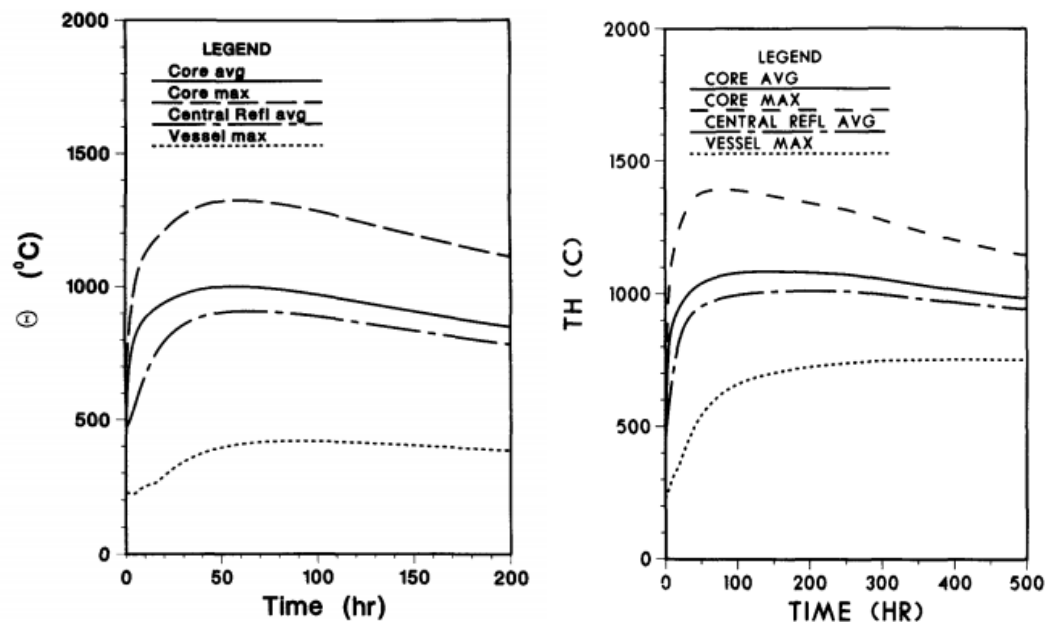


Figure 20 Core and vessel temperatures during D-LOFC with RCCS Cooldown (left) and without operating RCCS (right). [69]

Adiabatic boundary conditions are used for the majority of walls, with the exception of interfaces among regions. For the interfaces among duct, vessel, core,

lower plenum and cavity, the internal interface boundary condition was used (transfers solution from one domain to another without modifications).

One thing to underline is that this simulation assumes conservative approach of the exchange flow phenomena because of the assumption of 100% of air in the cavity at the beginning of the simulation. Increasing the air mass fraction increases the air-ingress speed because the density gradient among air and helium is increased for the higher air concentrations at the same temperature gradient. Since density gradient is the driving force in the exchange flow phase, therefore the most conservative case was selected as the initiating condition in the modeled domains, to account for the effect of the most severe conditions.

Table 4 Depressurization case initial conditions.

	Pressure [MPa]	Temperature [K]	Fluid
Vessel (upcomer, upper plenum, MCSS)	0.8	523	Helium
Cavity	0.1	293	Air
Core	0.8	960	Helium
LP	0.8	960	Helium
Inner duct	$(\$Centroid[2] > 1.3748) ? 800000 : 101000$	$(\$Centroid[2] > 1.3748) ? 960 : 293$	$(\$Centroid[2] > 1.3748) ? 0 : 1$
Outer Duct	$(\$Centroid[2] > 1.3748) ? 800000 : 101000$	$(\$Centroid[2] > 1.3748) ? 523 : 293$	$(\$Centroid[2] > 1.3748) ? 0 : 1$

For the analysis of exchange flow stage initial conditions were analogous to those presented in Table 4, only pressure in the system was unified to 0.1 MPa.

In the simulations that involve air ingress mitigation concept investigation, several cases were considered:

1. Influence of injected gas: helium, nitrogen and argon.

2. Influence of injection velocity: 0.0, 0.5, 1.0, 2.0 m/s.
3. Influence of flow rate of the injected gas (change with the increase in injection diameter).
4. Impact of injection placement: side, bottom and simultaneous side and bottom lower plenum injections (Figure 21).

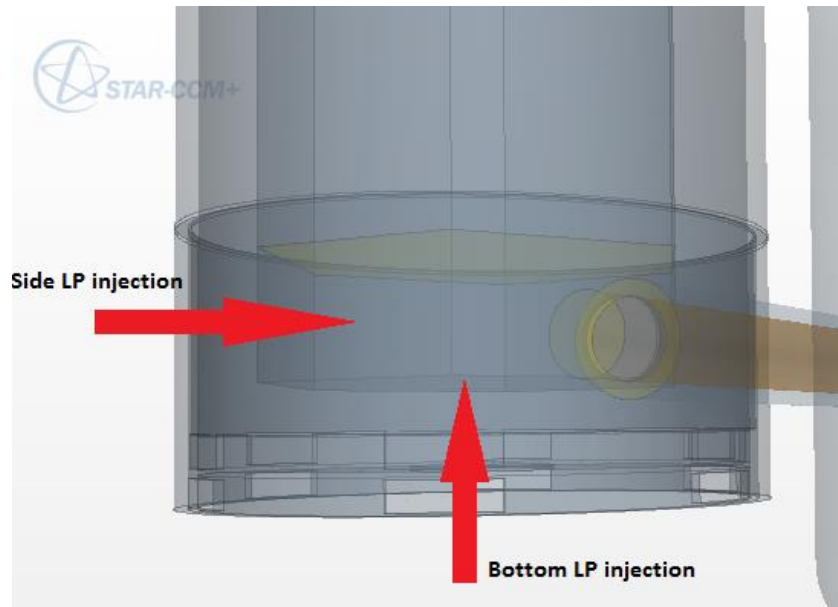


Figure 21 Placement of the lower plenum secondary gas injections, schematic view.

5.5. Porous body model

The internal structure of the HTTF is complex for the detailed CFD simulation. HTTF core itself contains 210 heater rods channels and over 516 coolant flow channels (Figure 22). It is also difficult to provide a detailed model of the lower plenum (with 163 support columns), especially if the analysis is not limited to the plenum model explicitly. Besides, the design of channel transitions between the core, reflectors and lower plenum blocks is very sophisticated and introduces additional complexity to the CFD modeling. Another factor that would contribute to the simulation complexity is the length to diameter ratio of the coolant channels which is around 100 in the HTTF design. The coolant bypass flow in the spaces among the fuel elements in each block further complicates the thermal-hydraulics

analysis of the core. Although direct numerical simulations of transport phenomena is theoretically possible to complete, it requires comprehensive computational resources (highly parallelized computation capabilities and a relatively long time: weeks to months) even for simple geometries [55]. Thus it was decided to model the core and lower plenum according to porous media approximation and reduce the number of mesh nodes and computational time required to accurately simulate the transient.

For the prismatic block core the pressure drop across the core consist of frictional losses, form losses and acceleration losses due to gas expansion. The largest contributor to the head loss in the VHTR core is the frictional pressure drop caused by the gas flow through the coolant channels.

The pipe head loss according to the Darcy-Weisbach's formula (for ducts flows of any cross section and for turbulent and laminar flows) is applicable [86]:

$$\Delta p = f \left(\frac{1}{2} \rho u^2 \right) \left(\frac{L}{D} \right) \quad (55)$$

According to the STARCCM+ User Guide [9], the porous medium approach can be adapted in the simulations that include: packed beds, filters, perforated plates, flow distributors, and tube banks. The porous media model incorporates additional flow resistance in a region of the model defined as “porous”. In CFD simulations involving porous media assumption, the details of the internal flow are not the major point of the simulation. The need is to properly resolve the macroscopic fluid behavior in the modeled domain. In essence, the porous media approach adds a momentum sink in the governing momentum equations [8]:

$$S_i = -\left(\sum_{j=1}^3 D_{ij} \mu v_j + \sum_{j=1}^3 C_{ij} \frac{1}{2} \rho v_{mag} v_j\right) \quad (56)$$

where:

S_i - source term for the i th (x, y, z) momentum equation,

v_j - velocity component in the j th (x, y, z) direction,

v_{mag} - velocity magnitude,

D_{ij} - tensor, viscous resistance factor,

C_{ij} - tensor, internal resistance factor,

μ - fluid viscosity.

For the simple homogeneous porous media, above equation simplifies to:

$$S_i = -\left(\frac{\mu}{\alpha} v_i + C_2 \frac{1}{2} \rho v_{mag} v_i\right) \quad (57)$$

where:

α - porous region permeability ($D_{ii} = \frac{1}{\alpha}$).

Experimental simulation results of the pressure drop over a range over flow rates have to be provided in order to calculate the pressure drop dependency as a function of the characteristic velocity through the structure (or alternatively existing empirical relationships for such dependency). Obtained function must be then fitted to the quadratic formulation of the pressure drop per unit length, introduced with the following equation [8]:

$$\frac{\Delta p}{L} = -(P_i |v| + P_v) v \quad (58)$$

where:

v - superficial velocity through the medium (actual velocity times volume porosity),

P_i - internal resistance coefficient,

P_v - viscous resistance coefficient.

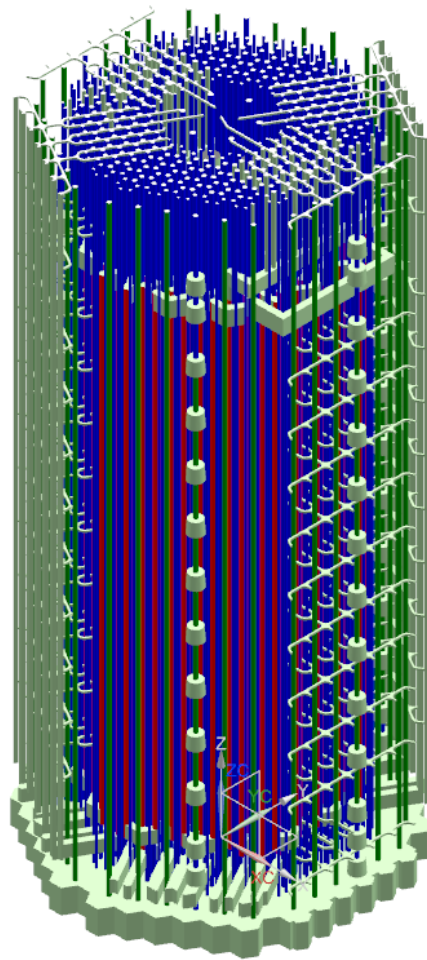


Figure 22 HTTF core internal flow patch.

By inserting equation (55) to equation (57) and comparing with equation (56), formulas for the unknown coefficients can be found.

The main values that should be set for a porous region are: porosity and the inertial and viscous coefficients required for the porous source term definition in the momentum equation.

Porosity is the volume fraction of fluid in the total volume of the modeled structure (fluid and solid). In Star-CCM+ porosity, is an additional input that is required for unsteady flow calculations that defines the ratio of open volume to total volume within the porous medium. This is used in the time derivative terms of the continuity, energy, and species equations [8]. Porosities of the core and lower plenum zones were derived separately. Porosities of the core and lower plenum are:

$$\gamma_{core} = \frac{V_{fluid,core}}{V_{fluid+structures,core}} = \frac{V_{coolant\ channels,core}}{V_{fluid+structures,core}} = 0.09085 \quad (59)$$

$$\gamma_{LP} = \frac{V_{fluid,LP}}{V_{fluid+structures,LP}} = \frac{V_{fluid+structures,LP} - V_{LP\ posts}}{V_{fluid+structures,LP}} = 0.5512 \quad (60)$$

The inertial and viscous resistance coefficients control the flow resistance over the porous medium. Porous internal and viscous resistances were determined separately for core and lower plenum regions as well. In the core region these parameters were introduced only in vertical direction (no cross flow is assumed between coolant channels). A different approach is established in the lower plenum model. A unidirectional flow assumption is not valid here, because lateral flow (normal to lower plenum posts axis) plays significant role in the overall lower plenum flow. This is why porous body parameters are set also for x,z-directions in the lower plenum region. [92]

Since no experimental data were available for the pressure drop as a function of coolant velocity, estimation of the coefficients in vertical direction was made by

friction factor curve fitting to Moody diagram (Figure 28) by equation (56). The Moody chart presents friction factor dependency on the Reynolds number with reference to the wall relative roughness. This chart is commonly used in fluid mechanics applications. Its accuracy is around $\pm 15\%$ and can be used for circular and noncircular pipe flows and for open channel flows [96].

In the lower plenum lateral direction, the flow can be considered as a flow across large tube bank. Zukauskas correlated laminar and turbulent pressure drop for the in-line and staggered tubes (Figure 23) arrays with the following equation [96]:

$$\Delta p = f \frac{N G_{max}^2}{2\rho} Z \quad (61)$$

where:

N – number of the tube rows in the direction of the flow,

Z - correction factor depending on the array arrangement,

G_{max} - maximum mass flux.

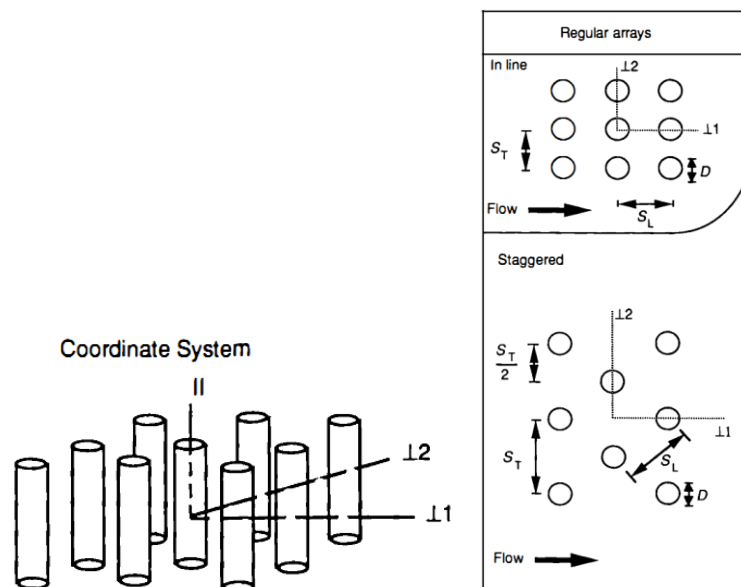


Figure 23 Schematic view of the staggered tube arrangement. [96]

In the symmetrical staggered tube bank $S_T=S_D=0.09m$ and correction factor $Z=1$. Since lower plenum support post diameter equals 0.057 in and in this case is equal to 1.58 , thus fitting curve (Figure 26) was found by correlation to the curve drawn for $X_T=1.5$ on the Zukauskas chart (Figure 28).

It should be underlined that in case of the lateral flow through the tube bank, standard friction factor correlation (equation (55)) must adopt modified volumetric hydraulic diameter expressed as follows [86]:

$$D_{v,LP} = \frac{4 \cdot \text{free volume of posts bundle}}{\text{friction surface area of posts}} = 0.4368\text{ m} \quad (63)$$

Considering lower plenum cross flow:

$$f_{core} = a_{core} + \frac{b_{core}}{Re_{core}} = 0.017 + \frac{79}{Re_{core}} \quad (64)$$

To designate the approximation of the pressure drop correlation using the Moody chart, wall roughness must be a known value. The HTTF core block is made of the Green Cast 94F plus material. This type of ceramics is used in the high temperature burner blocks or high temperature thermal combustors (with maximum service temperature of 1870°C). It consists mainly of alumina (96.5%) and Lime (3%). Average wall roughness height for the core block coolant channel was found to be around 0.008 mm (two sample channels in the core block were measured with digital microscope). Applying average coolant channel diameter (14 mm), relative wall roughness is found to be equal to 0.00057 .

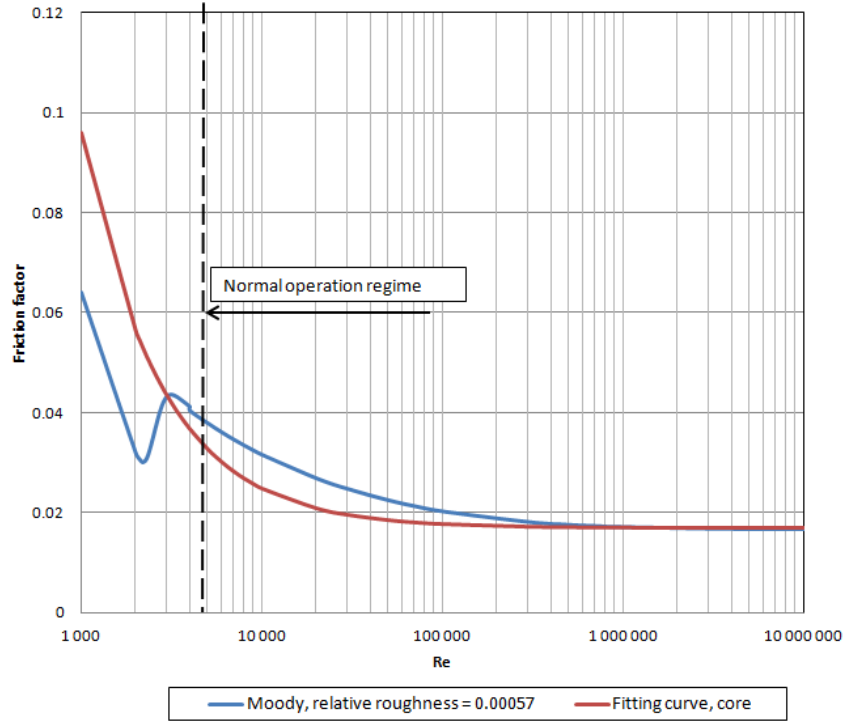


Figure 24 Fitting curve for the core porous body model implementation, Moody diagram.

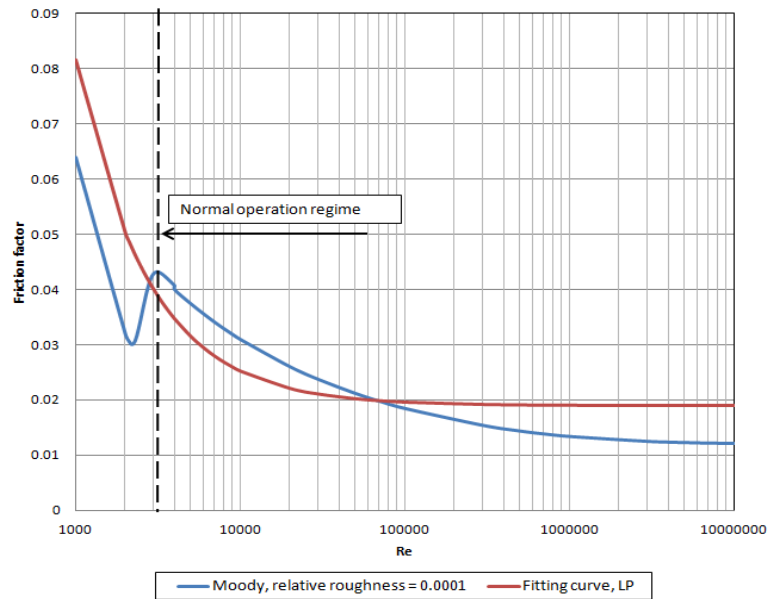


Figure 25 Fitting curve for the lower plenum porous body model implementation, Moody diagram.

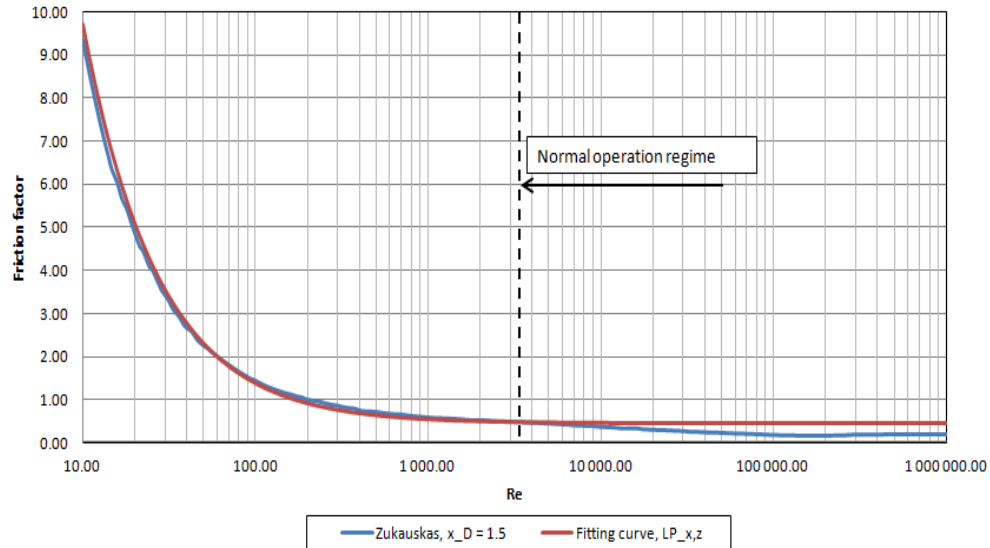


Figure 26 Fitting curve for the lower plenum porous body model implementation, Zakauskas diagram.

To restrict the flow in the cross-stream direction, the porous resistance, which depends on inertial and viscous resistance, must be a large value in the cross-stream. The following is recommended to make the cross-stream resistance sufficiently large: the cross-stream inertial resistance set to zero and the cross-stream viscous resistance to two orders of magnitude greater than resistances in the flow direction. Table 5 summarizes the porous body model parameters introduced in the simulation.[92]

Table 5 Details of porous body modeling: lower plenum and reactor core.

	Core		Lower Plenum	
	y	x,z	y	x,z
Data fitting	Moody	-	Moody	Zukauskas
Curve fitting	$f = 0.017 + \frac{79}{Re}$	-	$f = 0.019 + \frac{63}{Re}$	$f = 0.47 + \frac{93}{Re}$
Internal resistance [kg/m ⁴]	$1.21 \cdot 0.5 \cdot \rho$	0	$0.3 \cdot 0.5 \cdot \rho$	$1.07 \cdot 0.5 \cdot \rho$
Viscous resistance [kg/m ³ s]	$\mu/5.04 \cdot 10^{-6}$	∞	$\mu/1.25 \cdot 10^{-4}$	$\mu/4.1 \cdot 10^{-3}$
Porosity	0.10		0.55	

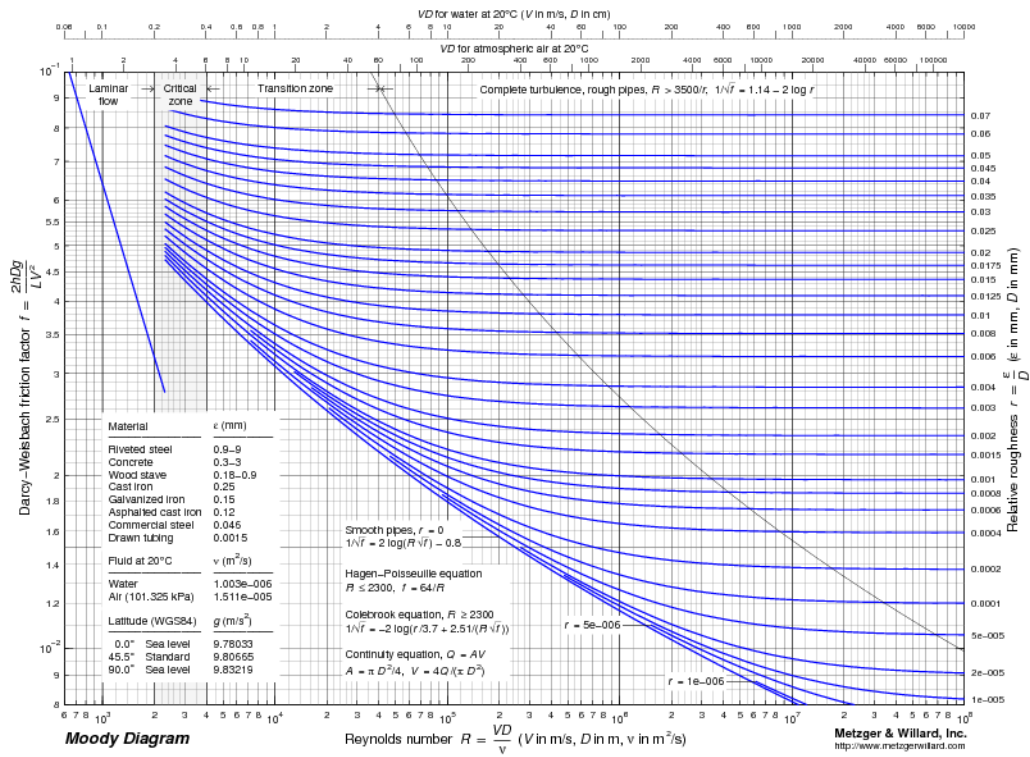


Figure 27 Friction factor (f) for the use in vertical channel flow arrangement.

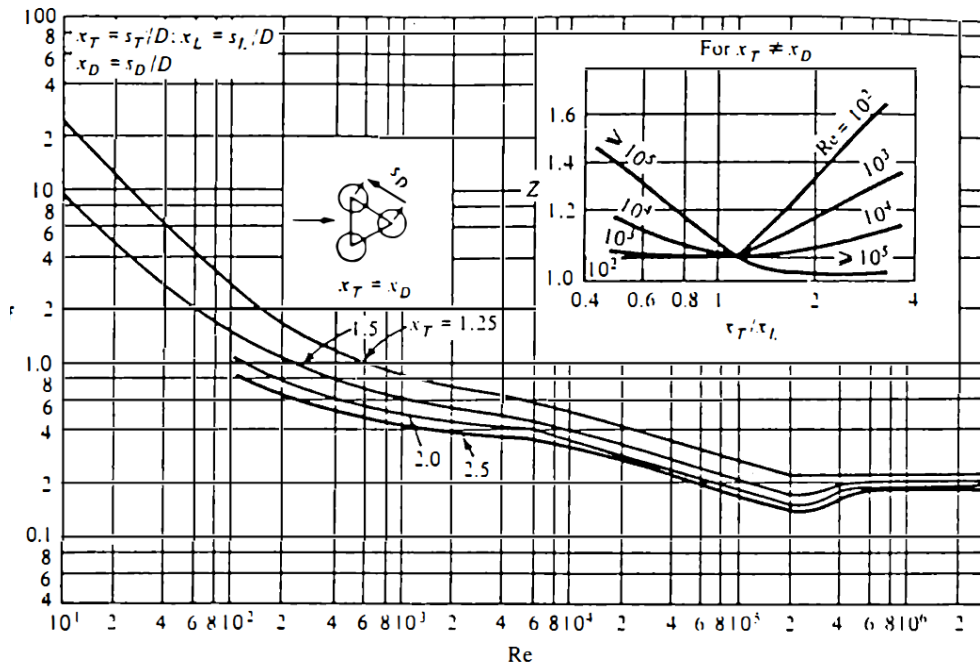


Figure 28 Friction factor (f) and the correction factor (Z) for the use for staggered tube arrangement.

After setting up a porous domain in the STAR CCM+ preprocessor, steady state analysis was run to check if the pressure drop in the reactor core, generated by the porous domain, stays within the range of value suggested by the General Atomics [52]. In the prototype reactor, pressure drop in the core should be equal to 31.0 kPa. Pressure drop across the HTTF core should be reduced by a factor of eight, thus equal to 3.875 kPa. According to the steady state analysis results of the core flow, pressure drop equals 1.788 kPa. Although this value is nearly two times smaller than the pressure drop suggested by the General Atomics it was decided to proceed with the simulations. Reason for that is that the pressure drop in the HTTF was not directly scaled and the HTTF designer's intent was to adjust the core and lower plenum pressure drops with insertion of additional flow orifices after obtaining first tests results on the reactor normal operation.

Porous body parameters for the prototype model were derived on the basis of values selected for HTTF model. Summary of MHTGR porous region setting is presented in Table 6.

Table 6 MHTGR porous model parameters.

Region, direction	Hydraulic Diameter [m]	Internal resistance [kg/m ⁴]	Viscous resistance [kg/m ³ s]
Core, y	0.0564	$0.3741 \cdot 0.5 \cdot \rho$	$\mu/9.7 \cdot 10^{-5}$
LP, y	0.25	$0.0785 \cdot 0.5 \cdot \rho$	$\mu/1.8 \cdot 10^{-3}$
LP, x,z	1.7472	$1.0721 \cdot 0.5 \cdot \rho$	$\mu/4.1 \cdot 10^{-3}$

5.6. Mesh model and refinement

The accuracy of the solution is governed by the computational grid. The size of the computational grid is usually coupled with the limitations of the computational resources. Fine mesh requires large resources (RAM, processors) and time to reach

a convergent solution. Hence the grid density is a trade-off between accuracy and available computational power to obtain a reasonable results. [87]

Geometry is discretized using the following meshing models: polyhedral mesher, prism layer mesher and surface remesher. In polyhedral mesh type, gradients can be better approximated that in for instance tetrahedral meshes, because polyhedral cell has many neighboring cells, typically of the order of 10. Previous research shows that an increased number of computing operations per cells (increased need for storage capability) is compensated by higher accuracy of obtained results. [87]

Polyhedral cells are especially beneficial for handling re-circulating flows. Comparisons in many practical tests have verified that, with polyhedral meshes, approximately four times fewer cells, half the memory, and a tenth to a fifth of computing time is required to achieve a solution as compared to a tetrahedral mesh – with the same level of accuracy. In addition, convergence properties are much better in computations on polyhedral meshes, where the default solver parameters usually do not need to be adjusted. [8]

Surface remesher was used to retriangulate the surface in order to optimize the quality of the volume mesh. Prism layer mesher is incorporated to generate prismatic control volumes near the wall boundaries. Along with the prism layer mesher, prism layer stretching and thickness can be defined. Prism layer stretching represents the thickness of the cell layer with reference to the adjacent layer beneath it. Therefore, the cell layers thickness increases with geometric progression: the further from the wall the thicker the prism layer is. The prism layer thickness refers to the thickness of the near-wall prism layer.

Solving for any type of CFD problem (steady/transient, laminar/turbulent, etc.) is computationally demanding. In essence, fine meshes are required to reduce the

numerical error associated with discretization of the analyzed domain. On the other hand such 'ideally' discretized regions would require highly efficient computational sources to generate the domain and furthermore, computational time will be significantly extended. Therefore, one aims to implement as simple computational grid as possible, while still capturing all of the details of the flow. [87]

Another important aspect to have in mind during generation of the meshed medium, is to check the cell quality or mesh validity. Face validity (FV) is an area-weighted measure of the correctness of the face normal relative to their attached cell centroid. Face validity of 1.0 means that all face normal are properly pointing away from the centroid (FV < 0.5 means that negative volume cells are present in the domain). Volume change metric (VC) describes the ratio of cells volume to that of its largest neighbor (VC=1.0 is the best case) [8]. All analyzed meshes, applied in this research, were topologically valid and had no negative volume cells. Five optimization cycles (recommended: 1÷8) were set during mesh generation along with the quality threshold equal to 0.5 (recommended: 0.4÷1) [8]. No cells with skewness angle above 90° were present. Look-up table for cells validity parameters is presented in Table 7. Faces validity and volume changes stays within the tolerance limits (all values are near unity). Taking this aspects into considerations, mesh sensitivity study was done to select appropriate size of computational mesh.

Table 7 Face validity and volume change statistics

Statistics	Range	Coarse	Medium	Fine
Face validity (FV) [%]	(0.7;0.8)	0	0	0
	(0.8;0.9)	0.064	0	0
	(0.9;0.95)	0.178	0.159	0.178
	(0.95;1.0)	99.758	99.841	99.822
Volume change (FC) [%]	(0.7;0.8)	0	0	0
	(0.8;0.9)	0.112	0.058	0.021
	(0.9;0.95)	0.566	0.365	0.31
	(0.95;1.0)	99.332	99.577	99.669

Summary of applied mesh sizes is given in Table 8. Three meshes were generated for the grid independence study: coarse, medium and fine. Different cell base sizes were selected for specific regions of the simulated domains (finer grid in the cross duct region, lower plenum, core and vessel while coarser in the cavity). The relative cell size, given in Table 8, is averaged among the whole computational grid and refinement factor refers to this value. Prism layers size in all regions was derived as a percentage of base size, equal to 33.3 % (default STARCCM + option) with stretching and growth ratio equal respectively 1.5 and 1.3. The following figures (Figure 29) shows the detailed, generated volume mesh (medium).

Table 8 Mesh sensitivity study details.

	# cells	Relative cell Size [m]	Refinement factor
Coarse	2438555	0.022	1.59
Medium	5634956	0.017	1.32
Fine	9908489	0.014	1.21

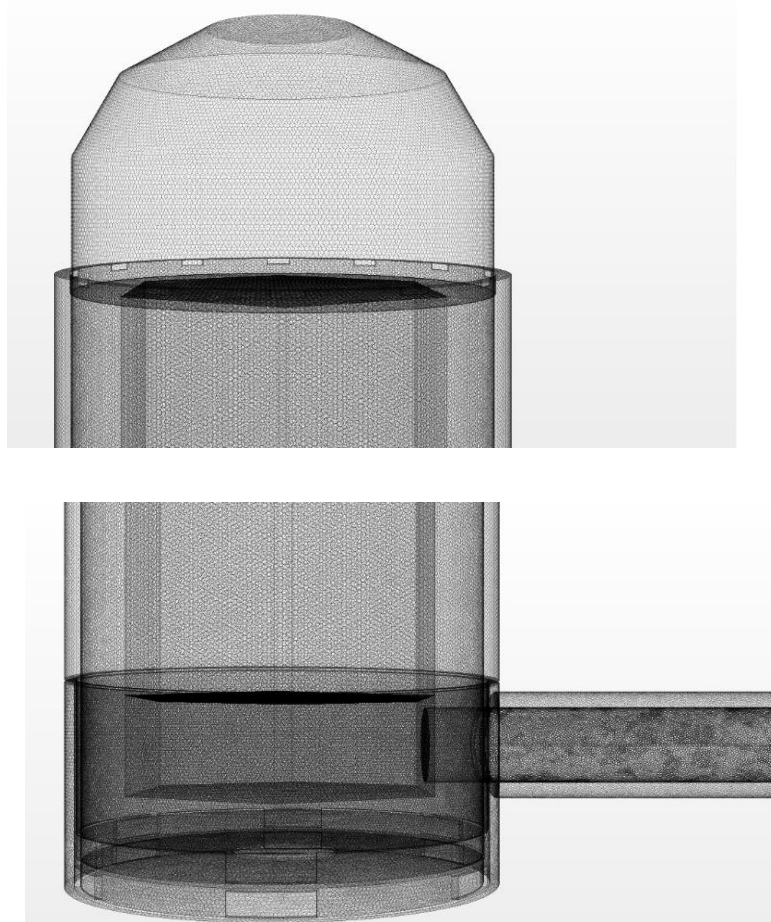


Figure 29 Detailed volume mesh on the selected domains (medium mesh).

Initial conditions for the exchange flow simulation were utilized. To evaluate grid convergence, a surface average mass fraction of air at Rake cross section as a function of time was investigated. Figure 30 shows surface average air concentrations at Rake plane section. According to the procedure described in the Chapter 2.6. the following figure presents also the extrapolated fine-mesh solution (representative for the asymptotic solution).

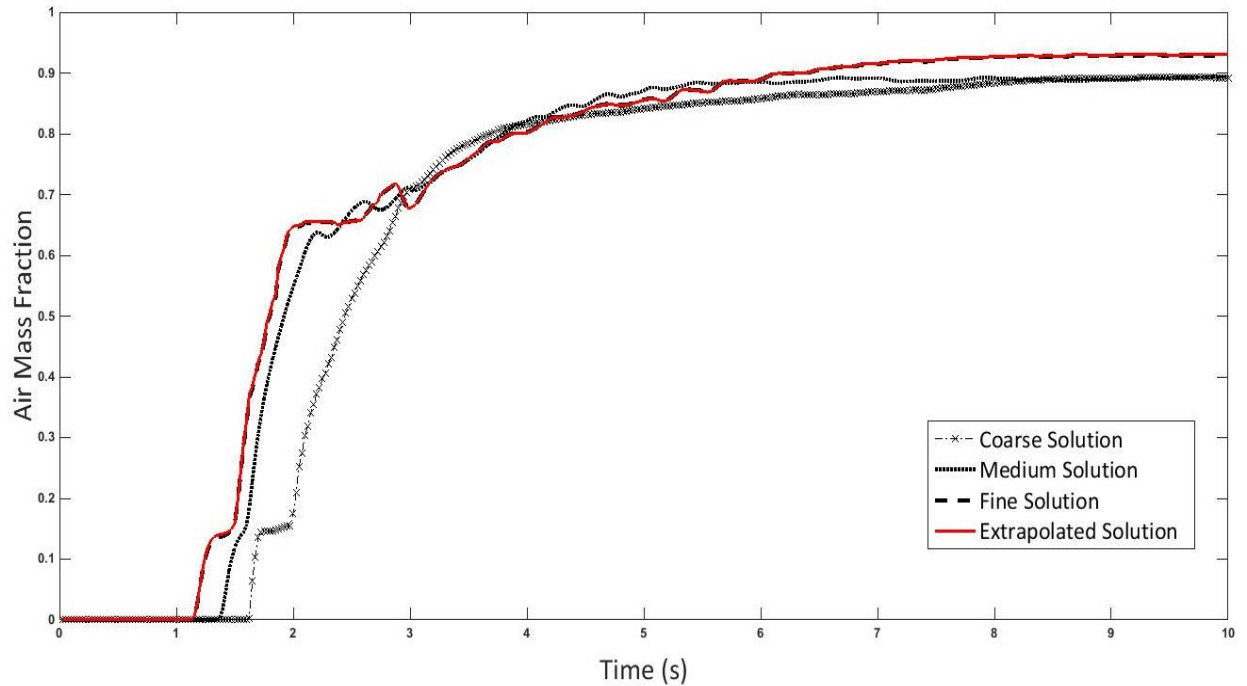


Figure 30 Surface average air mass fraction at Rake plane section for different meshes along with the extrapolated solution.

Before the air current will reach the Rake instrumentation plane, the surface concentration is equal to zero. In the three investigated meshes, air reaches analyzed surface at different times. The cold wave starts crossing the plane at 1.25, 1.35 and 1.625 sec, respectively for the fine, medium and coarse meshes. The extrapolated error that corresponds to different meshes is presented in Figure 31. At the solution time, when air reaches the Rake plane section, large concentration gradients occur which causes discrepancies among results obtained from the applied meshes. The maximum extrapolated error is equal to 12 % and subsequently asymptotically reduces to zero, as the simulation proceeds and concentration gradients are reduced.

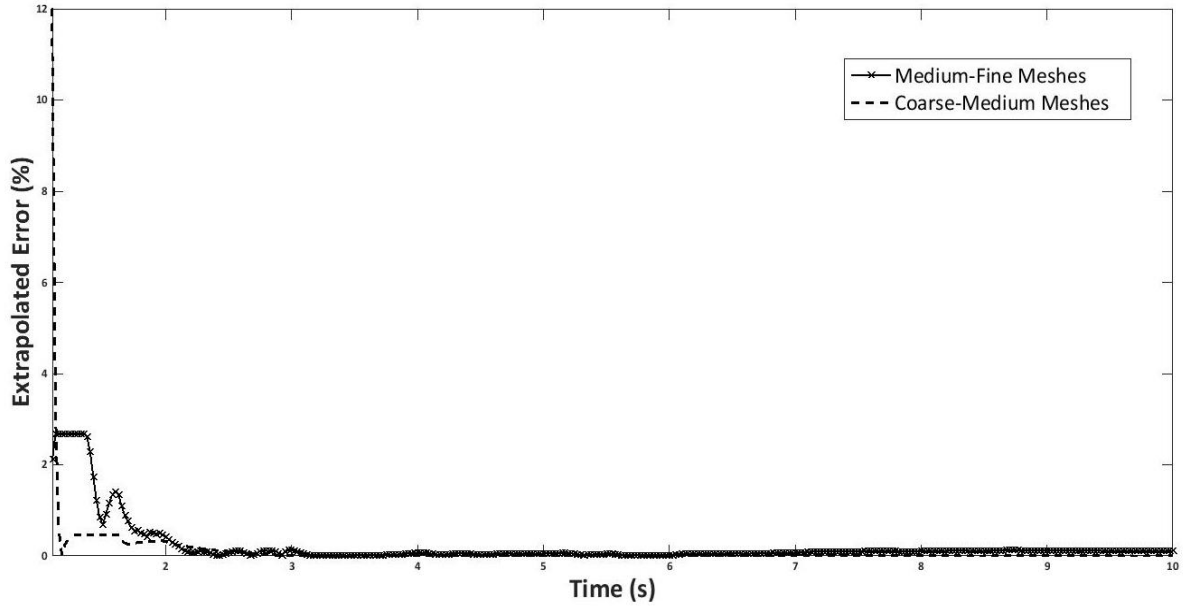


Figure 31 Extrapolated error between applied grids.

Grid convergence index is shown in the form of an uncertainty bands around the fine mesh solution. The highest uncertainty equals 3.4% and occurs again at the solution time, when air current reaches the Rake cross section plane.

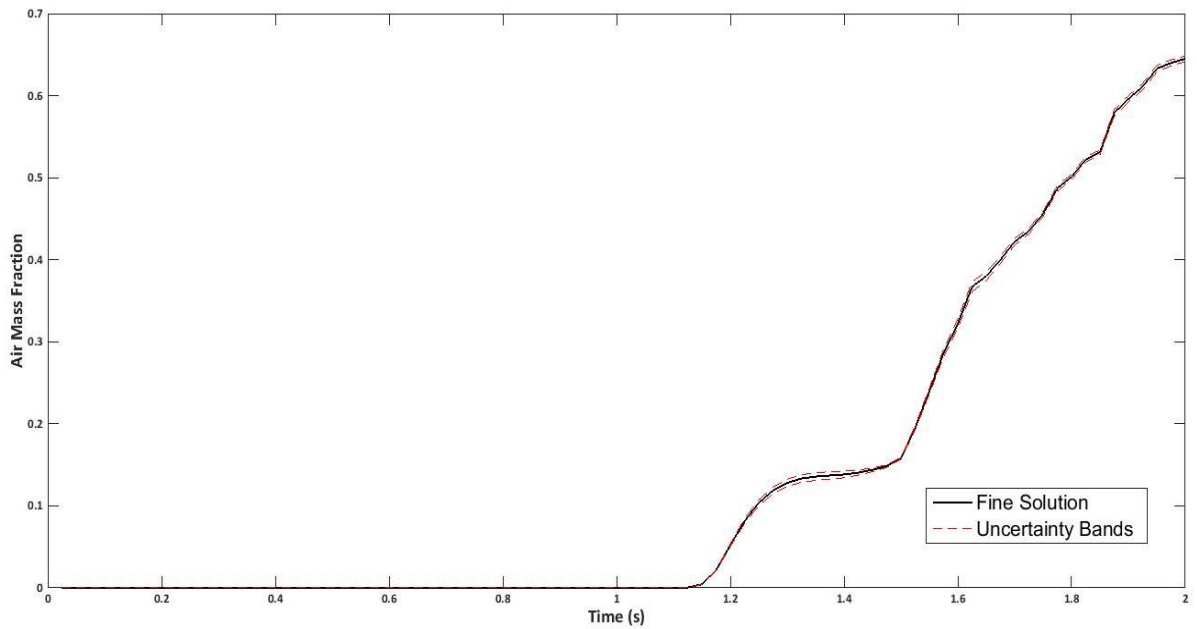


Figure 32 Fine solution uncertainty bands.

Having in mind the relatively small values of the extrapolated errors among obtained solutions and error band around the fine mesh solution showing that fine grid approaches the exact solution with small error associated with uncertainty bands, it was decided to select medium mesh for further analysis. Medium mesh averaged refinement factor differs from the fine mesh only by 0.1, but at the same time, number of cells in the domain is reduced by over 4.0 mln. Less expanded computational grid will provide savings with respect to computational power, memory and time. Details of medium mesh cells quantity and distribution is presented in Table 9.

Table 9 Details of cell quantity and placement, medium mesh, HTTF.

Region	Cells quantity	Cell base size [m]	Number of prism layers	Prism layers thickness [m]
Core	459 530	0.02	5	0.0067
Lower plenum	998 62			
Inner duct	549 065	0.01	8	0.0033
Outer duct	897 571			
Vessel	2 049 280	0.015	3	0.0049
Cavity	1 579 648	0.05	3	0.0173
Total	5 634 956			

In case of the MHTGR reactor analysis, cell base size in each region was increased. The resultant mesh consists of over 13.0 mln cells, with details provided in Table 10.

In the blowdown analysis, the simulation was very time consuming so the potential to run refinement study on the mesh size is reduced. Accordingly, the medium mesh (the same base size as in exchange flow study) is applied.

Table 10 Details of cell quantity and placement, medium mesh, MHTGR.

MHTGR Region	Cells quantity	Cell base size [m]	Number of prism layers	Prism layers thickness [m]
Core	2 611 380	0.04	5	0.0133
Lower plenum	530 012			
Inner duct	1 531 580	0.025	8	0.00845
Outer duct	2 314 619			
Vessel	4 753 067	0.04	3	0.0127
Cavity	1 385 869	0.10	3	0.0347
Total	13 126 527			

5.7. Turbulence sensitivity analysis

In CFD modeling, constant struggle concerns simulation of very complex phenomena using relatively simple tools and methods. Nowadays laminar flow theory is well developed but there are no straightforward tools that can simulate the fine-scale random fluctuations of the turbulent flows [43]. Complexity of turbulence modeling is challenging if one needs to explicitly capture details of relevant physics that includes highly unsteady, three dimensional, dissipative phenomena. Turbulent flows may be computed using several different approaches:

1. Reynolds-Averaged Navier Stokes (RANS),
2. Large Eddy Simulations (LES),
3. Detached Eddy Simulations (DES),
4. Direct Numerical Simulation (DNS).

RANS approach resolves large scale eddies in the modeled phenomena while short length scales are computed by introduction of additional term called Reynolds stresses.

DNS means numerical solving of continuity equation and Navier-Stokes equation, including all length and time scales of existing phenomena. This method, with ability to provide the most reliable results, requires very large computational power that is not commonly available. On the other hand, LES resolves large scale vortices while the smallest scales of the flow are modeled by subgrid scale models. Small scales eddies approximation allows to greatly reduce the computational cost comparing to DNS. DES is a modification of a RANS method in which the model switches to LES when eddies are enough small for a subgrid scale formulation applied in LES calculations. If turbulent length scale is smaller than the maximum grid size, then RANS is applied, otherwise LES is used. Therefore the grid refinement for DES is not as computationally demanding as LES method since it reduces detailed information about the flow. LES and DES on the other hand require greater computational power than RANS model, but are far less expensive than DNS. [43, 87]

This section will employ turbulence models for the RANS equations, since these type of models are utilized in the majority of production applications. Additional turbulent equations, solved within RANS are referred to by the number of transport equations that are solved in order to compute the model contributions. The least computationally expensive models are the algebraic (zero equation) models. This method is also called Mixing Length Model and it does not solve any additional transport equation. The most popular one equation model is Spalart Allmaras Model. It solves one additional transport equation to derive parameters required to calculate turbulent viscosity. Two equation turbulence models are one

of the most commonly used types of turbulence models. K-Epsilon and the K-Omega models have become standard models for industrial applications and are commonly adapted for vast types of engineering problems. [43, 87, 91]

5.7.1. K-Epsilon Models

K-Epsilon models are the most widely validated turbulence models. Together with very ease implementation, they became applicable in most of the industrial problems.

Standard K-Epsilon model employs two new transport equations that resolves turbulent kinetic energy, k , and eddy diffusivity, ε :

$$k = \frac{3}{2}(UI)^2 \quad (65)$$

$$\varepsilon = \frac{C_\mu^{0.75} k^{1.5}}{l} \quad (66)$$

where:

U – reference inlet velocity,

I – turbulent intensity,

C_μ – dimensionless constant = 0.09,

l – mixing length.

Standard K-Epsilon model leads to stable calculations that converge relatively easily in the area of reasonable applications of this model. It will not provide reliable predictions for swirling and rotating flows, flows with strong separation, axis symmetric jets or fully developed flows in non-circular ducts.

Realizable K-Epsilon model contains a new transport equation for the turbulent dissipation rate. Also, the dimensionless constant in the Standard model, is expressed here as a function of mean flow and turbulent conditions. Realizable

model provides improved performance on the prediction of the spreading rate of jets, flows involving rotations, boundary layers under strong adverse pressure gradients, separation and recirculation. [87]

The Two-Layer model combines the K-Epsilon model (realizable or standard) with the two-layer approach. The coefficients in the models are identical, but the two-layer approach, is an approach that allows the K-Epsilon model to become applicable in the viscous sublayer (laminar sublayer) range. Since fluid flow is static in contact with solid wall, viscous sublayer concept was introduced to resolve the viscous effects that dominate in this region. Thickness of this layer is very small, so a non-dimensionalized term: y^+ , is incorporated to represent distance from the wall surface. Above the viscous sublayer ($y^+ < 5$), in the buffer region ($5 < y^+ < 30$), the flow begins its transition to the fully turbulent regime ($y^+ > 30$) where the average flow velocity is related to the logarithm of the distance to the wall (log-law region). Further away, flow will transform to free stream region.

In the Two-layer approach, turbulent dissipation rate and the turbulent viscosity are specified as functions of wall distance. In STAR-CCM+, the two-layer formulations will work with either low-Reynolds number type meshes, with $y^+ \sim 1$, or for $y^+ > 30$ type meshes [8]. One should notice that wall functions ignore the flow field in the buffer region.

5.7.2. K-Omega Models

The Standard K-Omega model developed by Wilcox (1998) is a two-equation model that serves as an alternative to the K-Epsilon model. It employs the following transport properties: turbulent kinetic energy and turbulent frequency (dissipation rate per unit turbulent kinetic energy). It has been shown that K-Omega model performs very well in the vicinity of walls in boundary layer flows.

It presents additional advantage over the K-Epsilon approach because of higher performance for boundary layer flow in case of adverse pressure gradients. Conceivably the dominance of this model over K-Epsilon would reveal in the viscous-dominated regions modeling without a need for wall damping functions usage. K-Omega is useful in models where K-epsilon often does not provide accurate results, for instance: internal flows (such as flow through a pipe bend), strong curvature flows, jets and separated flows. Nonetheless, this model is highly sensitive to the free-stream value of the turbulent frequency. This means that solver setup faces strong dependence on inlet boundary conditions for internal flows. This issue does not take place in K-Epsilon approach. In general, the standard K-Epsilon model is less dependent on the free stream values but does not perform well under adverse pressure gradients, where K-Omega seems to be more applicable. [87]

5.7.3. Menter SST

To overcome this discrepancy, Menter SST (Shear Stress Transport K- Omega) model that is a combination of the K-Epsilon in the free stream and the K-Omega models near the walls can be applied. This model is able to eliminate sensitivity of the turbulence model on the free stream values retaining the K-Omega near-wall functionality. [87]

5.7.4. Turbulence sensitivity study results

This section presents the effects of turbulence models on the stratified flow simulation results. Together with the laminar case, four different models were taken under investigation: standard, realizable K-Epsilon models and SST, Wilcox K-Omega models. Relatively large differences are observed between the laminar and the turbulence models. Figure 33 shows volume average molecular fraction of

air in the core up to 30 sec from the beginning of the transient. Significant discrepancies among analyzed models exist starting from the first second up to the fourteenth second of the simulation. This is the stage when air enters the lower plenum and undergoes rebound and recirculation. It is clearly seen at Figure 33 and Figure 34 that K-Omega models as well as Standard K-Epsilon model highly over predict mixing associated with dissipation. Before air enters the lower plenum, results from all considered cases presents comparable trends. Based on Figure 35, each turbulence model perform in a similar manner and only Wilcox K-Omega reflects some stagnation stage from 0.3 sec to 3 sec from the beginning of the transient. On the other hand, laminar case shows very conservative results, limiting air movement to the core (thus rebound stage) to insignificant values. The Realizable K-Epsilon model presents realistic results, showing reasonable air concentration in the system and accounting for the mixing and recirculation in the lower plenum. From the analyzed models, only Realizable K-Epsilon is specifically intended for low-Reynolds type flows and this also explains why it compares well to the conservative laminar case. Another factor that was analyzed under the parametric turbulence study, was the velocity magnitude at the break cross section at the beginning of the accident. In all models, despite Realizable K-Epsilon, high velocity oscillations occur at the beginning of the onset of the exchange flow (Figure 35).

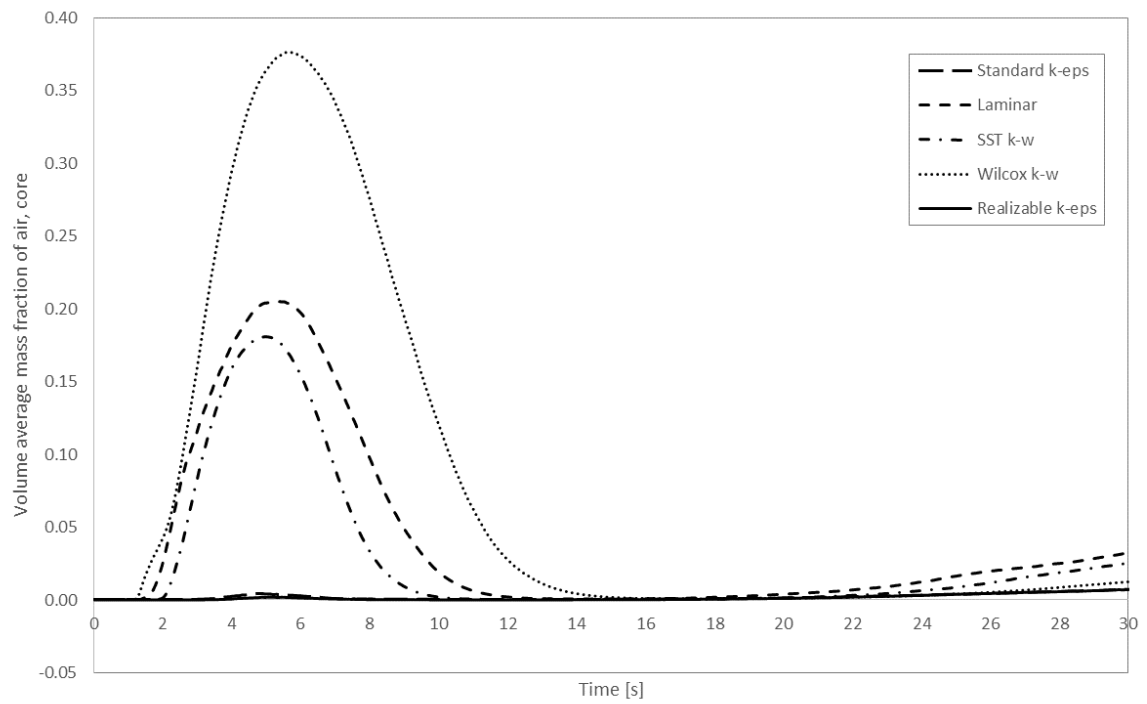


Figure 33 Volume average mass fraction of air in the core, turbulence models comparison.

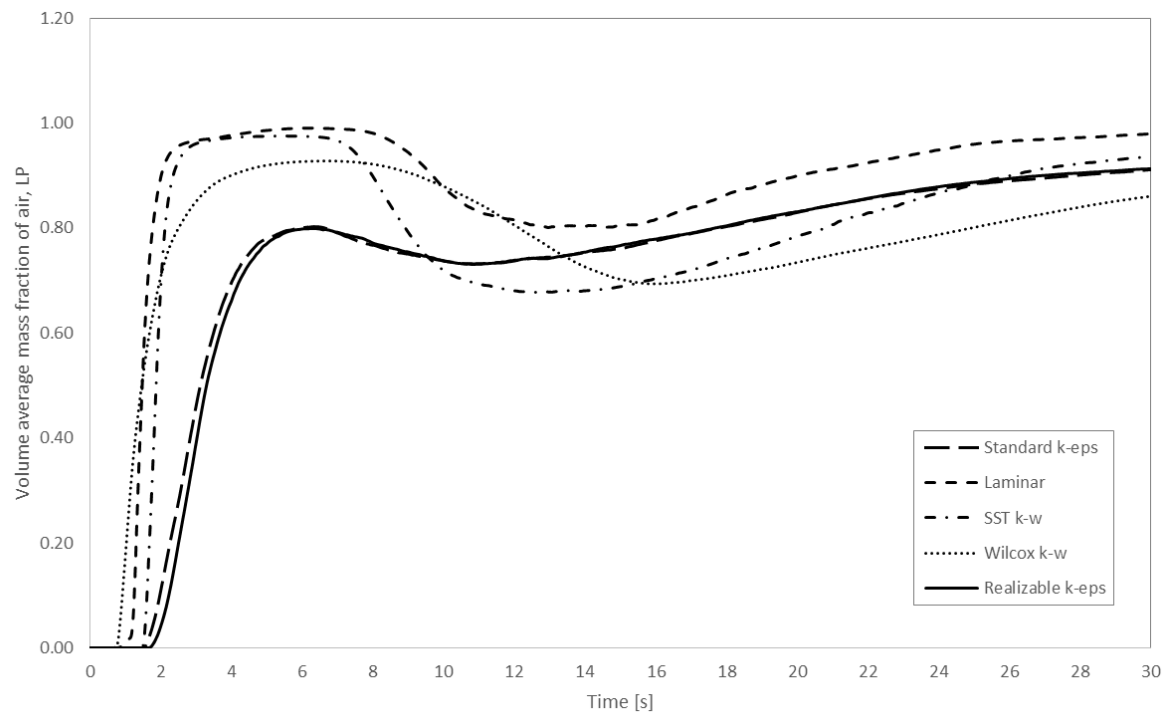


Figure 34 Volume average mass fraction of air in the LP, turbulence models comparison.

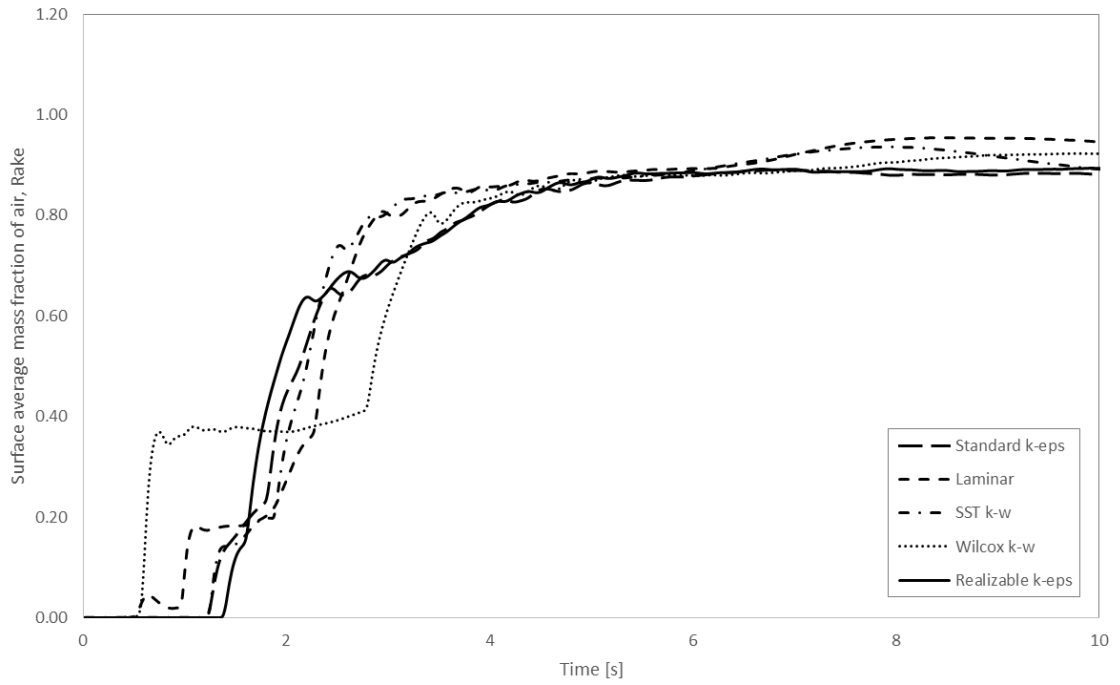


Figure 35 Surface average mass fraction of air at Rake cross section, turbulence models comparison.

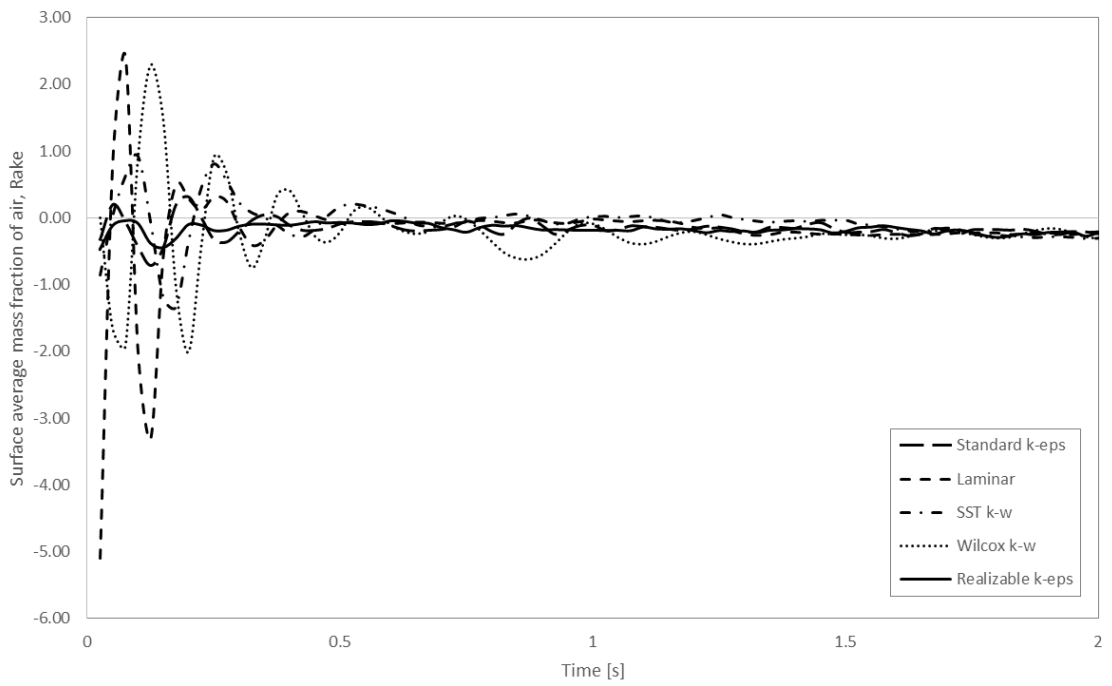


Figure 36 Surface average mass fraction of air at break cross section, turbulence models comparison

Additionally, X-Y velocity profiles can also be collected at the rake cross-section, providing insight into the distribution of the velocity and shapes the gravity currents. Below graphs (Figure 37-41) plots the x-velocity profile in the z-direction at the broken hot and cold ducts (vertical axis: the position along the ducts). The positive (+) velocity represents the flow in the lower plenum direction (air) and the negative velocity (-) represents the outward flow of helium to the cavity side. Standard K-Epsilon model shows the closest range of velocities to the laminar case. Laminar model predicts slightly higher air ingress speed, equal to 0.57 m/s (in other models this value ranges from 0.45 up to 0.54 m/s). The reason for that are the reduced mixing effects in the laminar case that influences in turn the temperature and density gradients of the flow that are the main driving forces for the stratified flow. Generally, magnitudes of the maximum flow velocities are in the same range and qualitatively, profile's shape reflects similar parabolic shapes. After investigation of the countercurrent flow velocities, Reynolds number and flow regime can be determined:

$$Re = \frac{UL}{\vartheta} \quad (66)$$

where: U is a scale of variation of velocity in a length scale L and ϑ is the kinematic viscosity (momentum diffusivity). In case of the countercurrent flow, a modified Reynolds number can be applied:

$$Re = \frac{U_{avg}H}{\vartheta} \quad (67)$$

where U_{avg} represents average fluid velocity and H states for the current height. As it was mention before, in each model, velocity profiles for hot and cold currents in both coolant legs, resemble the shape of fully developed flow in a simple pipe flow. Considering the 1-D flow in the fully developed flow in the circular pipe,

average velocity is defined as half of maximum velocity [96]. With assumption of fully developed laminar flow, current height equal to half channel diameter, Reynolds number is equal to:

$$Re_{hot\ current} (T = 960\ K) = \frac{0.57 \frac{m}{s} \cdot 0.15m}{8.533 \cdot 10^{-4} \frac{m^2}{s}} = 100.2 \quad (68)$$

Above value stays within the laminar regime. On the other hand considering mixing effects and further behavior of the fluid in the lower plenum it is optional to consider this flow as a low-Reynolds number turbulent flow. If in turn consider countercurrent flow as turbulent one, standard K-Epsilon and K-Omega as well as SST K-Omega models resemble no applicability to this type of flow phenomena. Conclusively, laminar model and Realizable K-Epsilon model imply the best solution, with laminar case being the most conservative one. Ultimately, in order to capture all flow phenomena and scales inside the lower plenum and also to account for the mixing and turbulence that will surely occur in the lower plenum during application of the mitigation concept, Realizable K-Epsilon model was selected for further modeling. Although K-Epsilon turbulence model may not be the most recommended model in theory, for the thermal stratification cases, it results in reasonable computational time and shows stable simulation convergence.

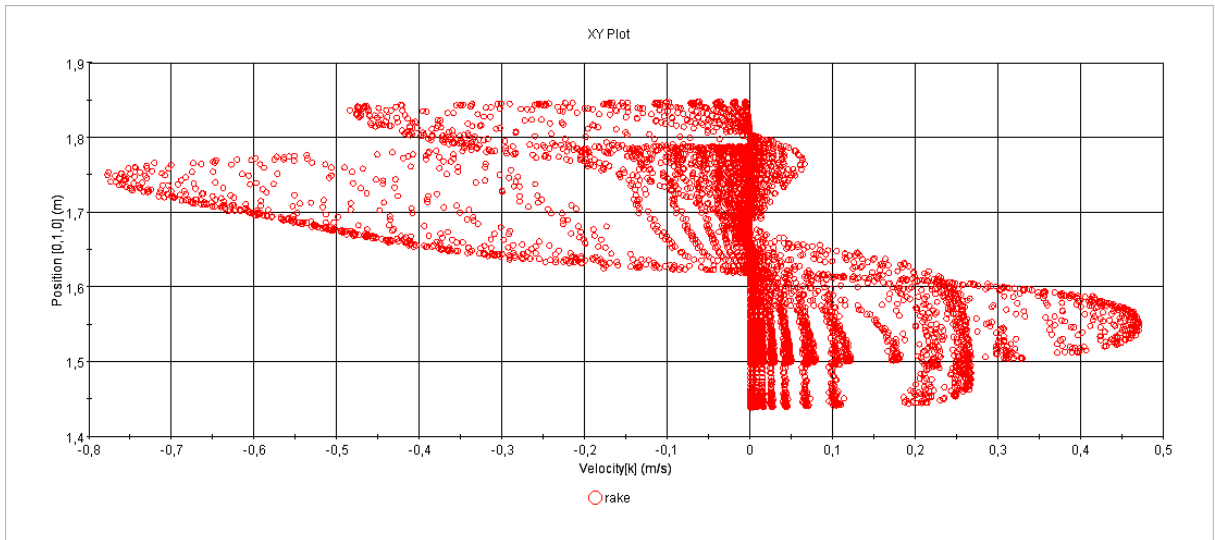


Figure 37 X-Y velocity profile at Rake cross section, Standard K-Epsilon model.

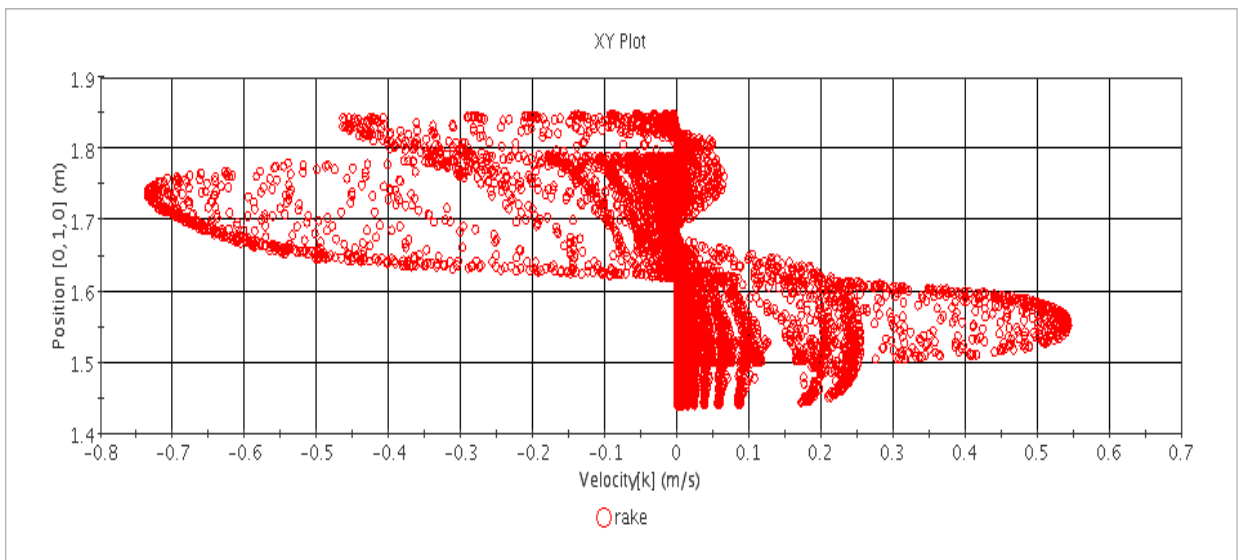


Figure 38 X-Y velocity profile at Rake cross section, Laminar model.

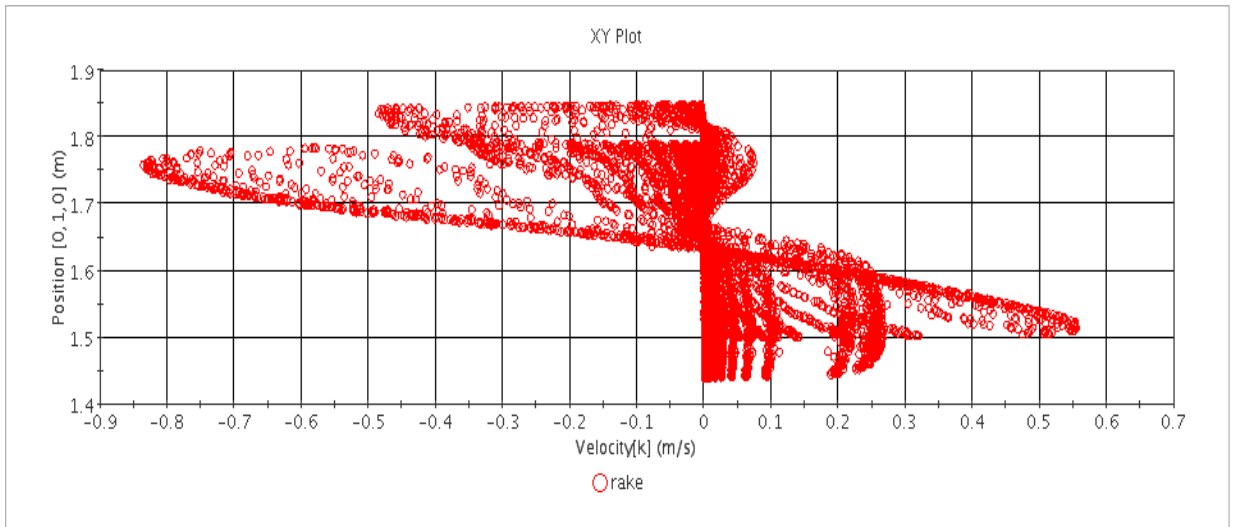


Figure 39 X-Y velocity profile at Rake cross section, SST K-Omega model.

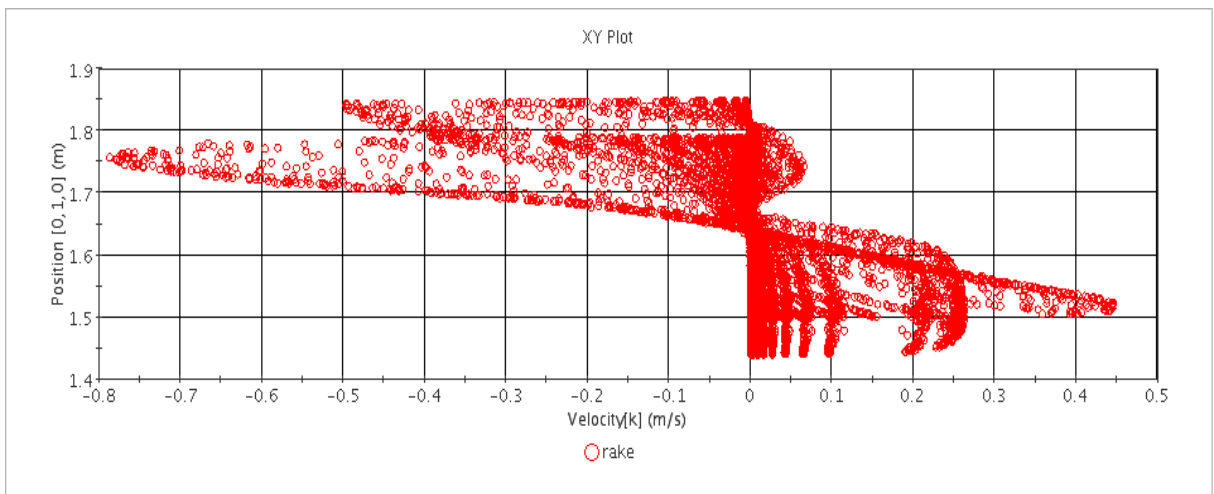


Figure 40 X-Y velocity profile at Rake cross section, Wilcox K-Omega model.

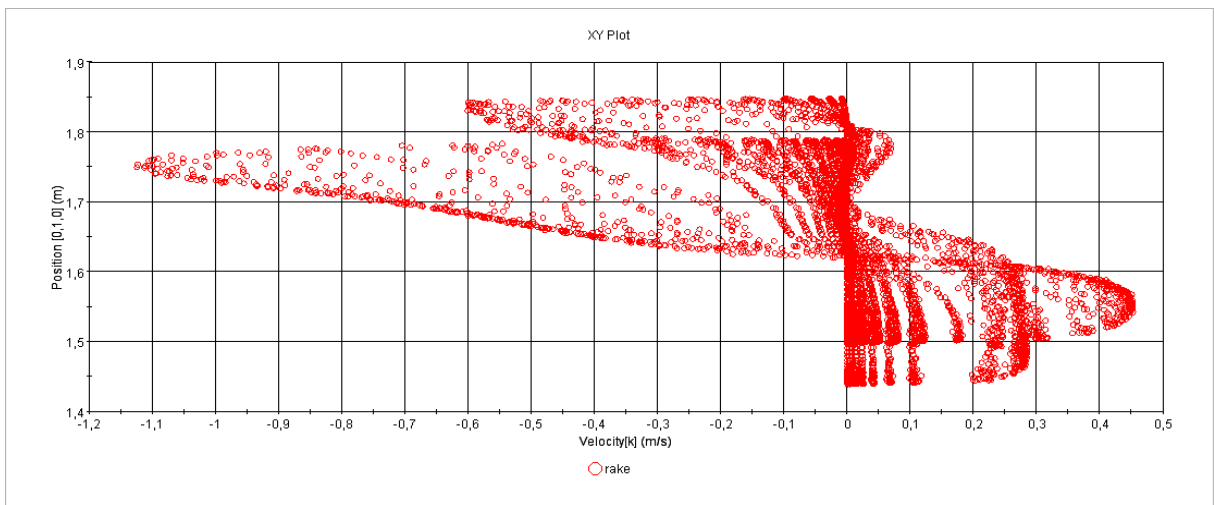


Figure 41 X-Y velocity profile at Rake cross section, Realizable K-Epsilon model.

6. CFD simulations results

6.1. Depressurization

The composition of the gas that ingresses into the reactor core during D-LOFC event is of high importance, because it will determine the oxygen concentration and the potential for graphite oxidation. The importance of the blowdown phase simulation lays in the fact that it supposes to provide initial conditions for the subsequent stratified flow stage, for instance: air mass fraction in the cavity or system temperature distribution. Besides that, there is a chance that reverse rarefaction Taylor wave will occur and lead to early ingress of some portions of air into the lower lenum and core during first seconds of the accident [47]. In the work done by Martineau et al. (2009), the finite element method spatial discretization of the Pressure-Corrected Implicit Continuous-fluid eulerian (PCICE) algorithm was developed to solve the classic Riemann shock tube problem with downstream boundary open to ambient pressure and upstream boundary pressure equal to 1.013 MPa (10 atm) and isothermal conditions (288.15 K). The Riemann shock tube simulation was implemented to illustrate the Taylor expansion wave and resulting rapid flow reversal. In this study, results from the depressurization simulation in the HTTF are comparable with the outcome from PCICE simulation provided by Martineau et al.

As it was mentioned in the Assumptions and Limitations section, STARCCM+ solver has troubles obtaining reasonable level of residuals convergence during the rapid depressurization of helium from the reactor core, vessel and lower plenum to the cavity. Simulation of these mechanism should be able to capture the dynamics of the flow at very short time scales. The best practice in such transient cases is to implement the coupled solver, significantly lower the solution time step

and reduce pressure and velocity underrelaxation factors [8]. Therefore, sensitivity studies on the mesh refinement and turbulence modeling were not executed in this simulation. Applied mesh size was the same as it was for the exchange flow analysis and turbulence model used was the Standard K-Epsilon.

To illustrate how pressure and velocity profiles changes in the system along the centerline line probe (Figure 42), several plots were drawn at various times of the transient. Figure 43 shows the initial conditions for pressure, temperature and domain placement in this problem (rupture placement, cavity, inner duct and lower plenum). When duct rupture occurs, discontinuity among the two initial states takes place.

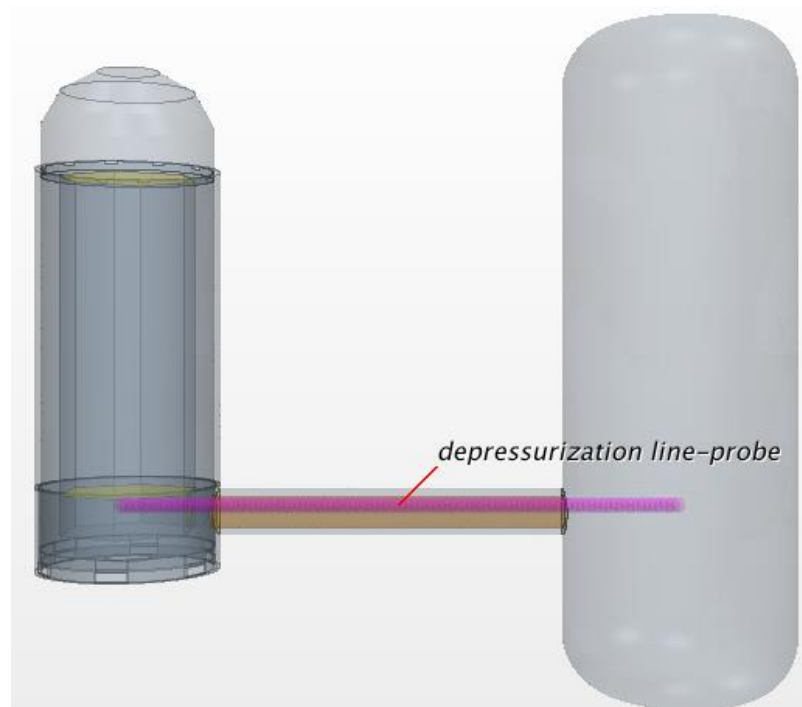


Figure 42 Placement of the depressurization line-probe (centerline).

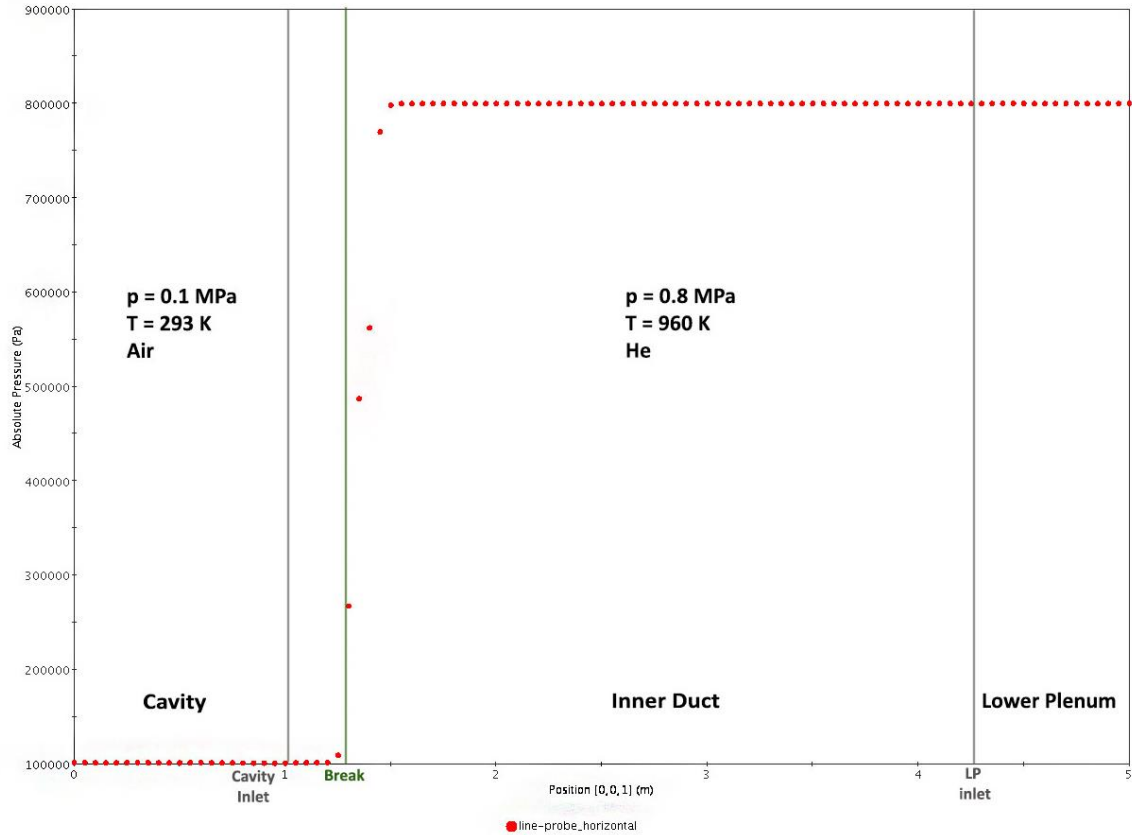


Figure 43 Depressurization pressure solution, $t = 0.7$ msec.

At the time of around 385 msec, classic Riemann solution is observed [70]. Shock wave propagates in the cavity direction, compresses the gas in the direction of wave formation and causes a pressure jump in front of the shock (Figure 44). Simultaneously, expansion wave propagates in the opposite direction (to the lower plenum) until it will reflect from the lower plenum side wall. One can observe the continuous form of the rarefaction wave: it consists of characteristic head and tail [4]. Expansion wave is also called as rarefaction wave because the gas in the high pressure section is being rarefied: helium density changes are shown in Figure 46, and can be compared with initial state density equal to 0.385 kg/m^3 . One should also notice how the initially static field is disturbed at very short time scale from the beginning of the break. Velocity distribution along the centerline at 385 msec, depicts maximum value at the shock wave front, equal to 700 m/s (Figure 45).

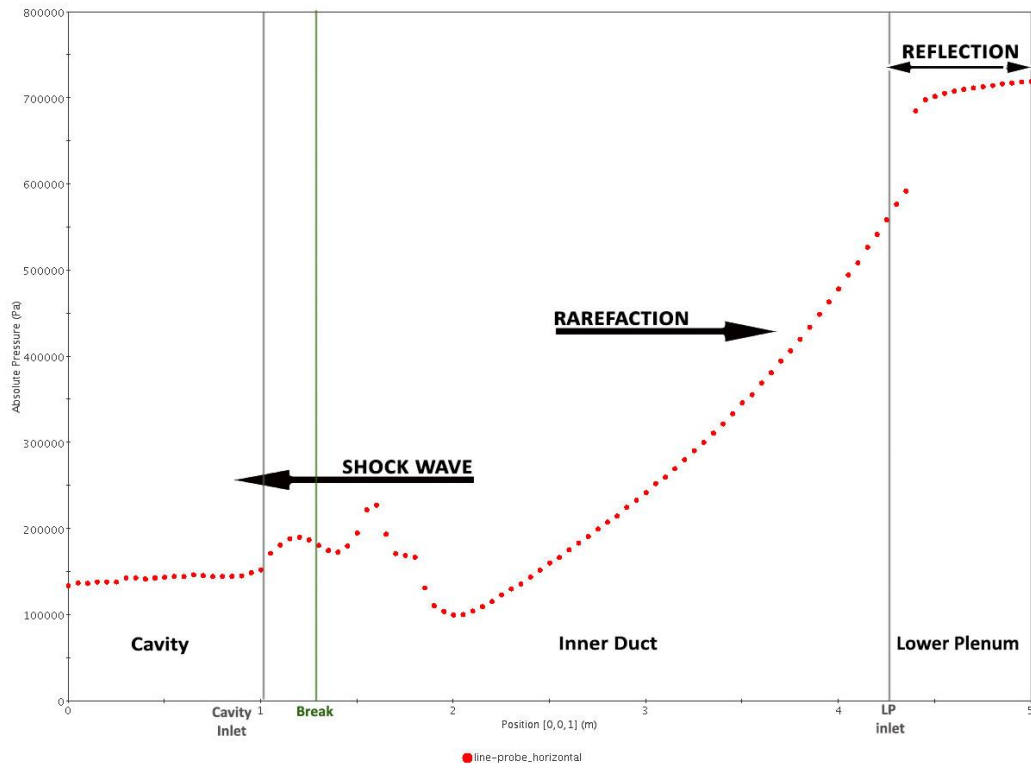


Figure 44 Depressurization pressure solution, $t = 385$ msec.

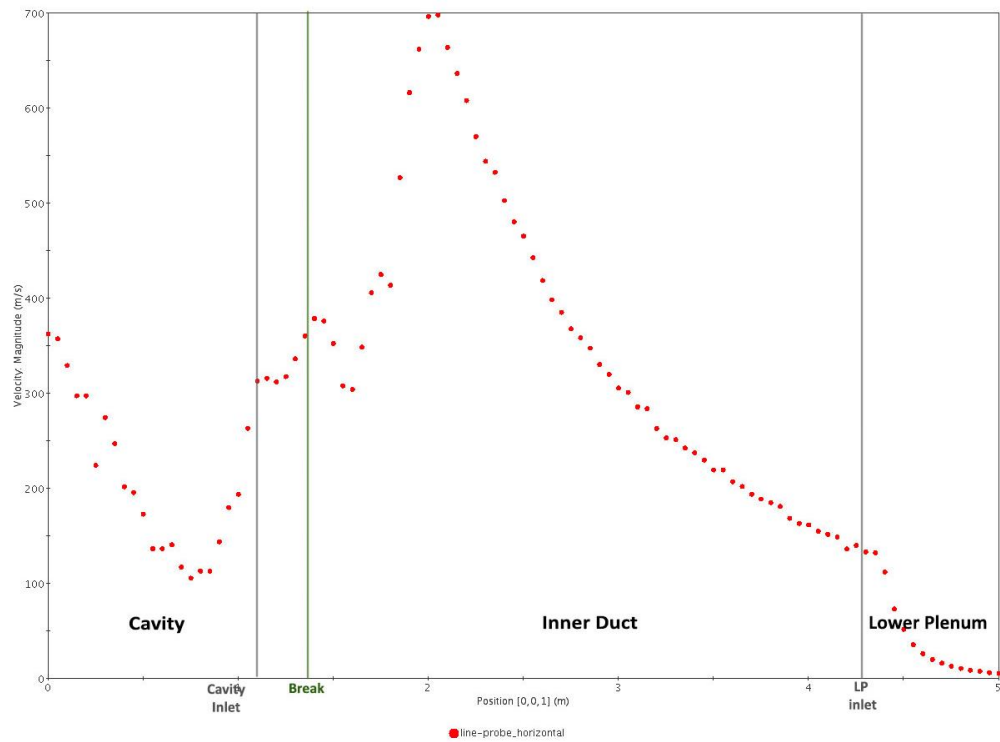


Figure 45 Depressurization velocity solution, $t = 385$ msec.

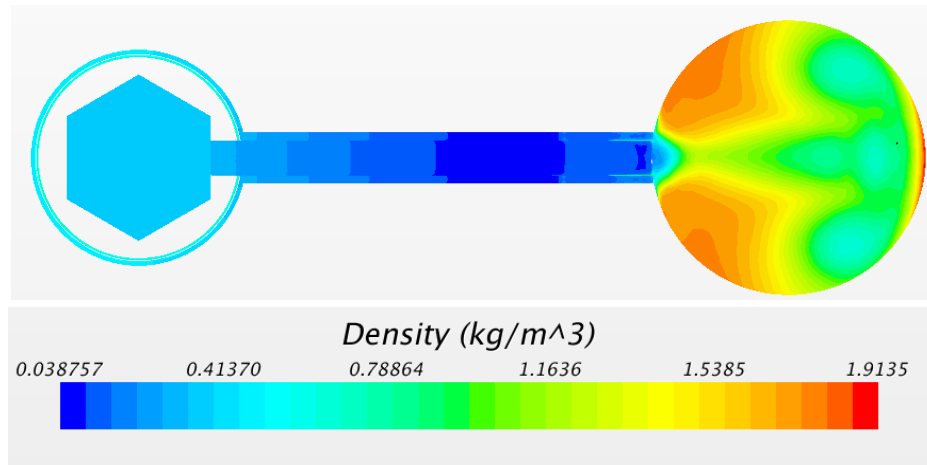


Figure 46 Density distribution during depressurization phase, at t=385 msec.

When the primary shock wave reaches the cavity wall, it gets reflected back into the cross duct (Figure 47, Figure 48). Higher temperature is observed behind the reflected shock (Figure 49). Almost simultaneously, the refraction wave from the initial shock reflects off the lower plenum side wall (Taylor wave).

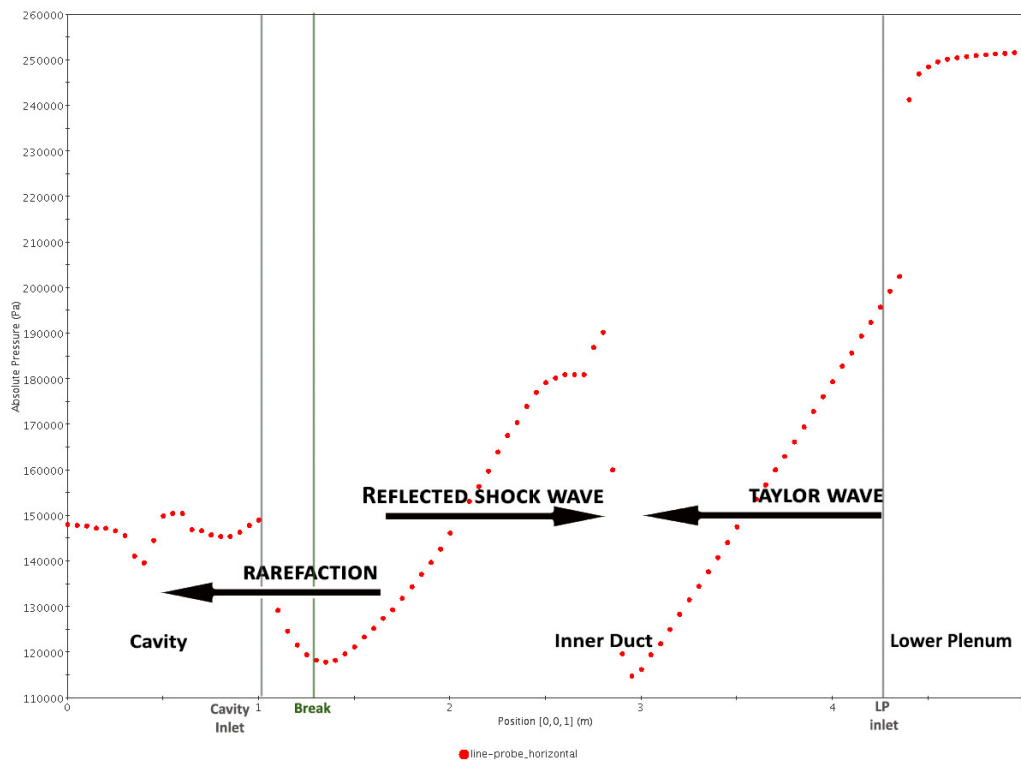


Figure 47 Depressurization pressure solution, t = 694 msec.

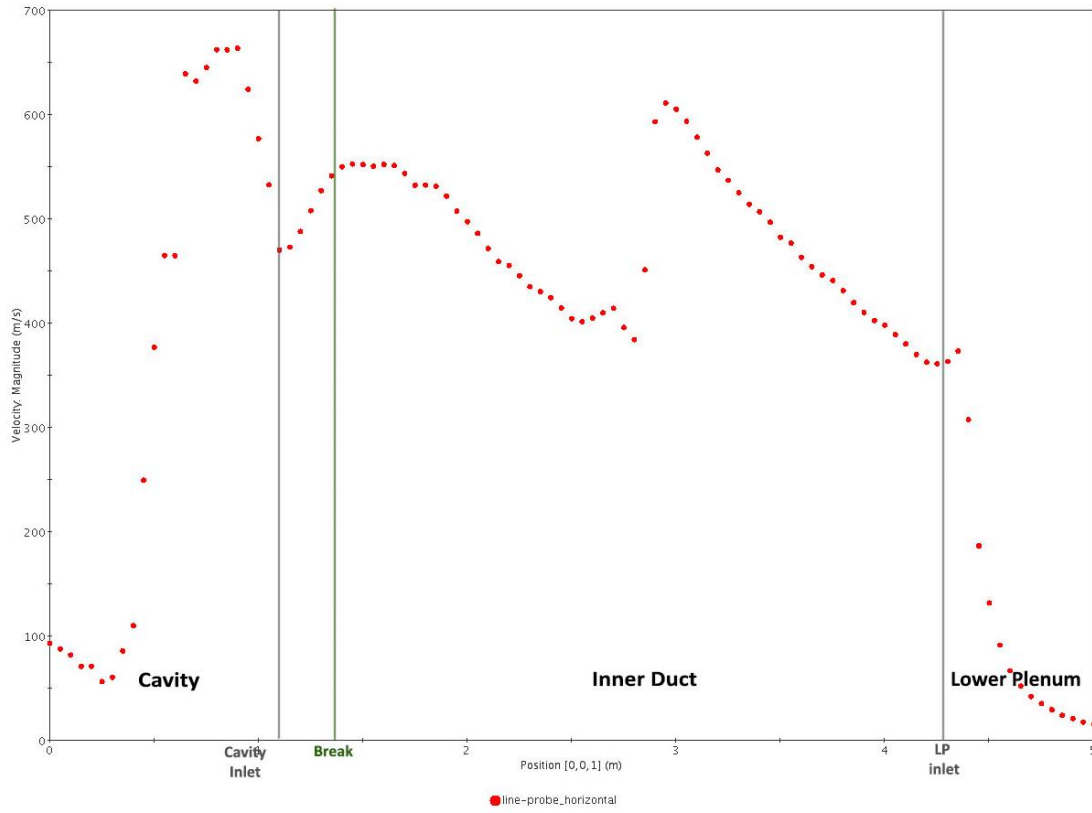


Figure 48 Depressurization velocity solution, t = 694 msec.

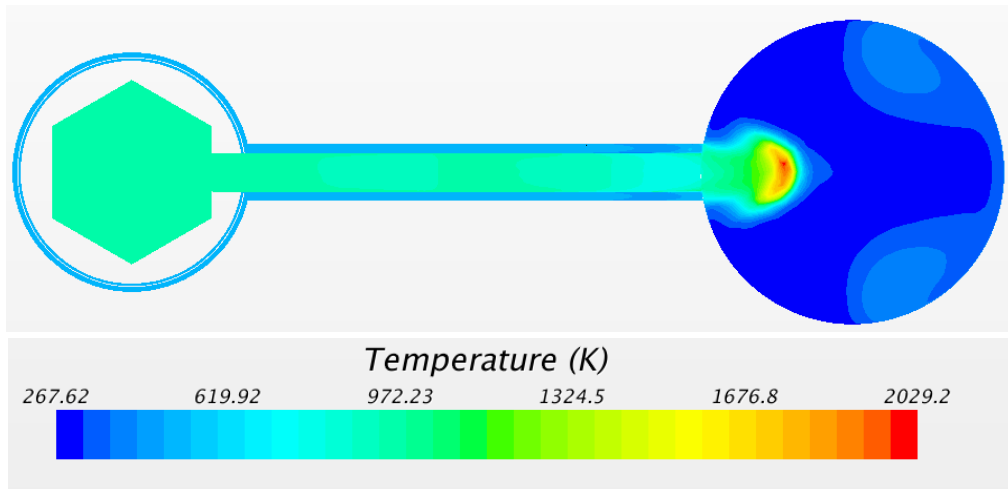


Figure 49 Temperature distribution during depressurization phase, at t=694 msec.

By the solution time of $t=826$ msec, pressure behind the Taylor wave continues to drop as well as the pressure gradient due to rarefaction wave propagating in the cavity direction (Figure 50). Leading edges of the pressure waves overlaps in the center of the cross duct. Maximum velocity is reduced to 600 m/s in the inner duct and is greatly reduced (less than 50 m/s) behind the rarefaction and Taylor waves (Figure 51). At this time of the solutions, the pressure field in the inner duct is below the atmospheric pressure and the cavity side becomes slightly overpressurized comparing to the lower plenum.

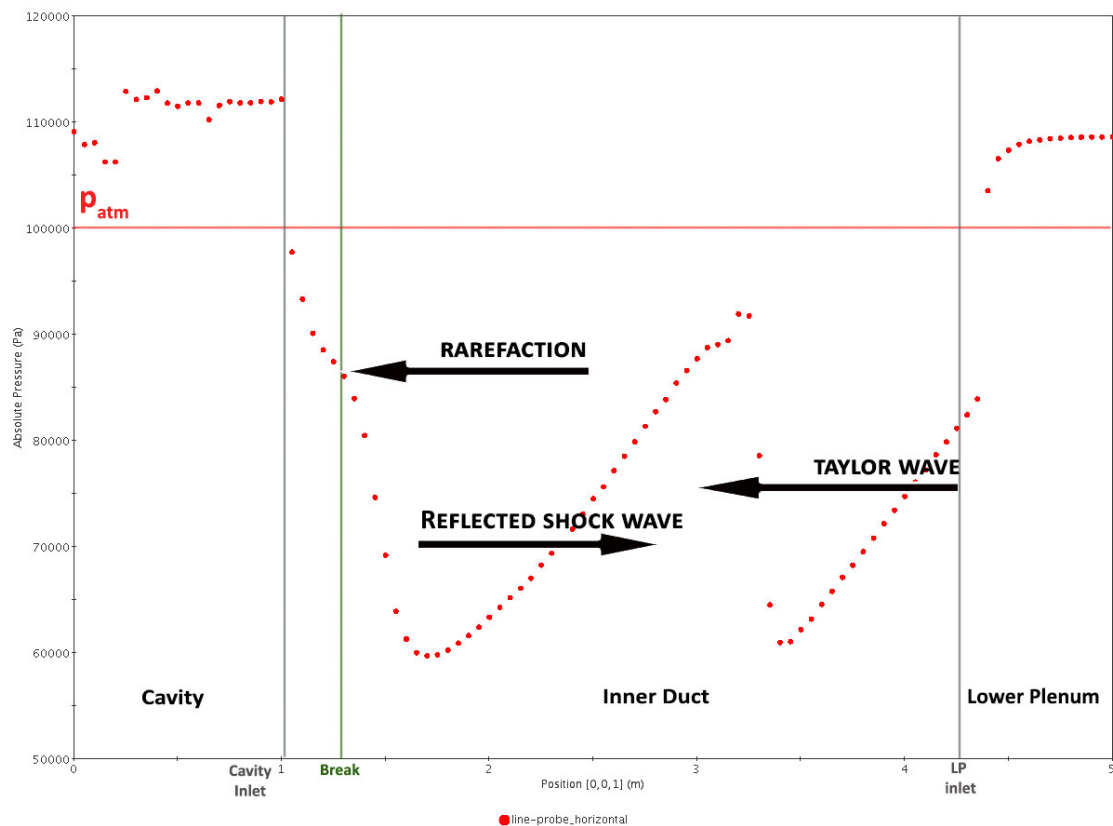


Figure 50 Depressurization pressure solution, $t = 826$ msec.

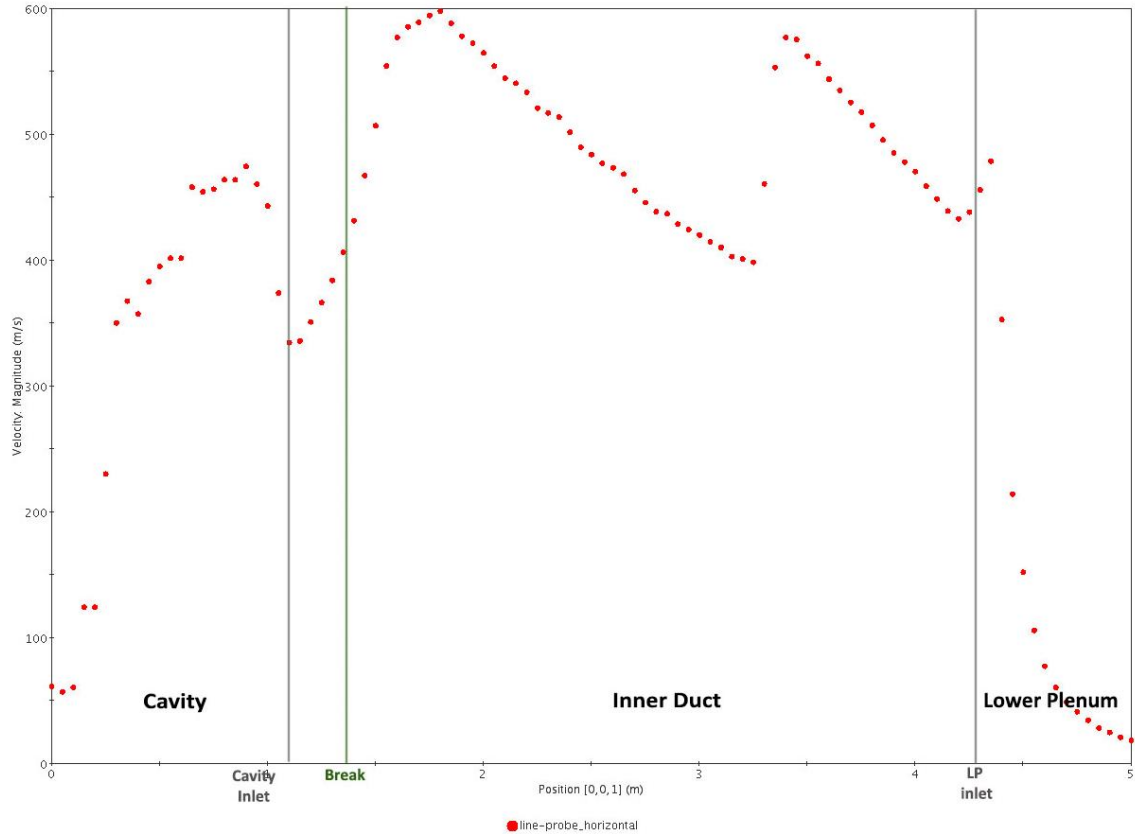


Figure 51 Depressurization velocity solution, $t = 826$ msec.

Pressure and velocity distributions at time $t=981$ msec are illustrated in Figure 52 and Figure 53. Flow reversal in the simulation is observed. Again pressure wave travels from the cavity side into the inner duct. Peak velocity of 600 m/s is observed one more time at the reversed shock propagation front. Lower plenum and part of the inner duct are still below the atmospheric pressure value.

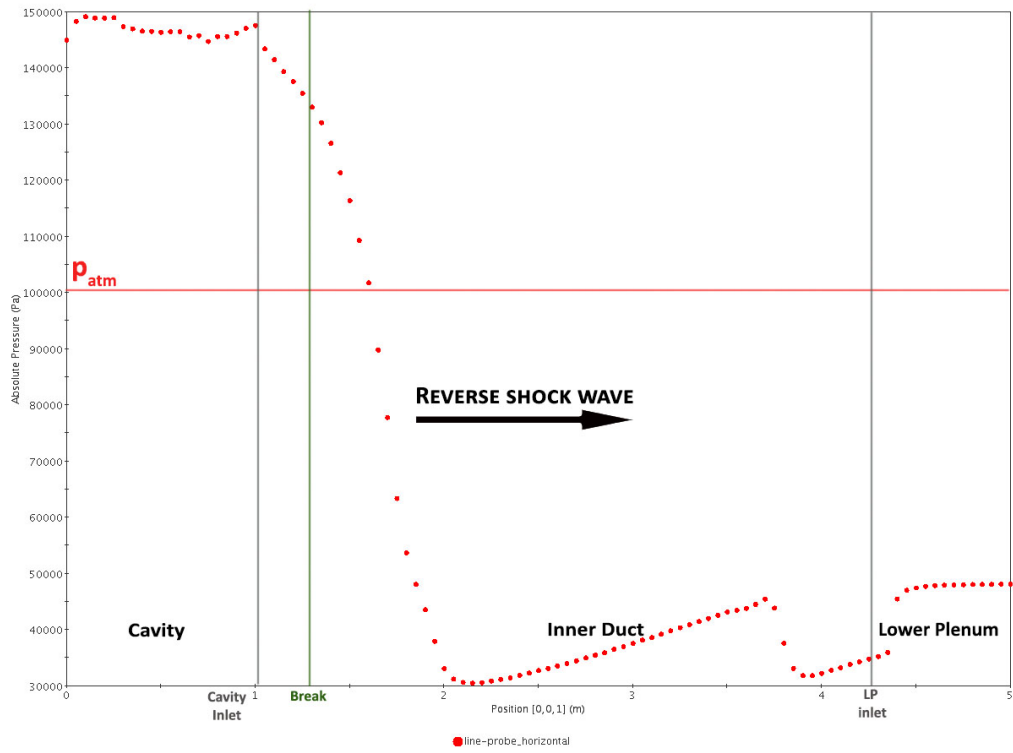


Figure 52 Depressurization pressure solution, t = 981 msec.

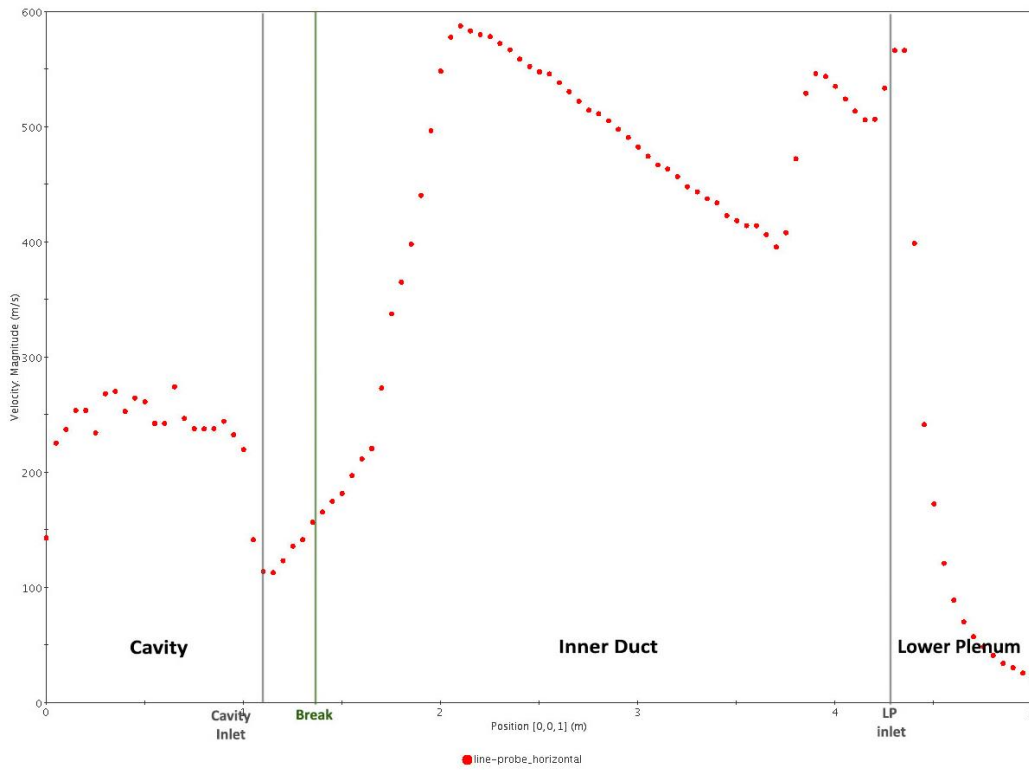


Figure 53 Depressurization velocity solution, t = 981 msec.

Volume average mass fraction of air at 981 msec from the beginning of the transient is slightly reduced in the cavity region, by 0.4% (Figure 54, Figure 55). The highest drop in the air mass fraction is seen near the domain inlet, where helium enters the cavity due to the previously propagated shock wave. At this point reverse shock wave moves reversely but the velocity field direction is still towards the cavity.

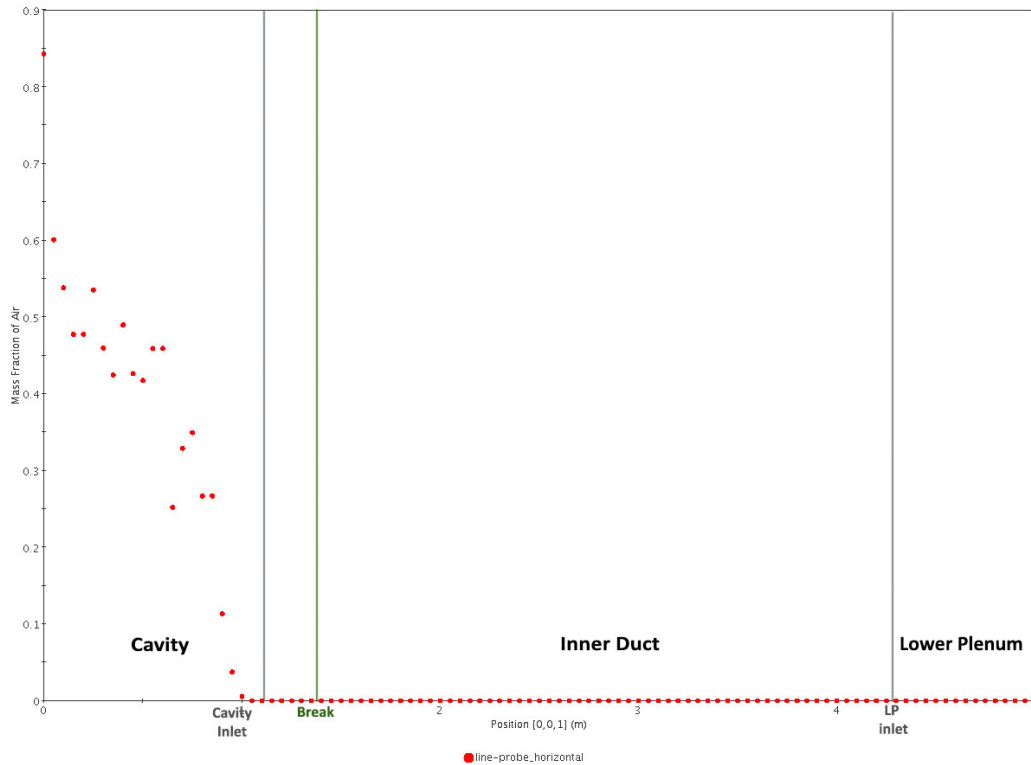


Figure 54 Depressurization air mass fraction solution, t=981 msec.

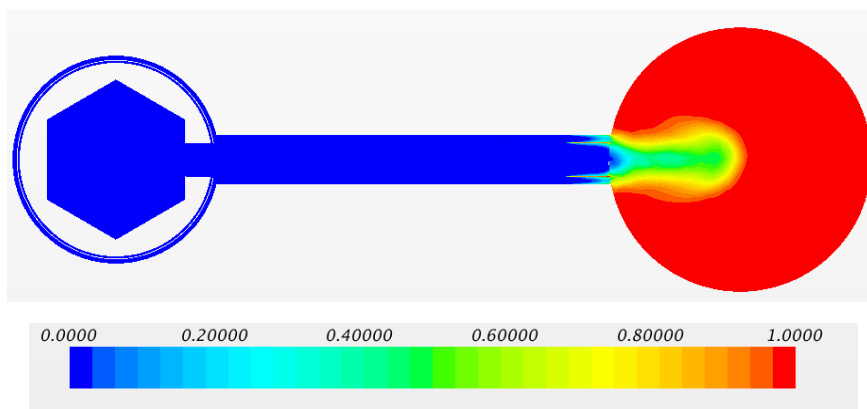


Figure 55 Air mass fraction distribution during depressurization phase, at t=981msec.

While the transient simulation proceeds, another reflected wave is created at the lower plenum side (Figure 56). Reverse wave from the other side that at the time of 1.58 sec occupies almost whole volume of the inner duct. It travels to the lower plenum and will be soon reflected from the lower plenum boundary as well. Maximum velocity is reduced to 400 m/s (Figure 57). At this moment velocity magnitude at break cross section is positive, which means that the direction of the flow velocity is from the cavity tank to the vessel. Helium that previously had entered the cavity volume, will now be removed and portion of air will travel to the reactor side instead (Figure 58).

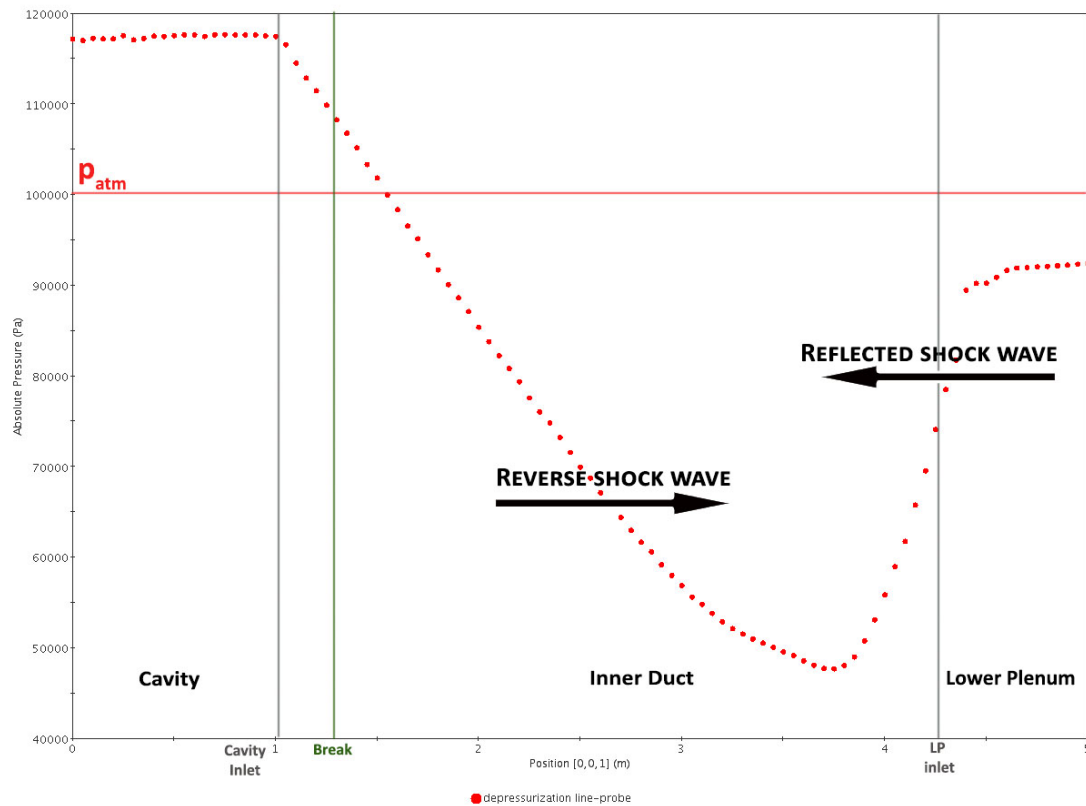


Figure 56 Depressurization pressure solution, $t = 1.58$ sec.

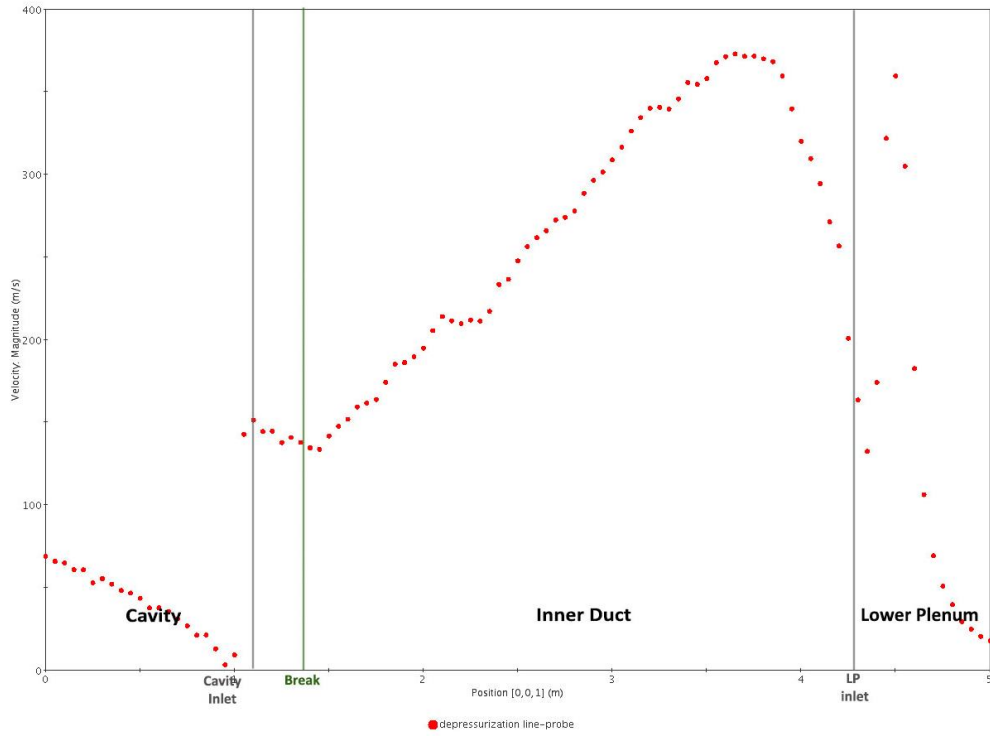


Figure 57 Depressurization velocity solution, t = 1.58 sec.

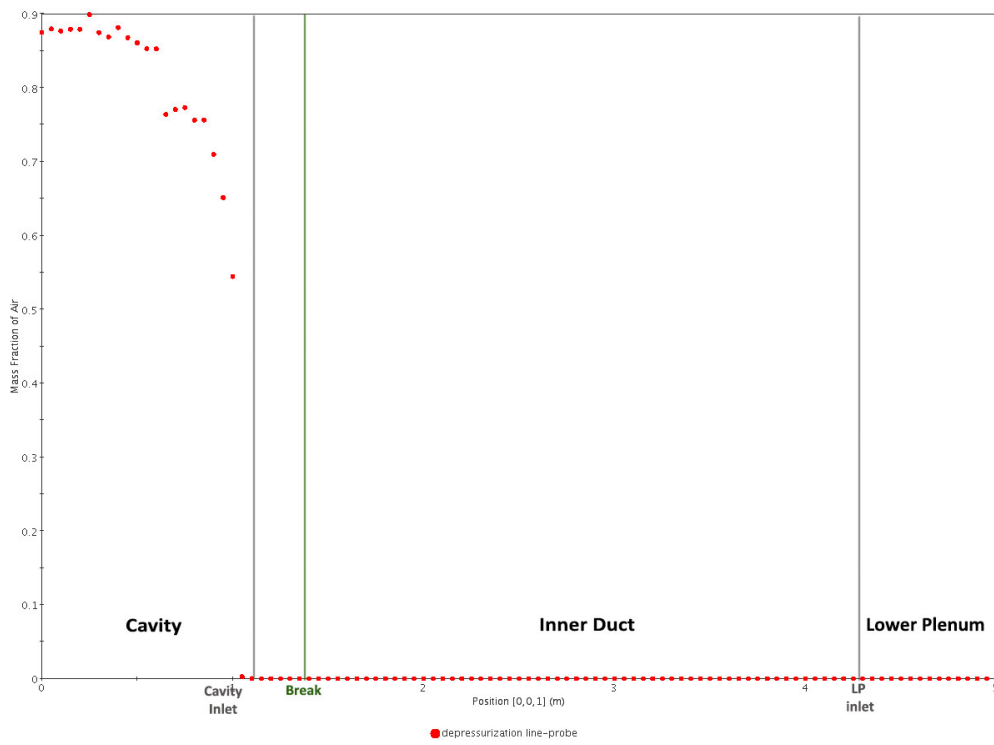


Figure 59 and Figure 60 show the progress of the simulation after the next 20 ms. At the simulation time of $t=1.785$ sec, the reverse flow shock has reached the lower plenum solid wall and yet another reflected shock is formed against the direction of the flow velocity.

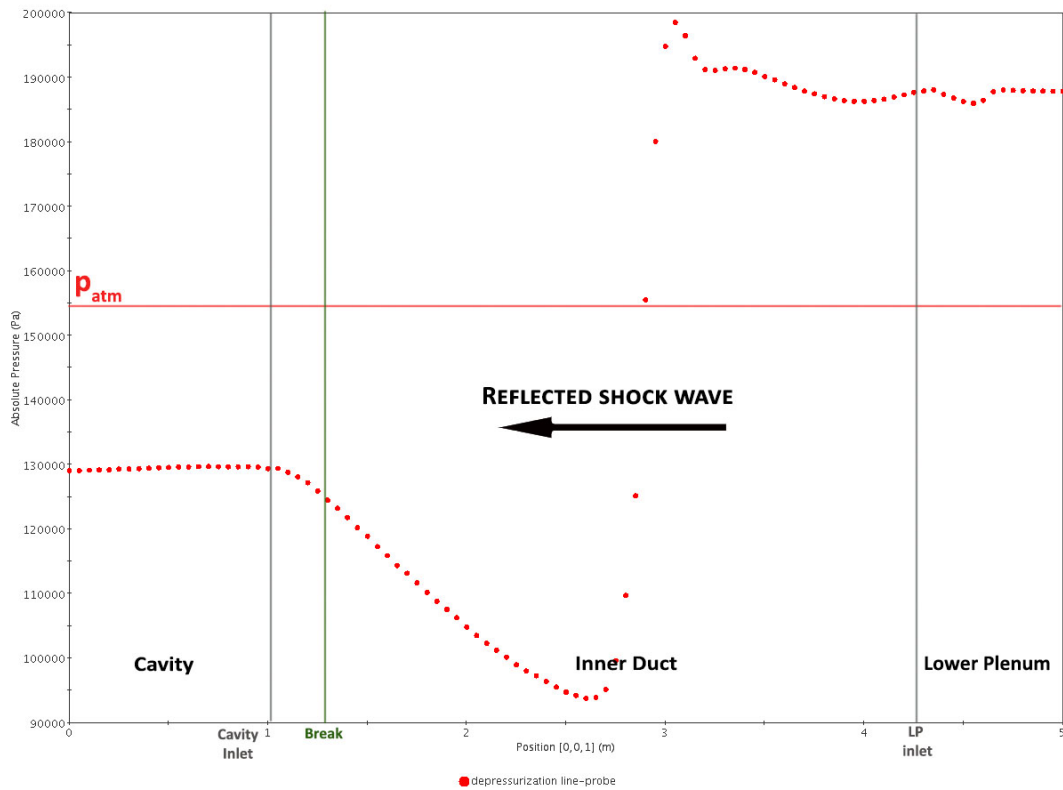


Figure 59 Depressurization pressure solution, $t = 1.78$ sec.

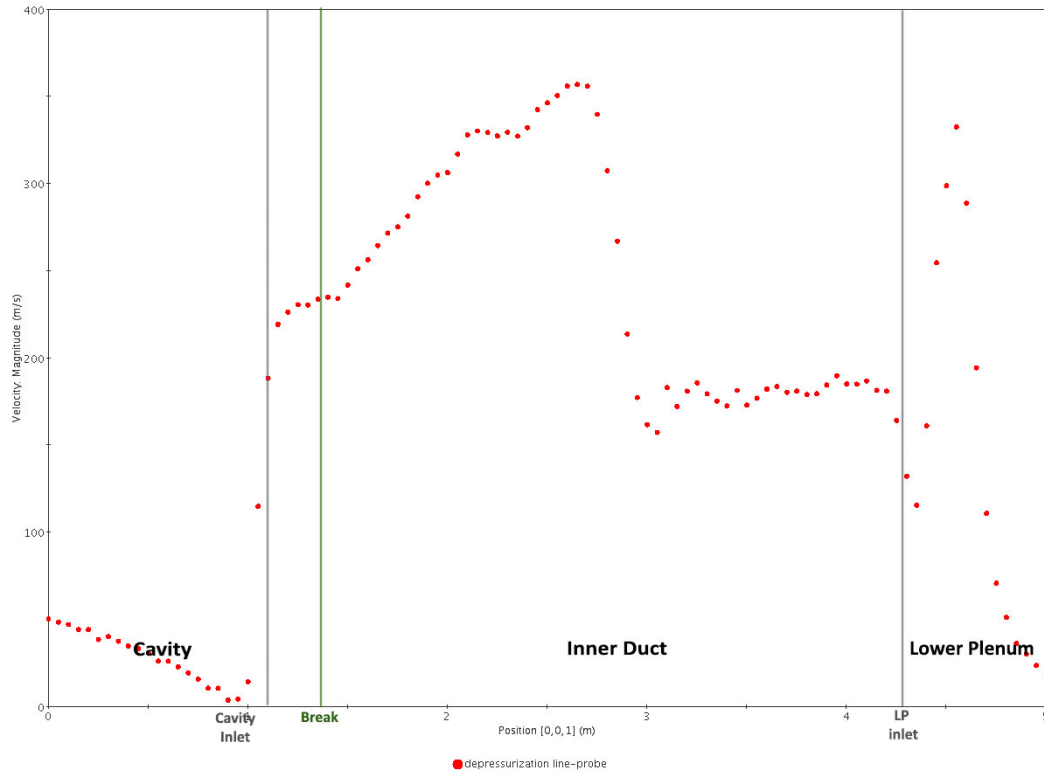


Figure 60 Depressurization velocity solution, $t = 1.78$ sec.

At the time scale of around 10 sec, pressure changes from 0.8 MPa to atmospheric value will occur. Flow reversals and rarefaction waves will be observed through out the entire process. Therefore in the curve showing average absolute pressure in the whole system as a function of transient time, pressure buildups and valleys are observed in the form of high amplitude oscillations (Figure 61). These oscillations decay as flow reversal momentum decreases along with system pressure decrease. Finally, pressure equalizes at the level of 115.3 kPa.

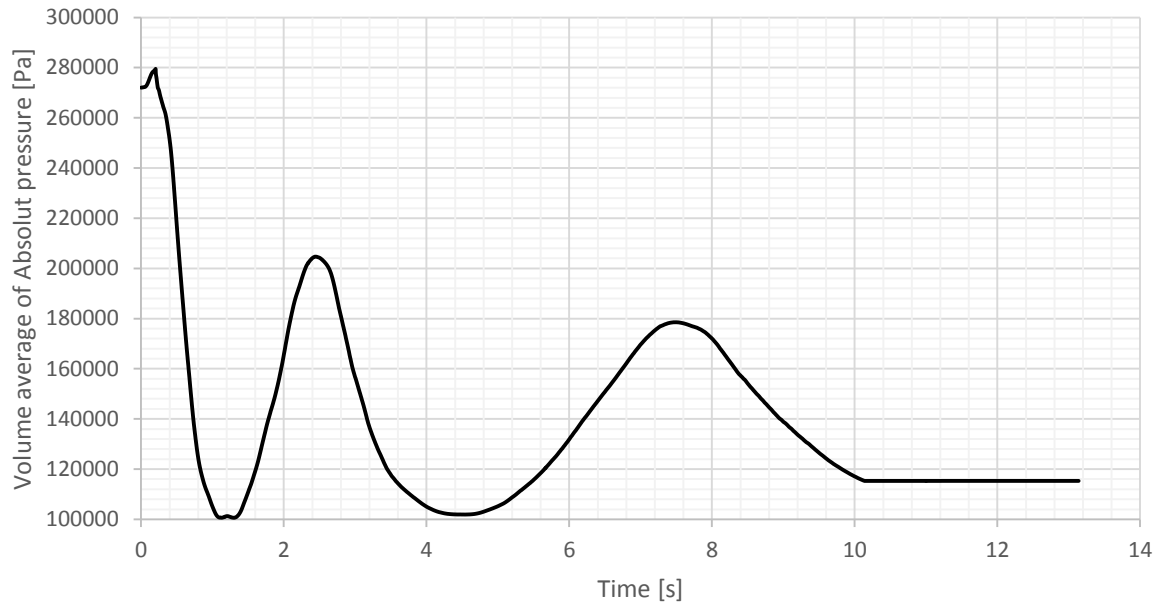


Figure 61 Volume average of absolute pressure in the entire reactor system during blowdown simulation.

To reach the pressure equalization stage after blowdown phase, the system must go through a variety of mass and energy states as the pressure decreases. The trajectory of these states is important because it is a driving force for the air and helium concentration gradients.

From the blowdown phase analysis it can be concluded that neither significant amount of helium enters the confinement volume nor air occupies lower plenum or core regions. This is why in the subsequent phase of the analysis, which is the stratified flow, systems parameters at the end of the blowdown simulation were not considered as initiating condition.

On the other hand, trajectory and development of shock waves in the reactor regions should be further analyzed in order to capture their influence on the construction and materials strength.

6.2. Lock exchange flow –porous bodies approach

3D CFD results of the air-helium exchange flow are discussed in this section. At the initialization of the simulation, both fluids are initially at rest. When orifice (break) is activated, a dense gravity current flows along the bottom to the Lower Plenum and a buoyant current will flow along the top to the cavity. Figure 62 shows the onset of the stratified flow, while air starts entering the inner/outer duct through the bottom part of the channel. Gravity current velocity magnitude distribution (with placement of the cross section planes) after 1.0 sec from the beginning of transient is shown in Figure 63. Gas velocity distribution at the hot and cold duct cross sections and corresponding density differences at 22 sec from the beginning of the simulation are shown in Figure 64. Clear stratification layer can be seen among air and helium at this simulation time. Velocity pattern at the instrumentation Rake section plane at this time, provides insight into velocity values of the gravity current.

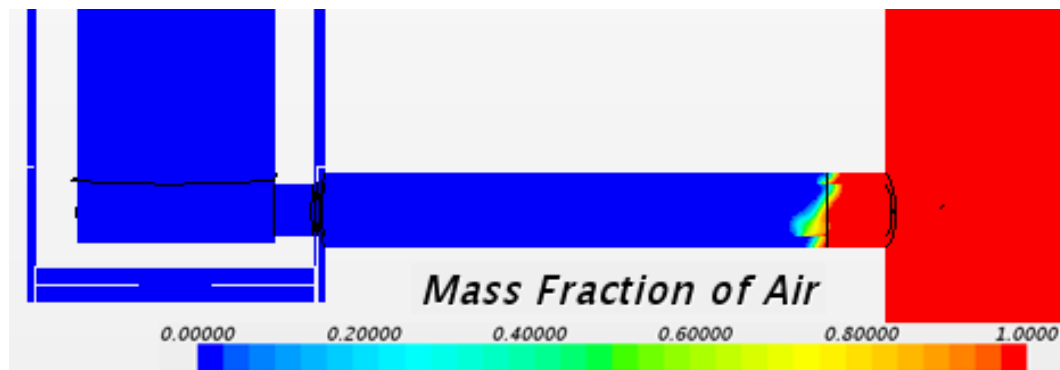


Figure 62 Onset of the exchange flow, air mass fraction.

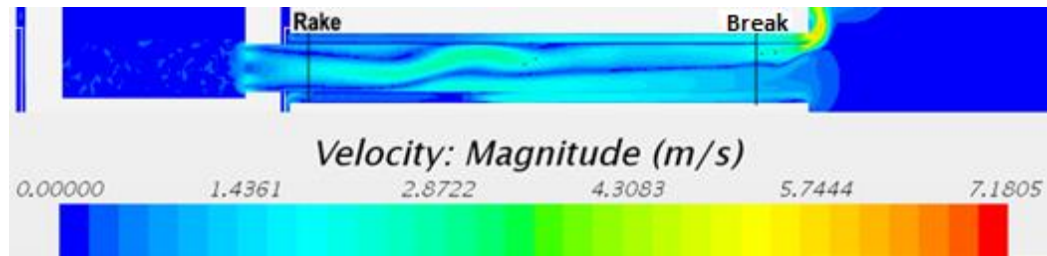


Figure 63 Stratified flow velocity magnitude distribution in the coaxial pipe at 1.0 s from the beginning of the transient.

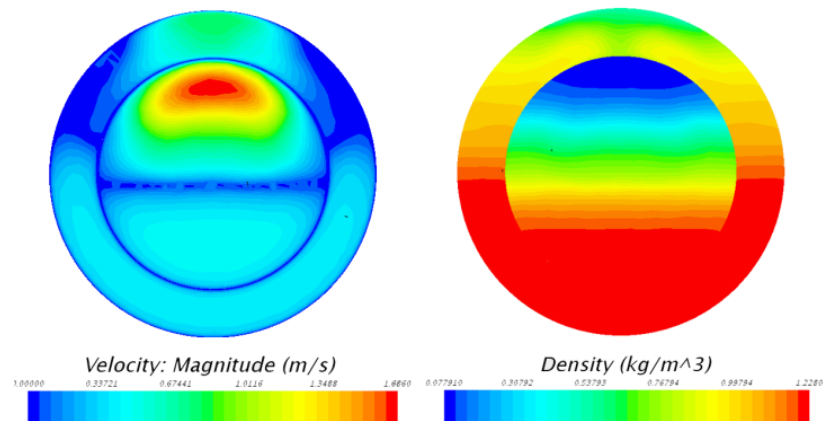


Figure 64 Velocity and density distributions at Rake section.

The figures below present flow streamlines at the end of the exchange flow simulation (30 sec) (part seed placed at the core/upper plenum interface). Helium that propagates from the core side does not recirculate or accumulate in the lower plenum volume. At this point of the simulation, lower plenum is filled with air (90% of its volume) and only small portion of helium travels to the cavity side occupying only utmost upper part of the inner duct and rest of it mixes with air in the upper lower plenum part. Lighter gas propagates to the bottom of the core ($v = -0.1 \text{ m/s}$) because in this area it has reduced temperature, being cooled by the inflowing air (thermal stratification). This process enhances air propagation to the lower reflector region.

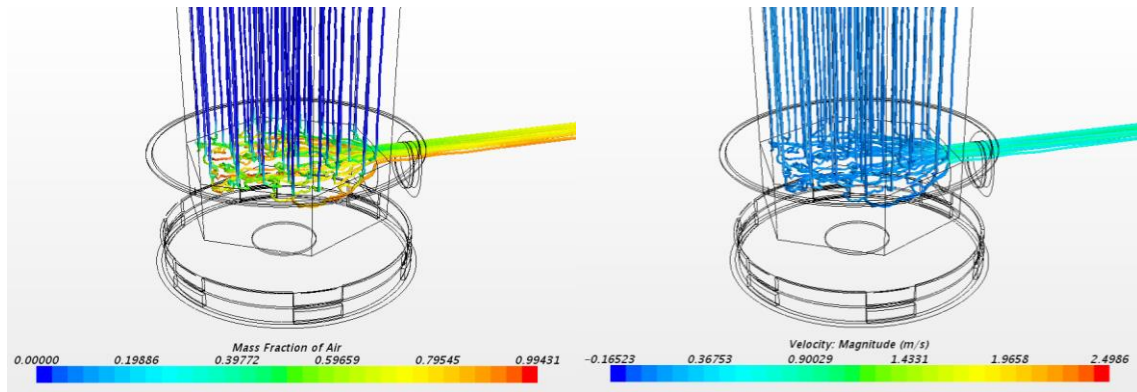


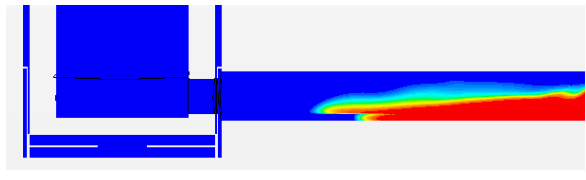
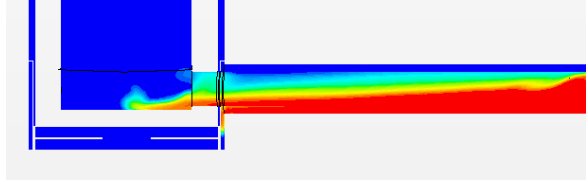
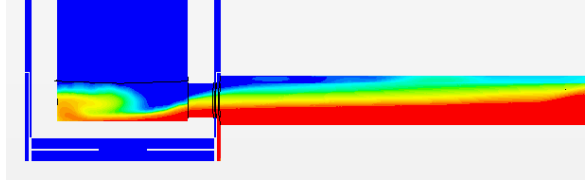
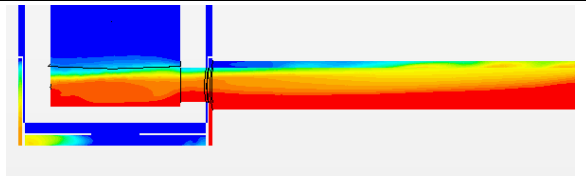
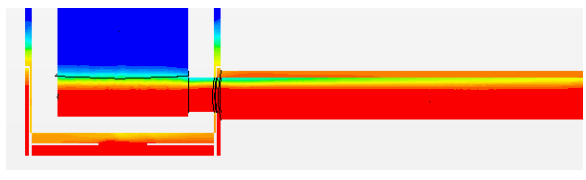
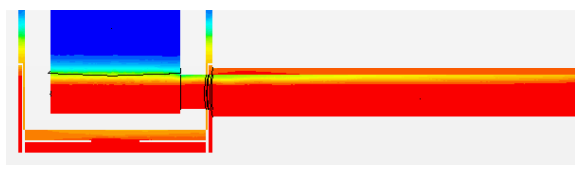
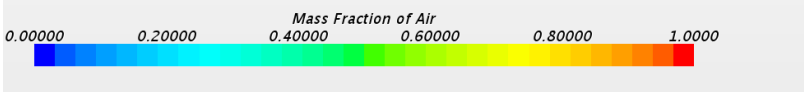
Figure 65 Exchange flow streamlines at the end of simulation, t=30 sec.

Table 11 depicts the sequence of exchange flow stages. At 1 sec from the beginning of the transient, cold gas nose propagates at the bottom of the cross duct. Air stream creates counter-current flow inside the channel and hot helium, being lighter than air, escapes from core and lower plenum structures towards the cavity along the top region of the duct. Heavy gas leading edge follows the shallow shape suggested by Keller & Chyou (1991) for the gas density difference below the critical value suggested by Lowe et al. (2005). As soon as after another second, cold air plume enters the bottom part of the lower plenum and creates a head wave that will propagate in the domain, rebounding from the lower plenum walls (starts at around 3 sec from the beginning of the transient and lasts for another 20 sec), producing wavy interface that subsequently promotes gas mixing. The more air enters the domain the mixing effect is reduced and quazi equilibrium phase is reached (>23 sec). This process will last until air amount in the lower plenum will reach the hot duct upper elevation level (>30 sec).

Heavy gas nose reaches the center of the lower plenum after around 2.5 seconds from the beginning of the transient. From Figure 66, it can be seen that the normalized current depth at that time is equal to 0.3 and current superficial velocity equals 1.35 m/s. If one would apply normalized current height with reference to data obtained for liquids (Lowe et al. 2005), then the same process

would take 22.3 sec and superficial velocity would reach 0.17 m/s. This way, it is proven that results for non-Boussinesq flow obtained by Lowe et al. (2005) for liquids, cannot be applied to gases gravity driven flow.

Table 11 Sequence of events in lock-exchange study – baseline model.

1 sec		Stratified flow in the inner duct and outer duct
2 sec		Dense air leading edge reaches lower plenum entrance and starts filling it up
3 sec		Air bounces off the opposite lower plenum wall, rebound and recirculation occurs.
5 sec		Due to recirculation, small amount of air enters the lower plenum reflector region
23sec		Air amount in the lower plenum slowly reaches the inner duct elevation level
30 sec		Air diffuses into reactor core, quasi equilibrium phase is reached
		

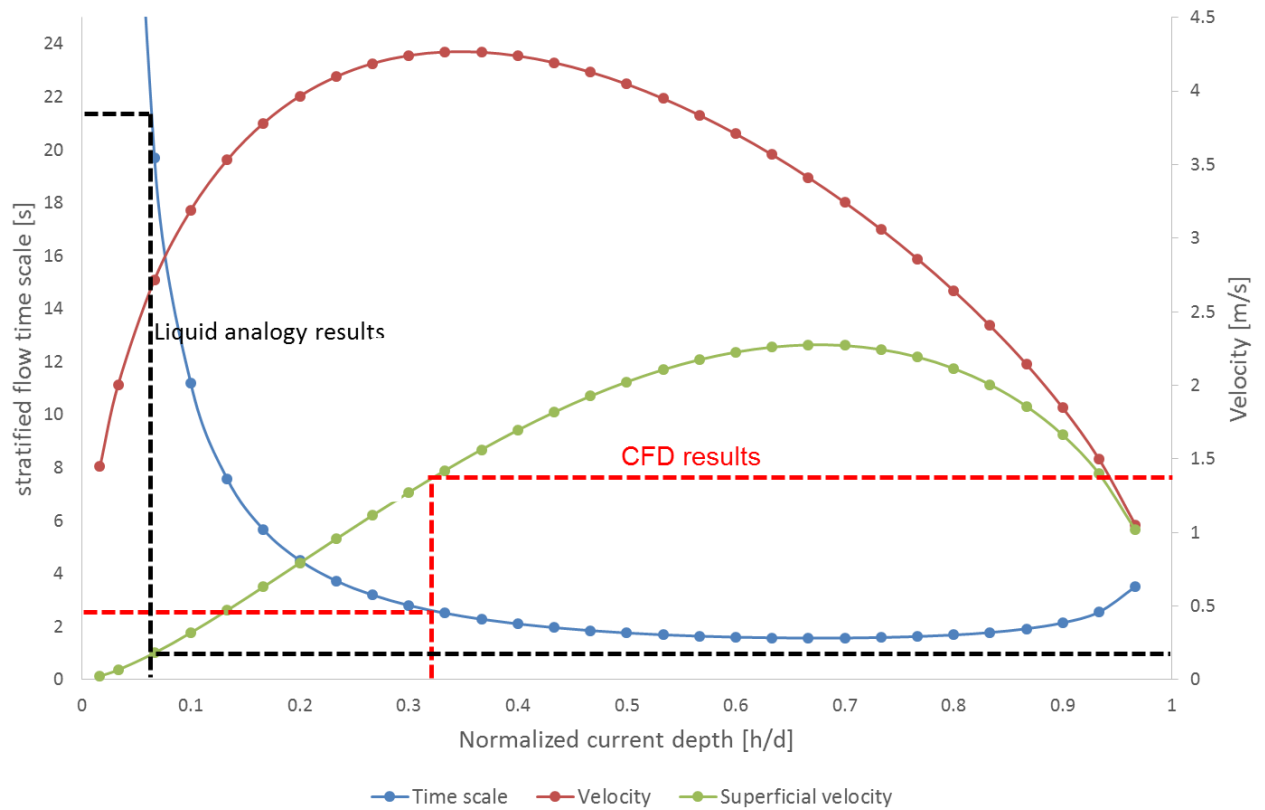


Figure 66 Stratified flow time scale as a function of the normalized current depth with reference to the stratified flow time scale obtained from CFD results, marked with the dashed line.

Figure 67 depicts calculated volume average air mass fractions in five different zones of the modeled system. Air concentration that was assumed to be 100% in the cavity at the beginning of the simulation, decreases very slightly in time. At the same time, air concentration rises quickly up to 97% in the cross duct and up to 90% in the lower plenum. Air amount in the vessel increases more slowly and after 30 sec reaches 15%. At the end of the simulation, volume average mass fraction of air in the core is only 0.7%.

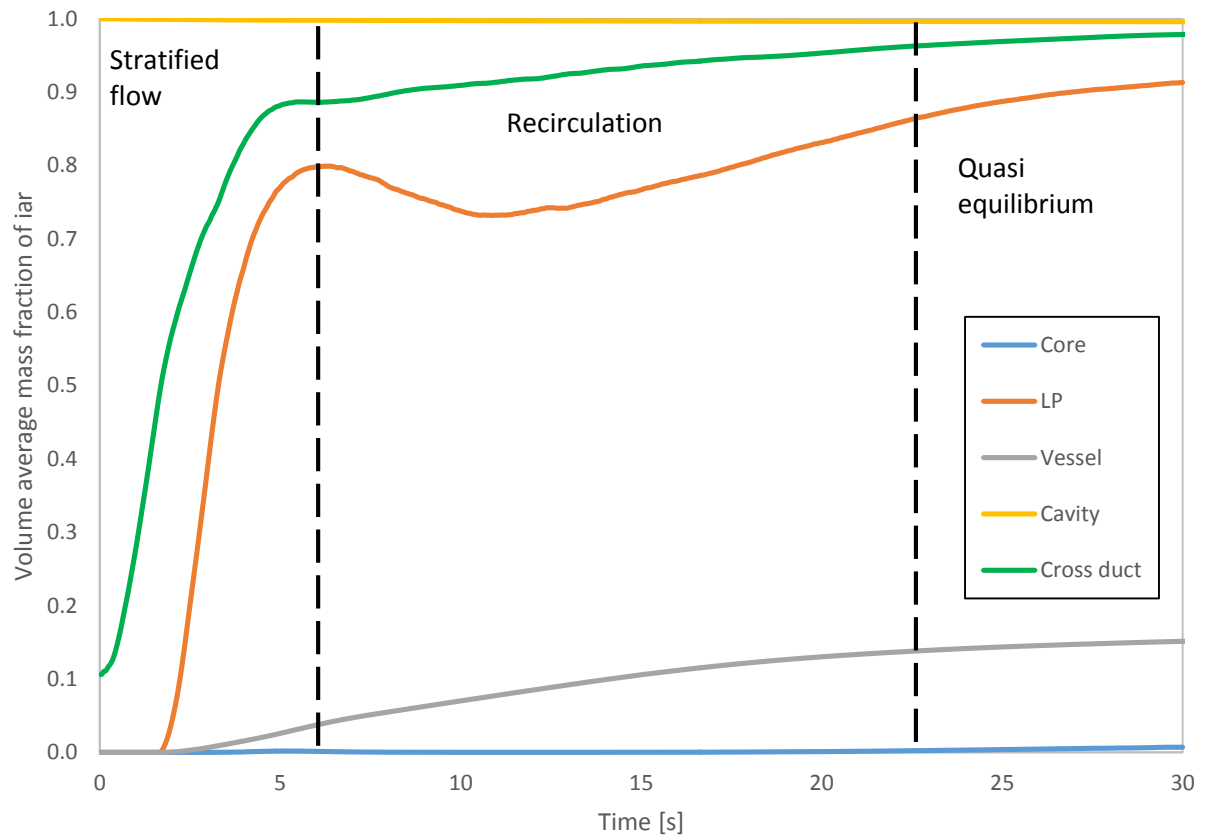


Figure 67 Volume average air mass fractions in different zones.

In order to investigate how the exchange flow phenomena will proceed in the prototype design, a full scale model of the MHTGR reactor was simulated. In order to establish this model, the previous geometry was scaled by a factor of four and new porous body parameters were set (volume increase by a factor of 64). Obtained results are presented in Figure 68. 'Pure' stratified flow (before air wave rebounds from lower plenum side wall) lasts around 6 sec in the HTTF case and extends to 12 sec in the prototype. This stays in agreement with the time scaling ratio for the horizontal flow, which according to equation (27) should be equal: $(t_{EX,H})_R = 1:2$. [93]

Analogous conclusion can be made on the horizontal exchange flow velocity scaling. According to equation (26), $(u_{Brk,H})_R = 1:2$ [93]. Considering air current speed, equal to 1.2 m/s in the MHTGR case (Figure 69), it over predicts it only by 0.1 m/s (comparing to 0.55 m/s in the HTTF). On the other hand, the velocity of helium leaving the vessel is almost four times higher than in the HTTF simulation (4.7m/s versus 1.15 m/s).

Another difference arises from the volume average air concentrations in the lower plenum of both reactors. In the prototype case, the air amount in the lower plenum at the end of initial stratified flow phase is around 20% higher than in the HTTF simulation. After the stratified flow, the rebound phase is enhanced in the MHTGR and air concentration finally drops to the same level as in the HTTF at the rebound concentration drop point.

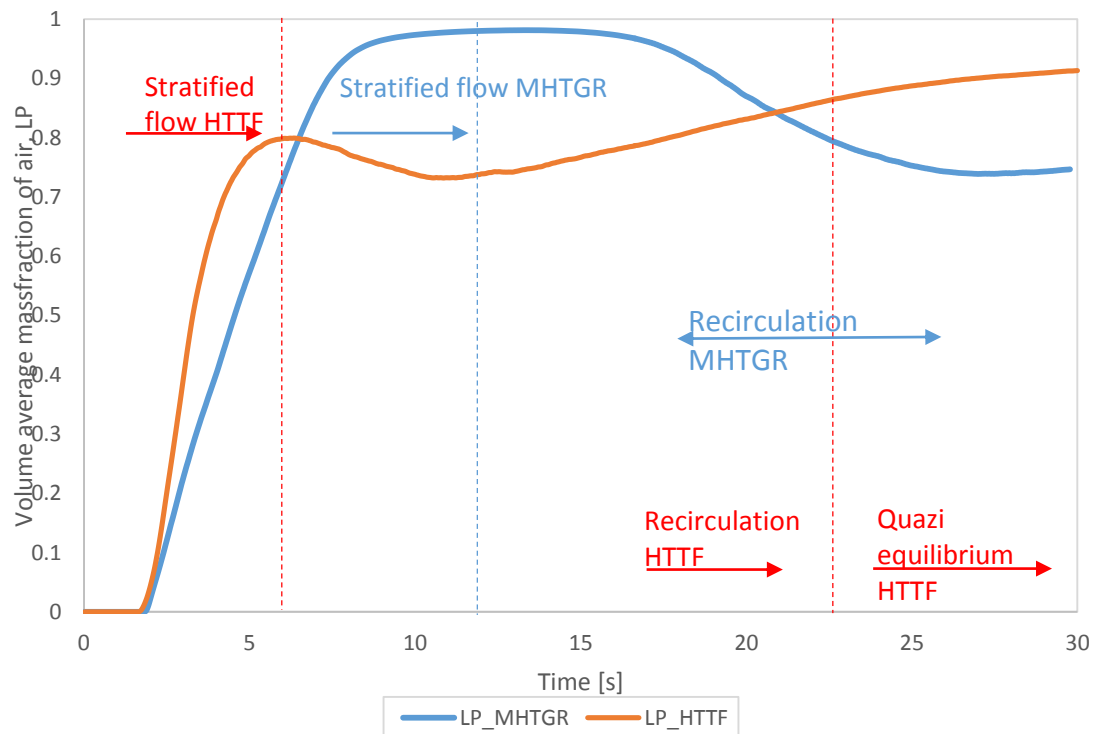


Figure 68 Comparison of volume average air mass fractions in the lower plenum in the HTTF and MHTGR.

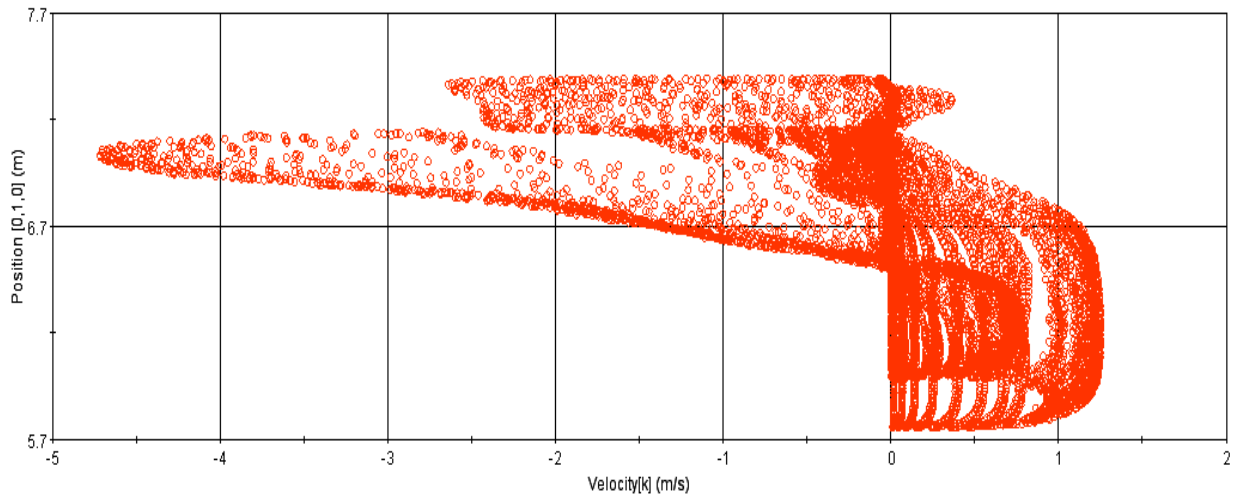


Figure 69 X-Y velocity profile at Rake cross section at 20 sec from the beginning of the transient.

Oh et al. (2011) criterion for the Stage 2. Stratified flow, that includes thermal stratification of air to the core volume before molecular diffusion stage, is investigated (equation (10)). To apply the condition, the following parameters were applied: core height equal to 3.0 m (from lower plenum roof up to the upper reflector), cross duct diameter equal to 0.3 m and average density of gas mixture in lower plenum and helium in the core, equal respectively to $0.665 \frac{kg}{m^3}$ and $0.052 \frac{kg}{m^3}$. Density and temperature distributions in the center of the lower plenum at $t=30$ sec is presented in Figure 70.

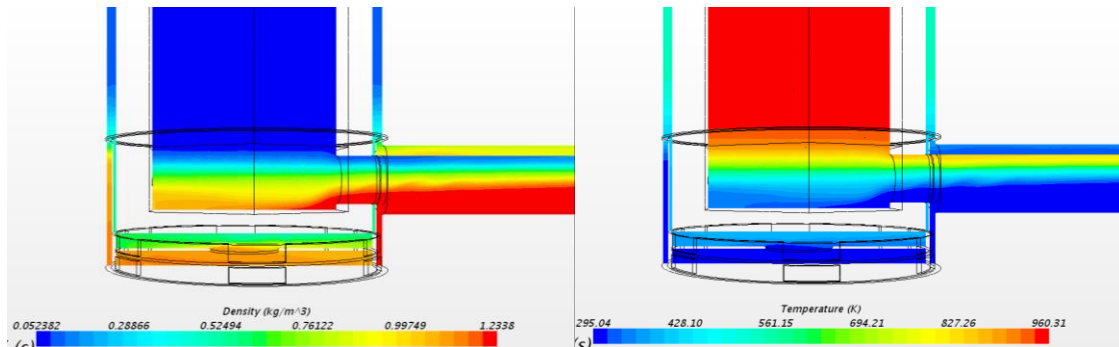


Figure 70 Density (left) and temperature (right) distribution in the lower plenum at $t=30$ sec, baseline study.

Using above values thermal stratification will lead to local natural circulation at the lower plenum-core interface according to criterion expressed by equation (10) and flow can be considered as convection dominant. According to study done by Oh et al. (2011) on the GT-MHR lock-exchange phenomena, flow is mainly affected by convection and air starts entering core volume after 10 sec from the beginning of the transient. Air managed to propagate to the top of the core after another 50 sec. This indicates the very short time scale of the problem and provides directions for the immediate initiation of the air ingress mitigation concept once depressurization starts. In case of this study, heat transfer contribution was not analyzed, so in Figure 71, onset of local natural circulation can be seen at $t=12$ sec, but in subsequent phase, air propagation is not as rapid as indicated by Oh et al. (2011).

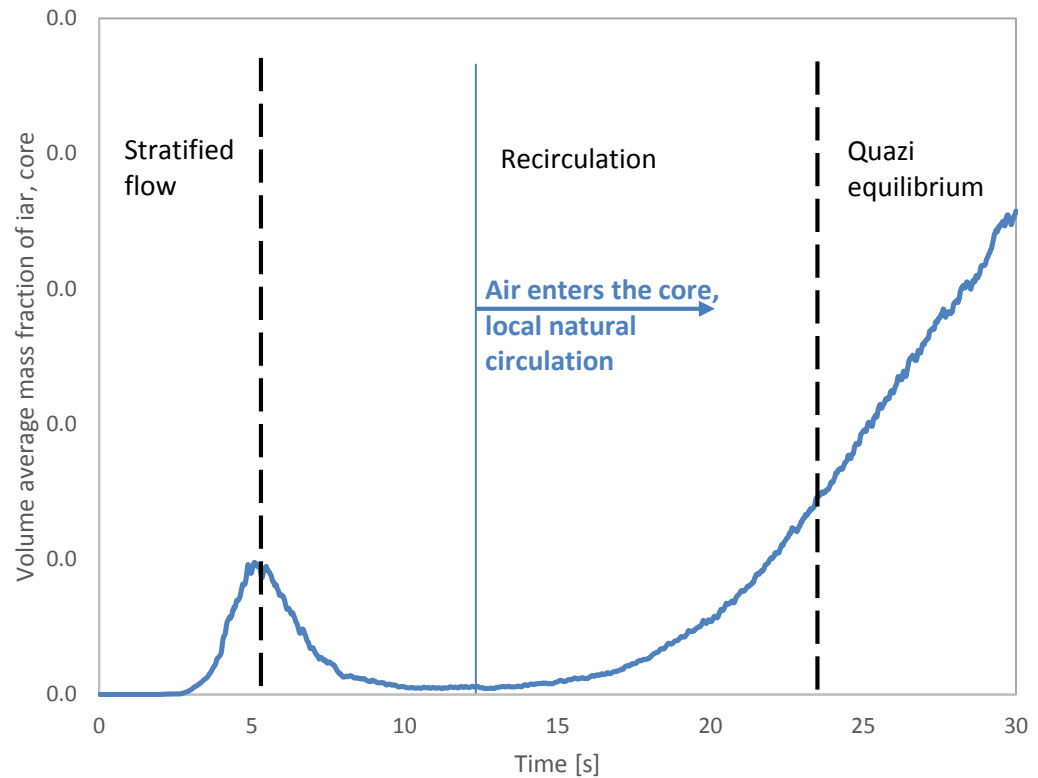


Figure 71 Onset of Stage 2 stratified flow indicated by volume average mass fraction of air in the core as a function of time.

6.3 Lock exchange flow - detailed lower plenum model

By setting the porous body approach to model the lower plenum and core structure in the HTTF system, it becomes impossible to further provide the exact velocity profile between for instance selected lower plenum support posts. One can obtain only the fluid velocity field in averaged sense [92]. Support posts are obstructions for the cold current reaching the lower plenum and it is anticipated that they will affect the exchange flow time scale and velocities. In order to capture the influence of the lower plenum detailed structure that includes over 160 graphite support columns, complete lower plenum design was modeled and implemented in the CFD calculations. This model on the other hand does not take into account the influence of core, upper plenum, upcomer and outer duct regions.

All initial conditions were applied with analogy to the lock-exchange flow setting in the porous model analysis. Domain was meshed with analogous models to previous simulations and the number of cells equals to 3 337 435 (with 2 721 907 cells in the lower plenum). In the lower plenum interface with core, wall boundary condition was placed. Similarly to previous cases, the system is already assumed to be depressurized. Pressure is set to atmospheric conditions and gases are considered to be in the stagnation initial condition.

Figure 72 presents sequence of events in the lock-exchange flow simulation with detailed lower plenum structure for 1.5, 6.0 and 35.0 sec respectively. Comparing to results presented in Table 11 **Error! Reference source not found.** and looking at REF _Ref421022867 \h Figure 72, stratified flow occurs more slowly in the case with support posts included in the lower plenum geometry during around first 10 seconds of the simulation. This might be due to the higher flow resistance caused by support columns in the cross-flow direction than calculated porous body parameters predict. On the other hand, core region was not considered in this analysis so there was less helium available to share in the stratified flow process, which may indicate why gas velocities at $t = 10$ sec (Figure 74), increases by a factor of two (compare with Figure 41). Rebound phase is not present in the graph showing the volume average mass fraction of air in the lower plenum (Figure 73). Most likely, local rebounding areas occur in the vicinity of particular posts and it was not captured by graph showing volume averaged values. Besides, since there is no helium stream that leaves the core and drag rebounding air with it, even if local air recirculation occurs, it does not leave the lower plenum volume.

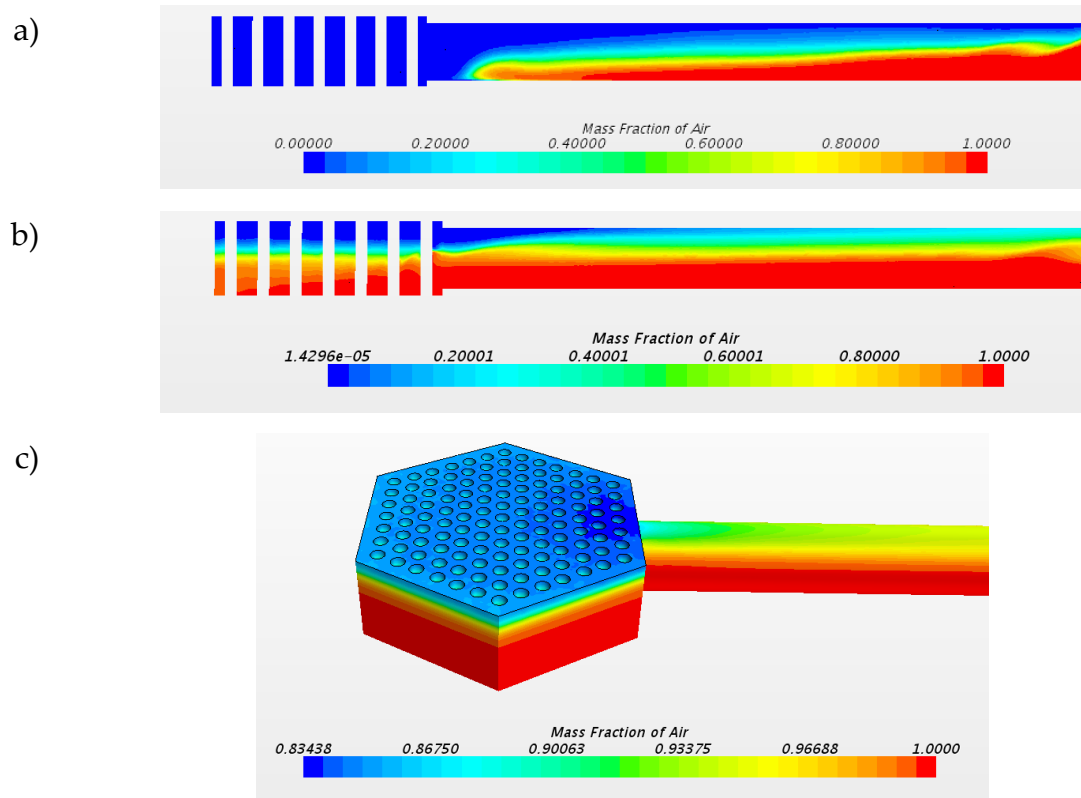


Figure 72 Sequence of lock-exchange flow events in the detailed lower plenum geometry simulation: figure a) shows cold plume propagation at 1.5 sec from the beginning of the transient, figure b) presents progress 5 sec later) while final stage at 35 sec is shown in figure c).

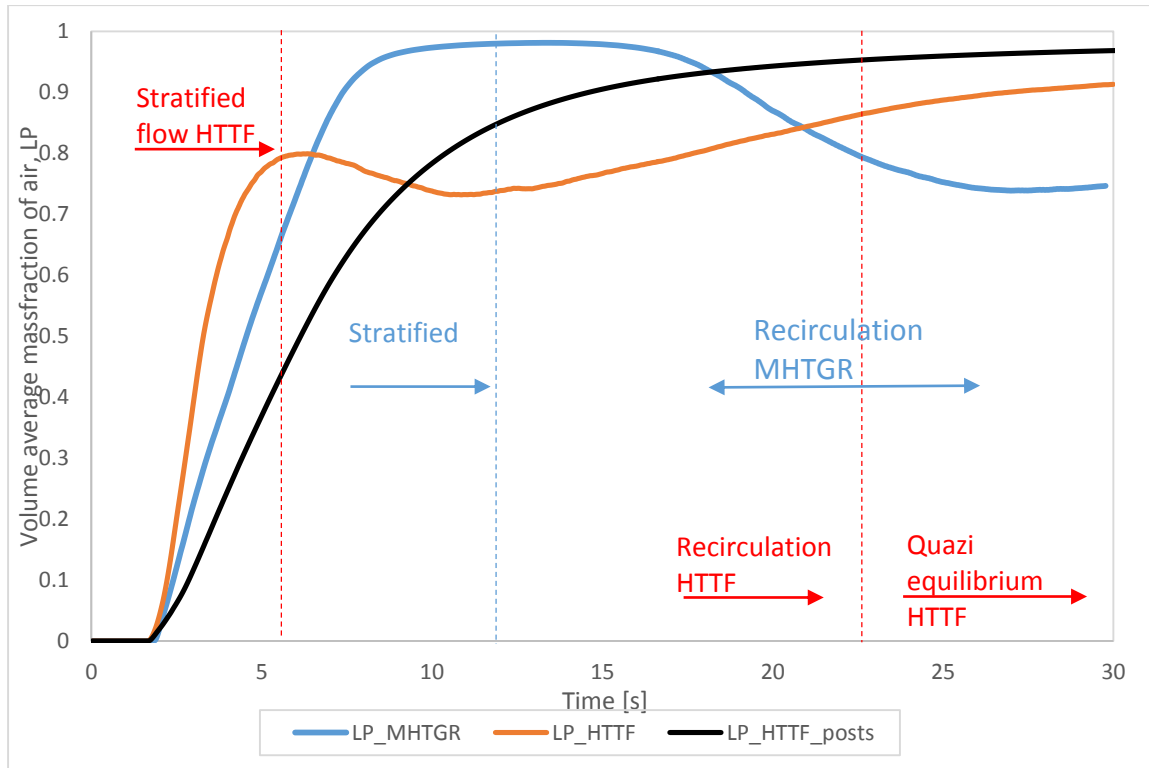


Figure 73 Comparison of volume average air mass fractions in the lower plenum in the baseline HTTF simulation with porous domain approach, MHTGR and detailed lower plenum simulation.

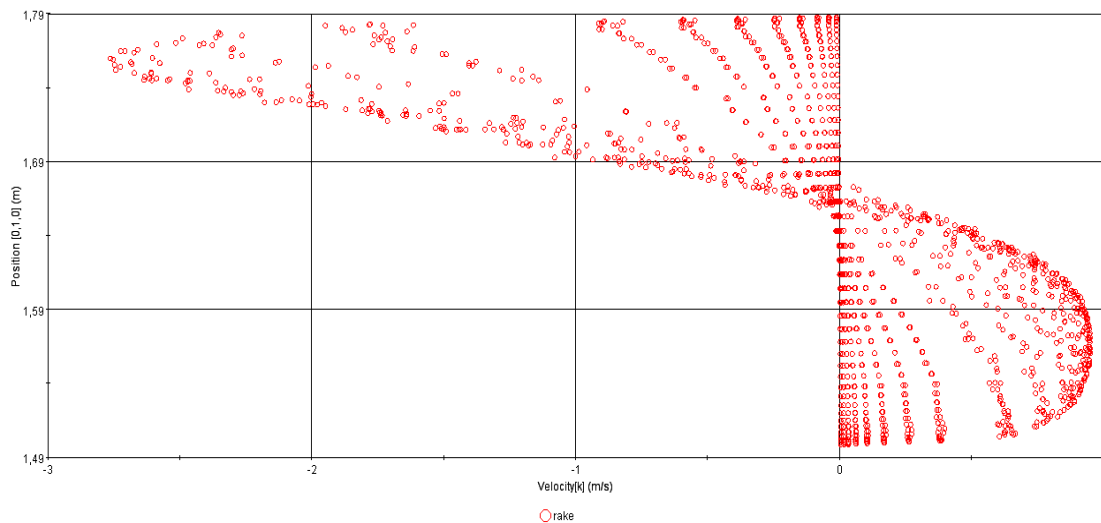


Figure 74 X-Y velocity profile at Rake cross section in detailed lower plenum model.

To provide insight into detailed velocity and air concentration distributions in the lower plenum structure (which could not be done with porous body assumption), scenes at particular cross sections (Figure 75) at 6.5 sec from the beginning of the

transient are presented in Table 12. These particular cross sections were selected so that the flow pattern impacted by air cold current in the lower part of the domain can be seen along with the upper part occupied by helium current and middle cross section that depicts interface among air and helium streams. At the lower cross section, air velocity distribution follows symmetrical, regular pattern: stream is directed at the 60° angle to the cross duct central horizontal axis. Additional effect of the posts implementation is that they act as a momentum sink, reducing the speed of air entering the domain. Regular flow pattern of helium leaving the lower plenum structure is shown at the upper cross section as well (there are no turns around posts volumes). Less ordered velocity distribution is present at gases interface in the middle lower plenum cross section.

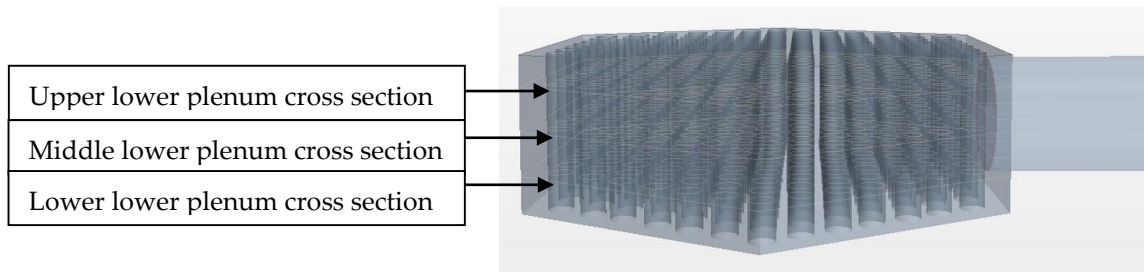
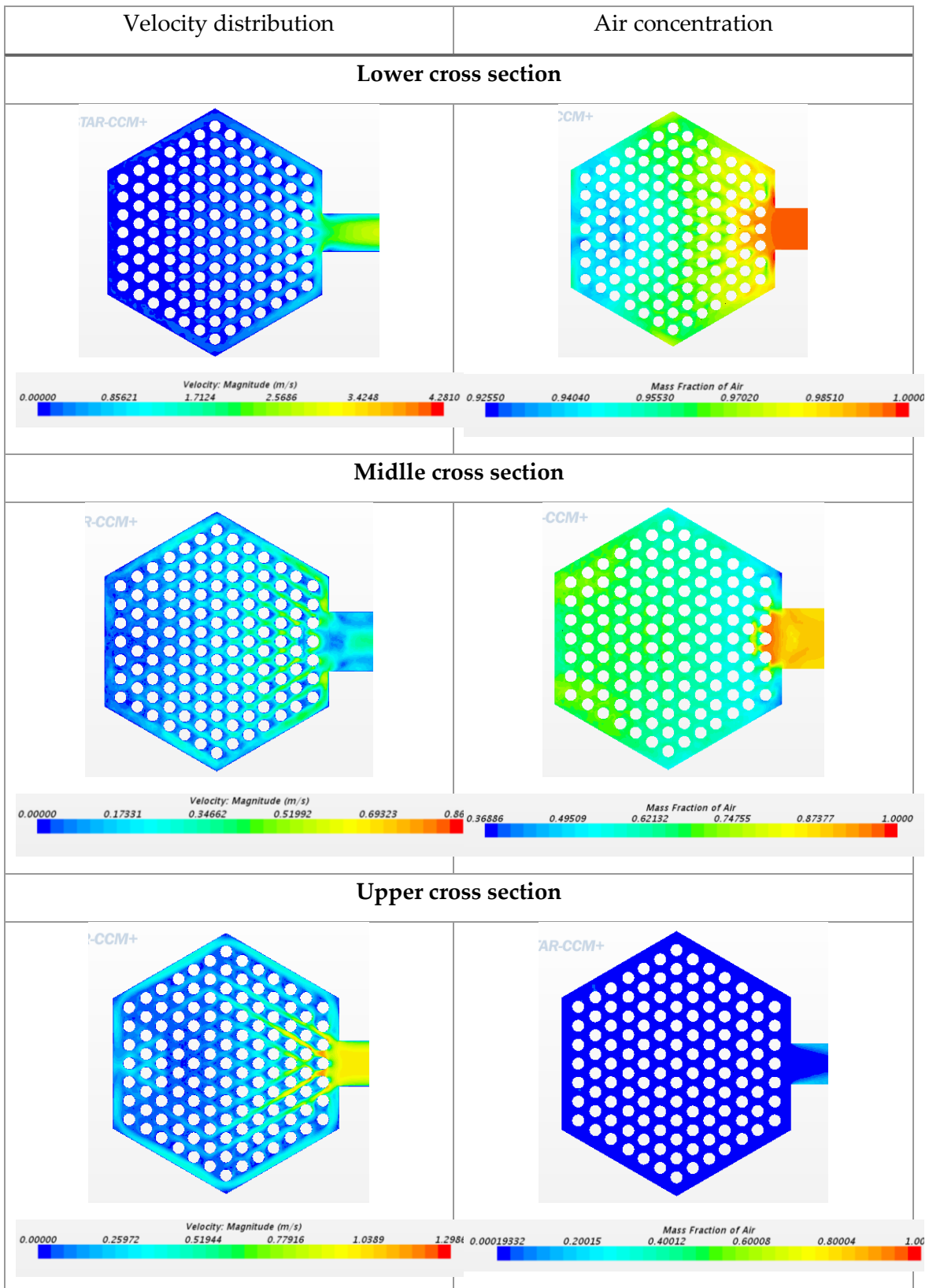


Figure 75 Detailed lower plenum cross sections, used to investigate velocity and air concentration distributions.

Table 12 Velocity and air concentration distributions at particular lower plenum cross sections in the case with detailed lower plenum geometry modeled.



Even though, detailed lower plenum lock exchange flow simulation reduces the human error associated with geometry simplification and physical modeling error coupled with uncertainties that arise from porous model implementation it can provide reasonable results on the mitigation concept efficiency only if core volume is simultaneously analyzed. Core region should be taken into account in the lock-exchange flow simulation to account for the gas diffusion into this domain and exclude helium recirculation to the cross duct and cavity. It is expected that computational time would be greatly extended if detailed lower plenum domain would be implemented together with porous core volume, not to mention detailed core geometry.

6.4. Mitigation concept

A secondary gas injection concept was proposed and modeled in STAR-CCM+ software to show the mitigation potential of the air-ingress into the reactor internal structures during D-LOFC scenario. The focus of the mitigation sensitivity is to reduce the mass fraction of air that will enter the lower plenum at the beginning of the transient. By preventing air ingress at the early stage of the accident, oxygen entrance to the reactor core can be excluded. Several cases were considered with different gases being injected into the lower plenum, varying injection velocities and injection diameter or placement. Results were also compared with the base case analysis without helium injection activation. In each scenario gas was injected at a normal direction to the lower plenum wall, at atmospheric pressure and temperature equal to 300 K. Table 1 summarizes the sequence of simulated scenarios. Firstly helium secondary injection at three different velocities: 0.5, 1.0 and 2.0 m/s, was investigated and compared with baseline analysis with $v_{inj}=0$ m/s in order to capture the dependence of mitigation system efficiency on the gas insertion velocity. Further steps accounted for the different densities of secondary

gas, thus fluids heavier than helium were implemented: nitrogen and argon. Subsequently, mass flow rate of injected gas was changed by increase of injection cross section and multiplying the injection placement (top and bottom injections). This way it was also possible to examine the impact of secondary gas jet position on the mitigation efficiency. Sensitivity study simulations of the mitigation concept were run for 30 sec from the beginning of the transient to address early stage of the accident (excludes molecular diffusion and natural circulation).

Table 13 Details of the mitigation method sensitivity study simulations.

Case	Gas	Velocity [m/s]	Placement	Injection diameter [m]	Mass flow rate [g/sec]
1	He	0.5	side	0.025	0.044
2	He	1.0	side	0.025	0.088
3	He	2.0	side	0.025	0.175
4	He	2.0	side	0.05	0.701
5	N ₂	2.0	side	0.025	1.228
6	Ar	2.0	side	0.025	1.750
7	Ar	1.0	bottom	0.025	0.875
8	Ar	2.0	bottom	0.025	1.750
9	Ar	2.0	side , bottom	0.025, 0.025	3.501

6.4.1. Helium injection

The main concept of secondary helium injection into lower plenum is to create two separate layers of air that will accumulate at the bottom part of the domain and secondary helium that will propagate to the upper part of the lower plenum region thus protecting core structures from being exposed to air influence.

To quantify the effect of the injection method, volume average mass fraction of air as a function of time, starting from the beginning of the transient, was measured. First step of the research was to investigate the impact of secondary helium injection at different injection speeds. The goal was to examine reduction of the air ingress, caused by density gradient difference, by the buoyancy force created with additional amount of helium in the lower plenum. Since helium is the working fluid in the HTTF, it was implicitly assumed that injection of this gas, if results with compelling impact, would be the most desirable.

Helium was injected at three different velocities and compared with the baseline study. Firstly, the time for the air plume to reach the instrumentation Rake was measured. It can be seen that secondary helium insertion does not have a meaningful impact on the delay in the air cold plume progression in the cross duct (Table 14). Although slightly noticeable, the analyzed cases present increase in the measured time to reach the Rake cross section. This provides a sense of impact of the injection mass flow rate on the mitigation concept efficiency and indicates the direction for further conceptual analyses. Moreover, the mitigating system should be able to enter sufficient amount of secondary gas so that when air plume reaches the lower plenum inlet, after 2 sec from the beginning of the transient, there will be enough secondary fluid to displace or block the air ingress.

Table 14 Approximate times for air current to reach instrumentation Rake.

Case	Injection velocity [m/s]	Time [s]
1	0.0	1.35
2	0.5	1.36
3	1.0	1.40
4	2.0	1.60

Considering volume average mass fraction of air in the lower plenum (Figure 76), case with $v_{inj}=2.0$ m/s presents reduced amount of air volume almost through the entire simulation time, by 5 % on average. Case 2. also results in reduced volume fraction of air in the lower plenum (2.5%).

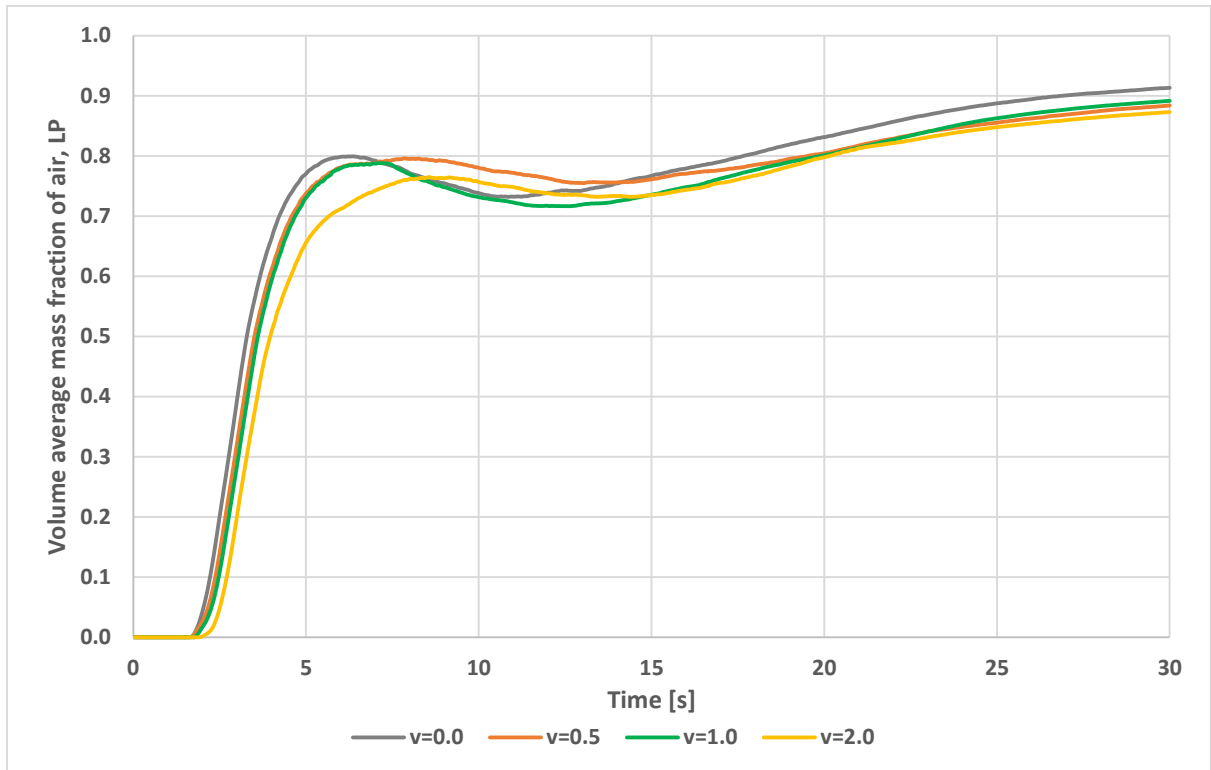


Figure 76 Volume average mass fraction of air as a function of time in the lower plenum.

Helium, being lighter than air, propagates to the upper part of the lower plenum after being injected. Then it travels along with hot helium that leaves the core to the inner cross duct. This way, mitigation system efficiency concentrates at the interface between the core and lower plenum and only slightly influences the volume average mass fraction of air in the lower plenum (Figure 77).

Results show that secondary injection of helium into the lower plenum can reduce air ingress because of two factors: first is simple replacement of gases and air recirculation while second is the air-core separation created by the secondary helium injection layer that will occur at the top of lower plenum (Figure 78). This

helium layer will be created because injected helium has lower temperature than helium in the core (this will hold the injected amount of gas in the lower plenum region) and on the other hand, helium, being lighter than air will recirculate to the top of lower plenum once air will ingress this domain (buoyancy force).

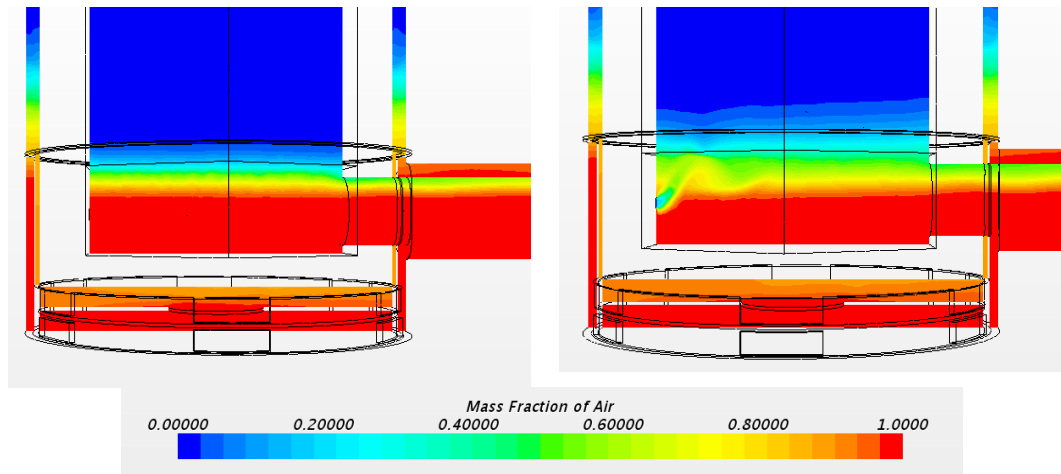


Figure 77 Distribution of mass fraction of air in the baseline model and in the case with helium injection, $v_{inj}=2$ m/s, $t=30$ sec.

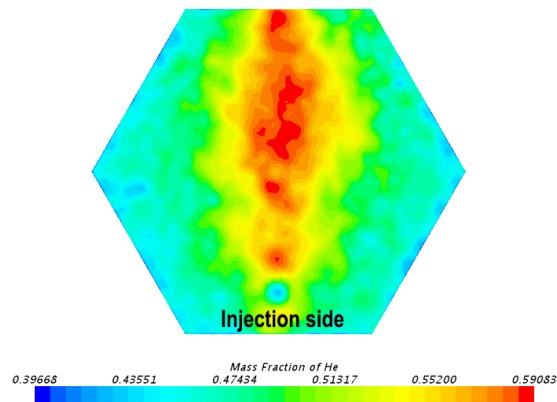


Figure 78 Mass fraction of helium at the lower plenum - Core interface ($v_{inj} = 2$ m/s, $t=35$ s).

Since the trend of increase in reduction of amount of air in the lower plenum due to increase in the injection velocity or mass flow rate was demonstrated, it was decided to leverage this tendency if the injection diameter would be increased by a factor of two (thus mass flow rate will increase by a factor of four). Volume average mass fraction of air the lower plenum is reduced to 0.82 (Figure 79).

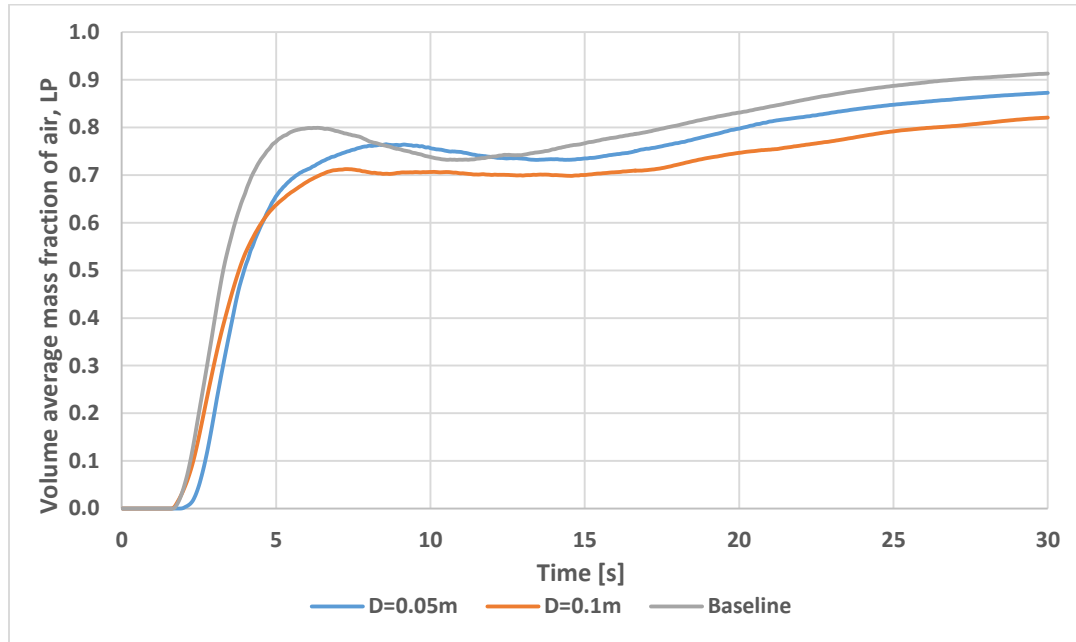


Figure 79 Comparison of volume average mass fraction of air in the LP between helium, LP side injection with $D=0.1$ m and $D=0.05$ m at $v=2$ m/s.

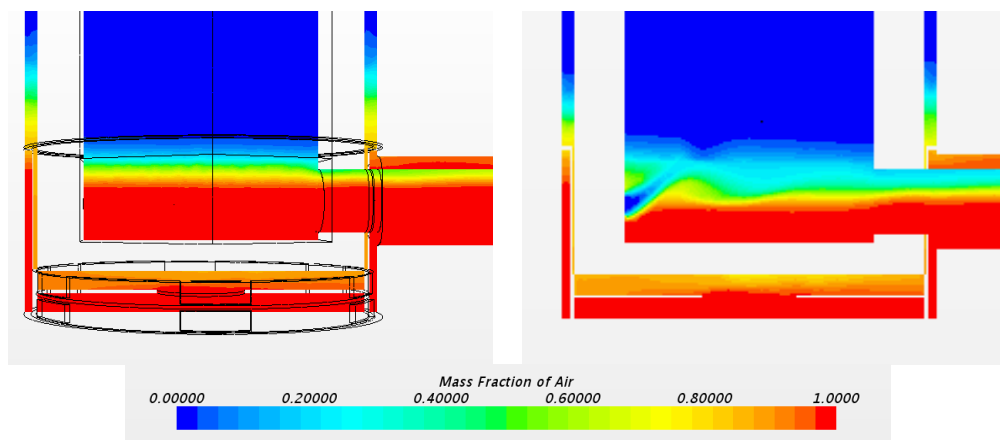


Figure 80 Distribution of mass fraction of air in the baseline model and in the case with increase diameter of helium injection, $t=30$ sec.

In the following injection study simulations, injection velocity will be fixed to $v_{inj}=2$ m/s to allow for comparative analyses among different mitigation concepts, according to gas densities and injection placement. Also, since increase in injection diameter can influence the structural design of the lower plenum, further concepts will be performed with $D=0.025$ m and mass flow rate will be modified by changes in the secondary gases densities.

6.4.2. Nitrogen injection

Subsequent step in the framework of air ingress mitigation study involves study on the secondary gas (nitrogen) density effect on the reduction of air volume fraction in the lower plenum. This way the injection mass flow rate is increased by a factor of 6.86 comparing to the case with helium injection at 2.0 m/s without increase in the injection diameter. Nitrogen interaction with carbon is not appreciable below about 1400°C, so nitrogen will become reactive with the graphite at the highest of accident temperatures.

The same dependence as on the increase in injection velocity is noticed, although the effectiveness is now significantly improved (Figure 81): after 3 sec from the beginning of the simulation, volume average mass fraction of air in the lower plenum is reduced from 0.91 to 0.72 (comparing to helium injection, it was reduced to 0.88). Because air in the lower plenum is diminished by almost 20% at the end of simulation, it became clear that next step should involve implementation of a fluid that will compromise the following criteria: dense enough to delay and reduce air ingress by even higher factors and at the same time do not influence core and lower plenum internal structures (inert gas).

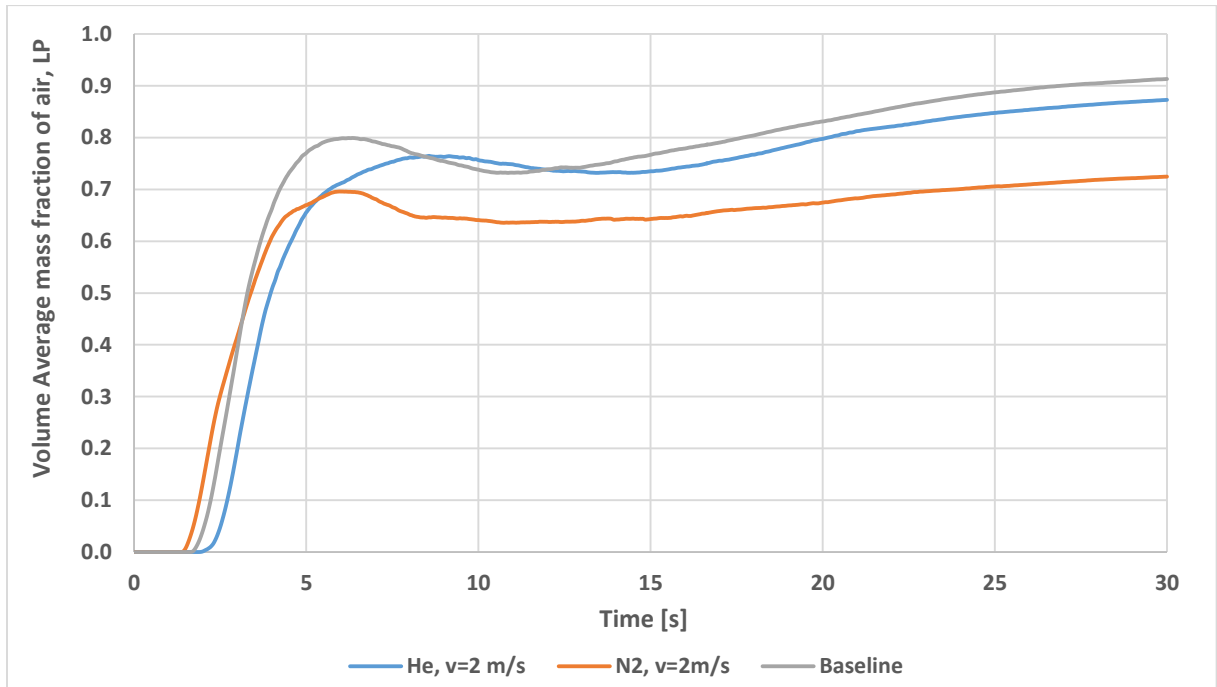


Figure 81 Comparison of volume average mass fraction of air in the LP between helium and nitrogen, LP side injection at $v=2$ m/s.

Below figure clearly shows the influence of the side Nitrogen injection on the air mass fraction reduction in the lower plenum.

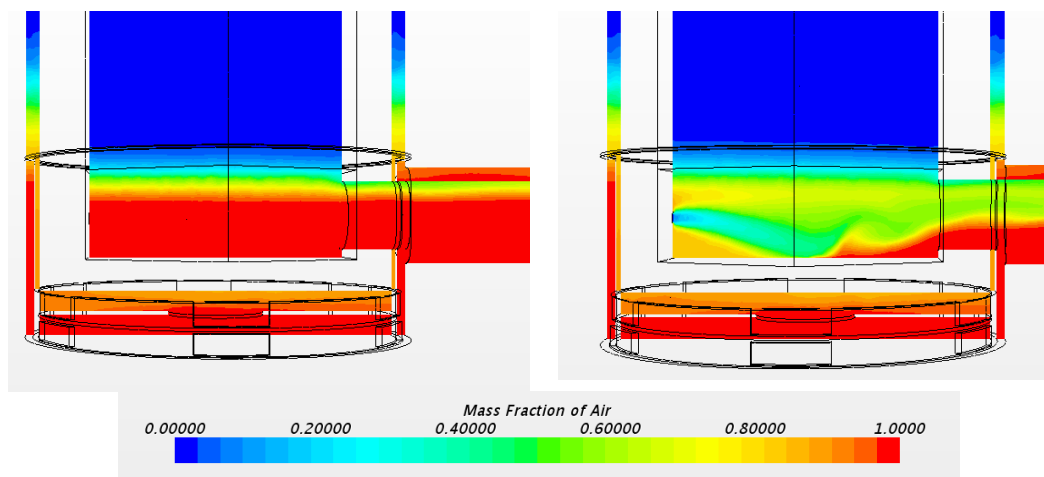


Figure 82 Distribution of mass fraction of air in the baseline model and in the case with side nitrogen injection, $v_{inj}=2.0$ m/s, $t=30$ sec.

6.4.3. Argon injection

Potential of argon as a mitigating fluid is also inspected because of its high density (higher than air) and because it is an inert gas (it will not react with graphite at high temperatures). Argon is commonly used in high-temperature industrial processes, as for instance inert shielding gas in welding process or in graphite electric furnaces. Injecting argon as a mitigating gas into the lower plenum will allow to investigate the influence of mitigating capabilities of a gas heavier than air. Argon, being heavier than helium and air will be distributed at the bottom of the lower plenum, blocking the air nose from entering the lower plenum region. Figure 83 presents comparison among nitrogen and argon injections at 2 m/s with the baseline case. Volume average mass fraction of air is reduced by 0.4 by argon application. This results in almost twice higher reduction of air concentration in the lower plenum domain than in case with the nitrogen injection.

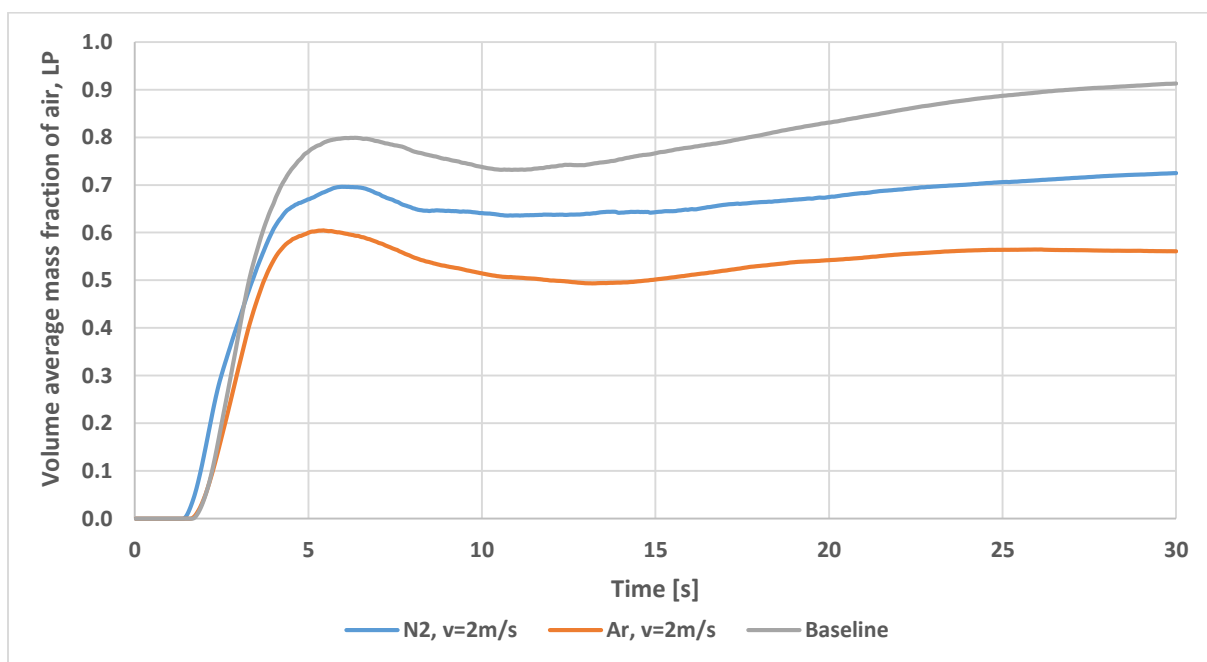


Figure 83 Comparison of volume average mass fraction of air in the LP between argon and nitrogen, LP side injection at $v=2$ m/s.

Since impact of argon injection is significant, injection placement study was conducted with argon as a mitigating fluid. Injection placed in the middle of the bottom lower plenum wall was checked. It was believed that heavy gas will immediately accumulate at the bottom of the lower plenum again, blocking air access to this region. Velocity of argon at the bottom injection is equal to 1.0 m/s and 2.0 m/s. Figure 84 presents that bottom injection also provides promising results, but not as effective as side argon implementation but still more effective than nitrogen side injection. There is no impact on the injection velocity in this case (same results for 1.0m/s and 2.0 m/s).

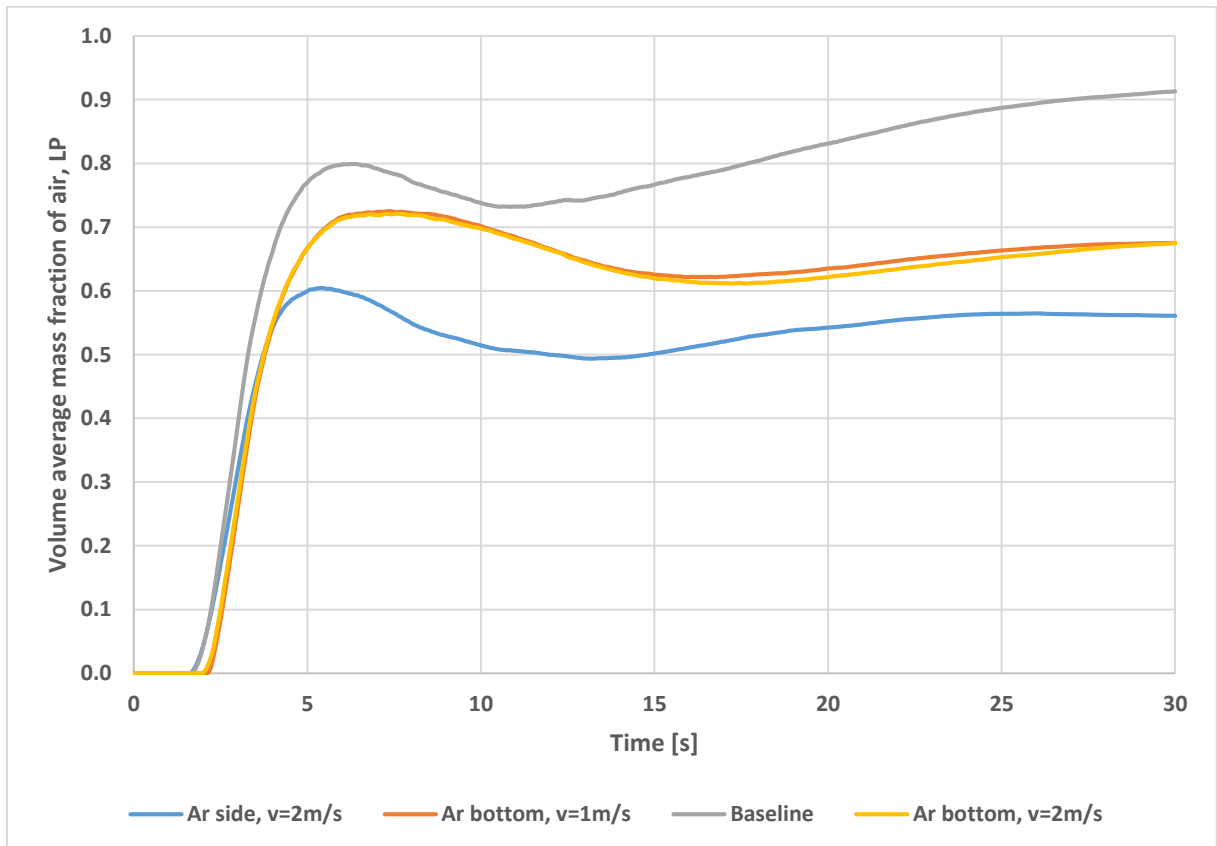


Figure 84 Comparison of volume average mass fraction of air in the LP between argon, LP side injection at v=2 m/s and LP bottom injection at v=1 m/s and 2 m/s.

Having the knowledge about the influence of gas density and velocity on the average amount of air in the lower plenum, it was decided to couple the argon

concept with the additional added value that would be created by increase in the injection mass flow rate but not directly by the increase of the injection diameter but by coupling concepts of the side and bottom argon injections at 2 m/s. Figure 85 shows the result of the described concept. Air concentration in the lower plenum is reduced by a factor of 5.4 after 30 sec from the beginning of the transient in the case with side and bottom injections implemented jointly. Moreover, this concept shows that air concentration in the lower plenum is not only reduced during the stratified flow phase (and then follows the same distribution as the baseline case but at lower air concentration level), but continuously replaces air from the lower plenum by pushing it back to the cross duct during recirculation and quasi equilibrium stages.

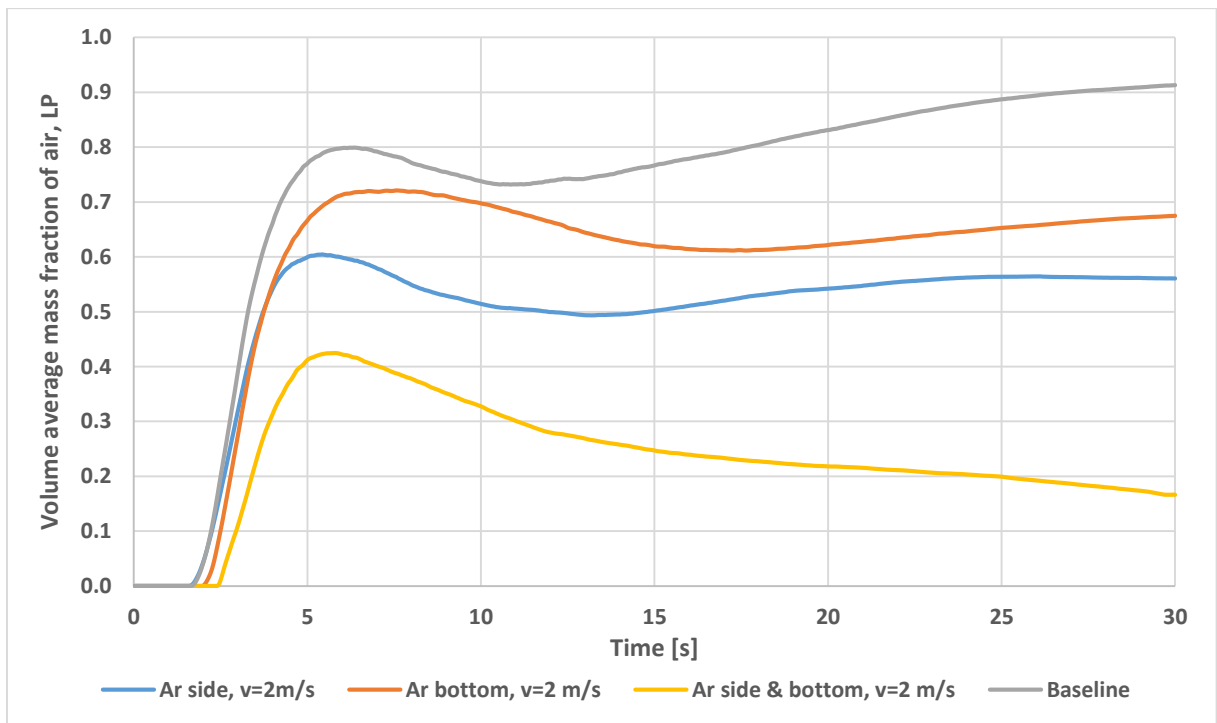
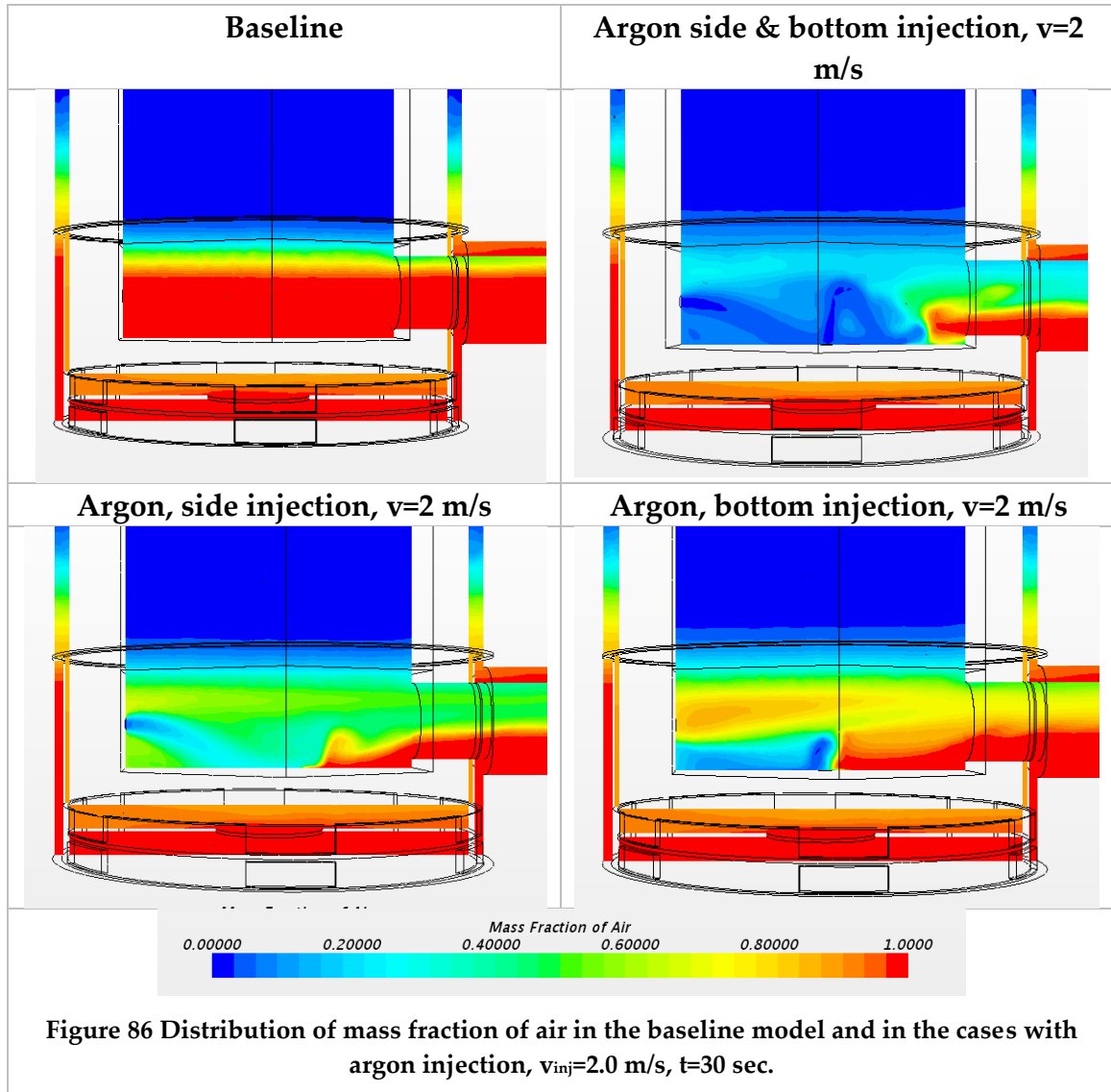


Figure 85 Comparison of volume average mass fraction of air in the LP between argon, LP bottom injection, LP side injection and LP bottom & side injection simultaneously at $v=1$ m/s.

Figure 86 presents the distribution of mass fraction of air in the lower plenum cross section plane at the end of the simulation (30 sec) in the baseline and argon injection cases. Volume average mass fraction of air is reduced to 0.17 by dual argon injection. One can notice how side and bottom injection momentum adds up to prevent air current propagation to the lower plenum.



As expected, argon accumulates at the bottom of the lower plenum. Argon streamlines distribution presented at Figure 87 shows that indeed stagnation zone is created in the left part of the domain. Near the cross duct, recirculation zone

exists that removes air from the region and is responsible for the continuous air replacement that was shown in the Figure 88. Mixture of air and argon leaves the lower plenum at average velocity equal to 0.65 m/s.

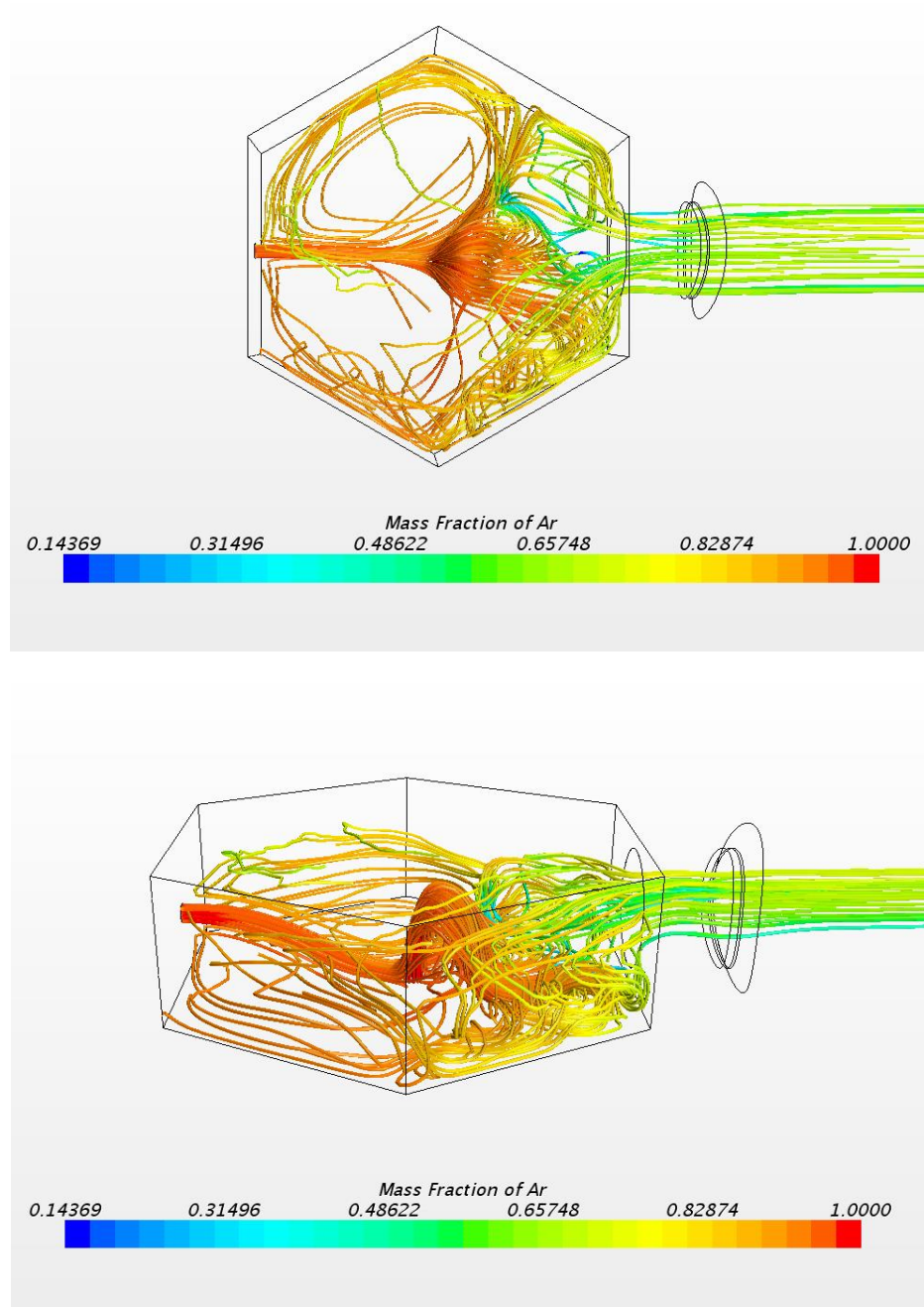


Figure 87 Argon flow streamlines indicating mixing with air (mass fraction of air), top and side views, $t=30$ sec.

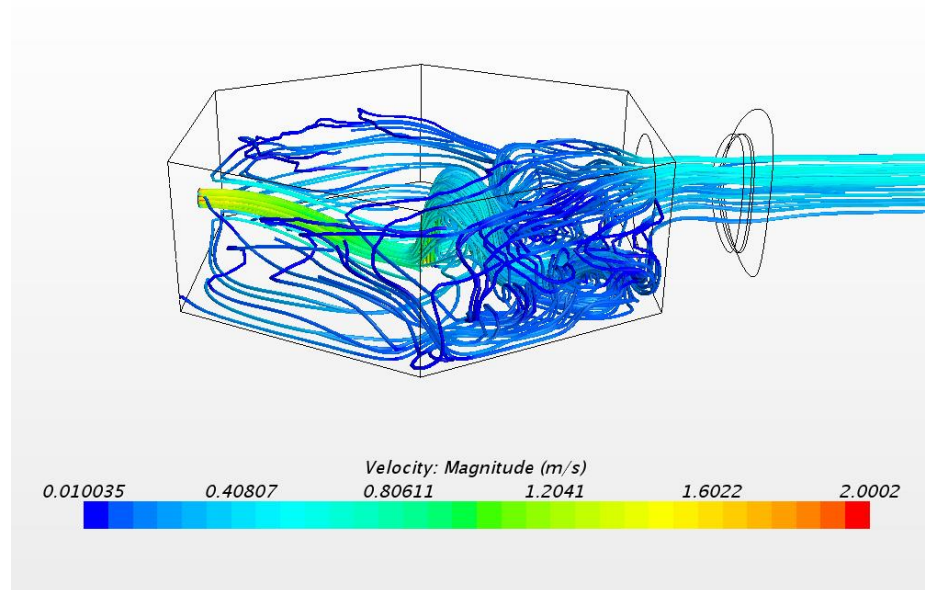


Figure 88 Argon flow streamline, velocity distribution, side view, t=30 sec.

6.5. Comparative study of considered mitigation methods

All analyzed cases are qualitatively compared in this subsection. Figure 89 reflects a summary of the conducted mitigation concept sensitivity study. Considering only side injection, there is a clear analogy among increase in secondary gas mass flow rate and reduction of air concentration in the lower plenum. Mass flow rate can be increased directly by changing injection diameter or velocity or by changing the injection working gas into denser one. Comparing injection placement, analogy to the mass flow rate does not play a role: almost the same reduction effect is obtained if argon is injected at 1.0 and 2.0 m/s. The most promising method of air ingress mitigation, among considered cases, is the joint side and bottom argon injection. Volume average mass fraction of air is reduced by over 81% in this case comparing to the baseline analysis.

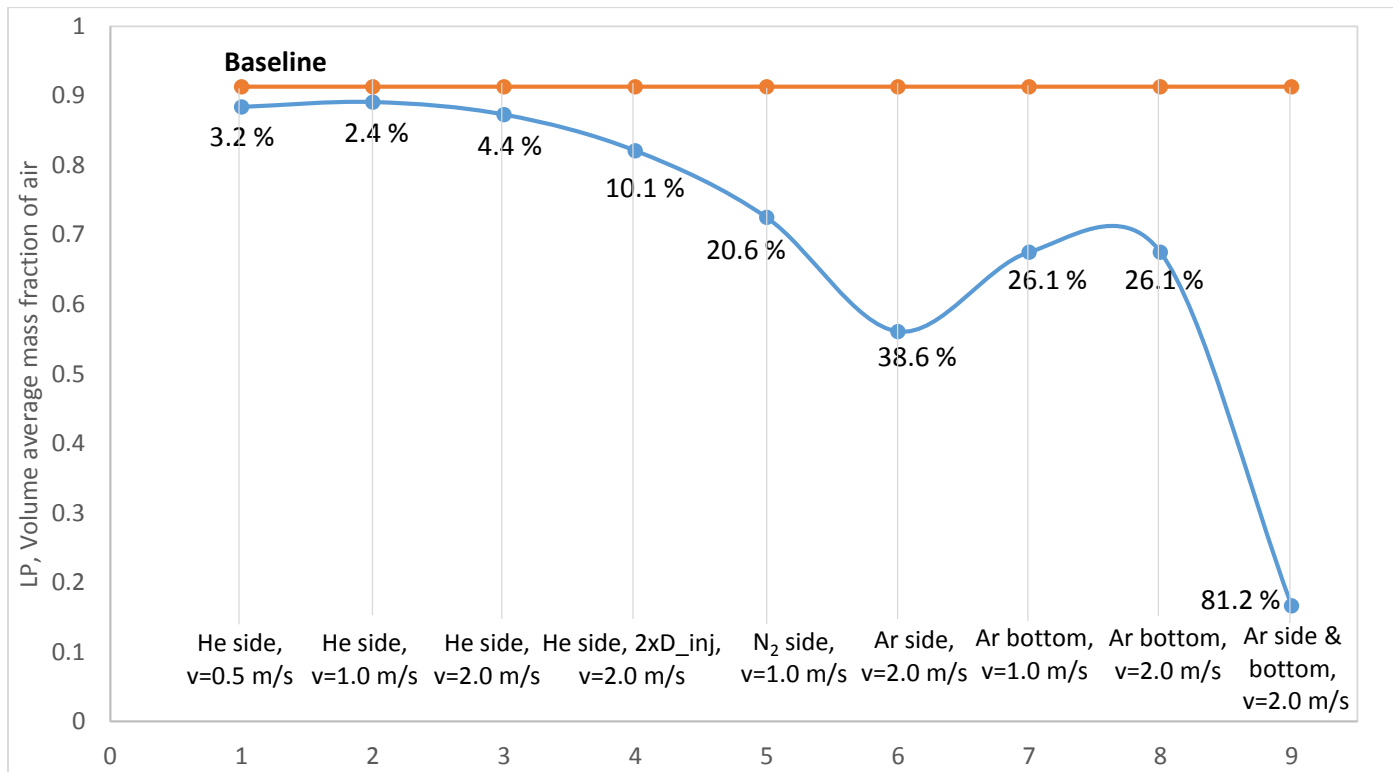


Figure 89 Comparison of the efficiency of the analyzed mitigation concepts.

To ensure that double injection method will be the most efficient solution, air concentration surface maximum is investigated at the section of interest. Placement of cross section for air surface concentration comparison is shown in Figure 90.

Figure 91 presents that despite of secondary helium injection with $D=0.025$ m, all cases reduce surface maximum at the lower plenum middle plane. Cases with helium injection does not influence local air maximum at this level. Considering other cross section planes at the lower plenum/core interface and then in the middle section of the bottom reflectors one can notice that in almost all examined cases, local air surface maximum will increase. This indicates that even though air concentration in the lower plenum is reduced, some portion of air will passage to the core bottom structures instead of being removed through the cross duct. In case of dual argon injection at side and bottom lower plenum walls, surface maximum is reduced at all considered cross section planes.

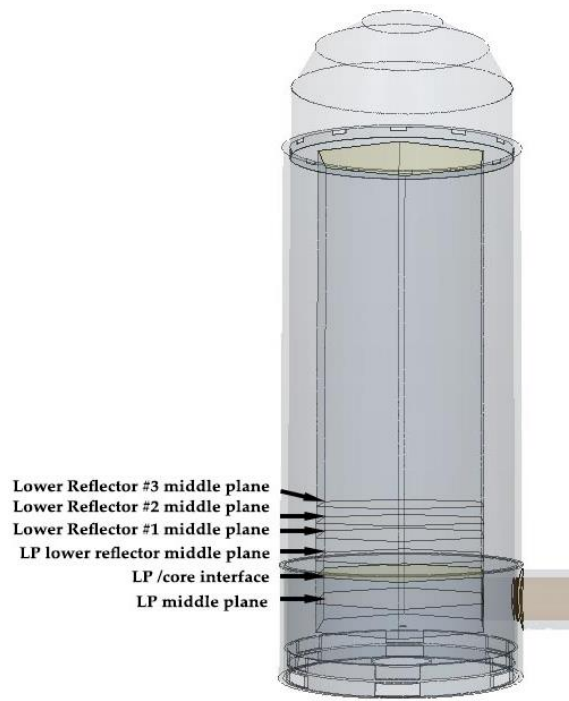


Figure 90 Cross sections placement for the local surface maximum analysis.

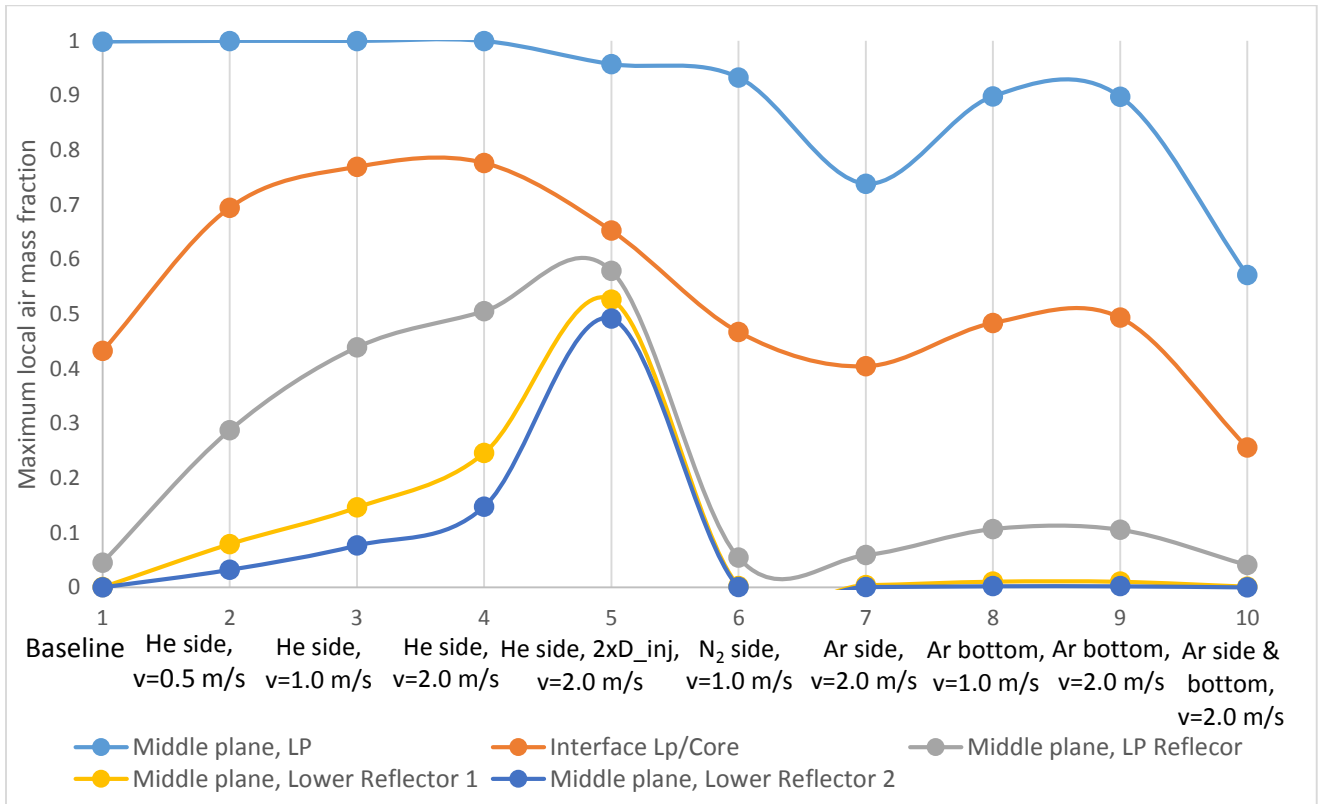


Figure 91 Maximum local surface air mass fraction, comparison between mitigation concepts.

7. D-LOFC mitigation method implementation

To adopt data of graphite oxidation into the mitigation concept applicability, some reference values of temperature, oxygen flow, concentration and graphite type should be selected. According to the report prepared in the RAPHAEL (Reactor for Process Heat, Hydrogen and Electricity Generation) project (European Commission, 2007-2008), during DCC transient, maximum fuel blocks temperature rises up to about 1400°C [6]. This maximum temperature is initially observed at the bottom of the core and then propagates to the center part of the reactor core. Temperature in the lower parts of the vessel (lower plenum) will remain at the level of 1000 K for about 10 h from the beginning of the transient. According to El-Genk et al. (2012) at this temperature level it will take 1.1 h, 1.5 h or 2 h respectively for Reynolds numbers 20, 10 and 5 to reach 10% of the graphite weight loss in the 0.8 m long VHTR fuel channel. At higher temperature (1100 K) it will take only 0.5 h (at Re=20) to lose 10% of graphite mass fraction [16]. Assuming the marginal case, the mitigation system should be capable of preventing the effects of the accident for at least 10 h from the beginning of the transient, until the temperature will decrease and potential oxidation will be reduced. To ensure that no significant damages will occur in the internal vessel structures, mitigation system should provide its functionality until the temperature will drop below 450°C in the lower plenum, which is after at least 55 h from the beginning of the transient.

To check how the system thermal hydraulic response will look like after 30 sec, simulations with open and closed valves were conducted. In Figure 92, it can be seen that after closing the dual injection valve, air mass fraction in the lower plenum continues to increase. On the other hand, if injections will remain active, then air amount will be significantly reduced. It takes circa one minute for the

argon dual injection system to fully fill the lower plenum volume and prevent air ingress to the core. Residual air mass (that managed to enter the lower plenum before it was filled up with argon) is removed through the inner duct. Even though this method presents high potential to prevent core support structures placed in the lower plenum from oxidation, it requires that system will continuously inject secondary gas for about 55 h, until temperature in the core will drop below hazardous values.

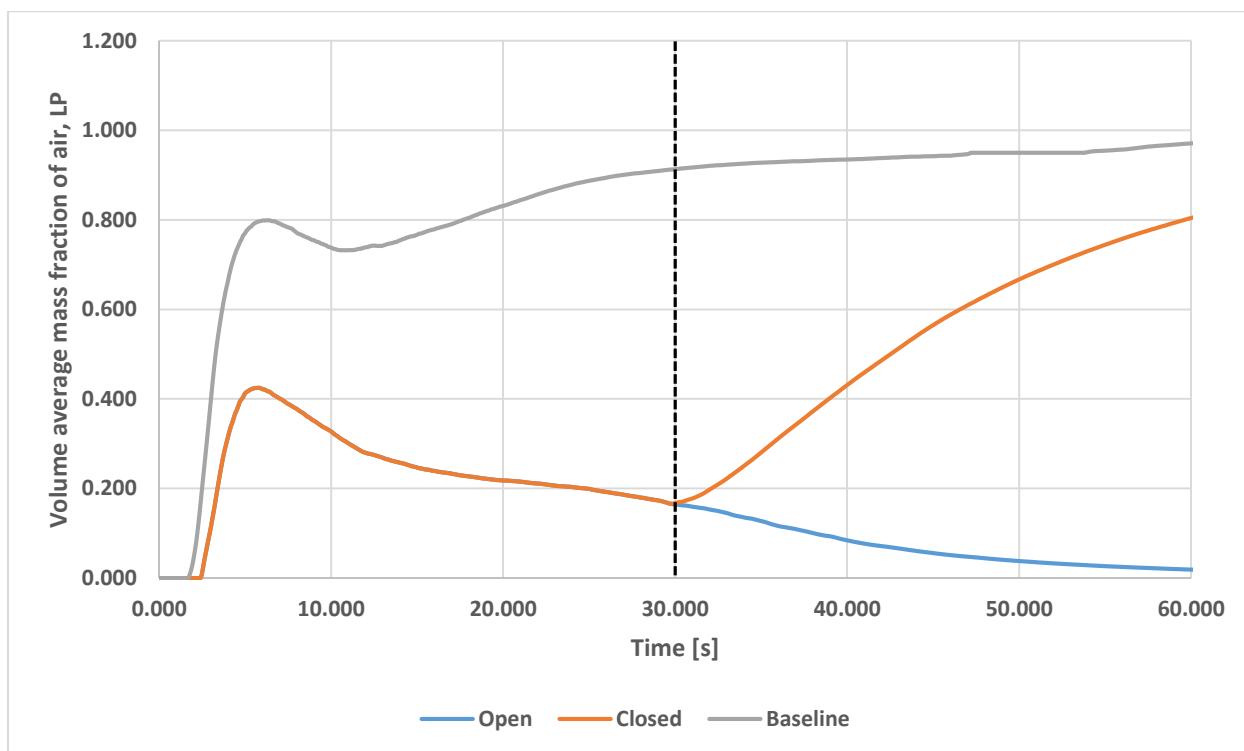


Figure 92 Comparison of mitigation system efficiency (dual argon injection) after closing the injection valve at 30 sec.

To physically apply the mitigation concept, a pressurized tank of argon with a check valve can be implemented. The check valve remains closed when the primary circuit is at full pressure. During an air ingress event, the pressure drops significantly in the primary side. When it drops below the argon tank pressure, the check valve will open to allow the argon to inject. It is important to initiate system operation immediately after signal on pressure boundary break appears. If

valve opening delay would occur, air can enter core structures after very short time scales due to convective dominated Stage 2 stratified flow [66, 55]. If mass flow rate of injected argon is around 3.5 g/sec, then after 55 h, argon mass in the reactor system will be around 693 kg. Tank volume and gas pressure are coupled and would require further transient analysis. From simple calculations, for tank pressurized equal to 80 atm, argon tank volume will occupy 0.2 m³.

8. Conclusions

This study discussed the depressurization and exchange flow stages during the D-LOFC event in the VHTR reactor and proposed a concept to mitigate air ingress into the reactor vessel and lower plenum. The HTTF facility located at Oregon State University was selected as a reference model in the CFD simulations.

Before a baseline simulation was established, sensitivity studies on applied mesh discretization and turbulence model were examined. The laminar case presented reasonable results. The Realizable K-Epsilon turbulence model provided results that were analogous to the laminar case. This model serves well for low-Reynolds number flows and since it could be also implemented in the mitigation sensitivity study, it was selected as a reference model. Three meshes were also analyzed: coarse, medium and fine, from which medium mesh with 5 634 956 elements was implemented throughout the remaining of this study.

Study on the influence of detailed lower plenum geometry was done. Lower plenum posts affect gases flow distribution and air ingress is reduced during first 10 sec of the transient comparing to porous model approach. In order to analyze mitigation concept, core volume has to be included in the simulation to take into account air mass fraction that enters this region at the rebound or local natural convection stages.

In the CFD analysis, during rapid depressurization, shock waves and rarefaction waves are observed. Significant changes in velocity and pressure result in density variations in the entire fluid domain. As a consequence, large temperature variations in the vessel and cavity sides are observed as well. The helium volume mass fraction that enters the cavity during that time is less than 0.5%. This relatively small amount results from the creation of reflected shock waves that

slow down the propagation of the helium concentration gradient to the confinement direction. An analogous situations exist in the vessel side of the system in the subsequent phase, when a reflected wave meets the opposite rarefied wave. These pressure wave oscillations continue until pressure equilibrium is reached around 10 sec from the pipe break initialization.

From the baseline lock-exchange flow analysis, it can be concluded that it takes around 2 sec with average velocity equal to 0.45 m/s for the gravity current leading edge to reach the lower plenum inlet and about 30 sec to fill it up to 90%. During that time, helium leaves the core and lower plenum at a velocity equal to 1.1 m/s. It was shown that flow in HTTF during D-LOFC is convection dominant and the onset of local natural circulation sites creation starts at 12 sec. Thanks to this study, limiting baseline solution has been established, with the assumption of 100% air concentration in the cavity.

Analytical model developed by Oh et al. (2011) for the stratified flow time scale estimation cannot be applied to verify results obtained from CFD simulation. Velocities calculated with reference to work done by Lowe et al. (2005) that included analogy to liquids normalized current height are not applicable in the case of lock-exchange flow of gases.

HTTF stratified flow time scale stays in agreement with prototype model results. MHTGR lock-exchange flow takes twice as much time as HTTF does. This indicated that selected mitigation concept can be successfully applied in the prototype design.

Argon injection at the lower plenum provided results that proves the efficiency of the analyzed method. This system would be able to reduce the amount of air in the lower plenum and consequently air ingress to the core during the exchange flow

stage by 81% with dual argon injection at the side and bottom lower plenum walls at $v_{inj} = 2$ m/s. Additionally, this system can potentially dilute the oxygen concentration in the lower plenum. A mitigation concept should reduce temperatures in the lower plenum and lower part of the reactor core influencing the scope of the thermal stratification.

If a dual injection system with argon as a working fluid is applied then the system's role would be to mitigate the air ingress oxidation potential for the first minutes of its operation (HTTF case) until air is completely removed from the lower plenum. After 60 sec of the simulation with active mitigating system, volume average mass fraction of air in the lower plenum is reduced to 2.0%. After that time, injecting additional portions of cold gas prevents the hazardous D-LOFC consequences by blocking air from entering the lower parts of the reactor components and lowering the temperature of the reactor system.

The results for the mitigation method sensitivity analysis and implementation, presented in this dissertation, should be considered as preliminary because they are based on particular assumptions with respect to the assumptions made on the baseline model (exchange flow simulation): geometry simplification, porous body models, simulation of 'pure' stratified flow phase without influence of the depressurization stage, and no heat transfer contribution, etc. However, analyses provide valuable insight into the potential of the mitigation application and its efficiency to avoid consequences of the DEGB in the VHTR reactor.

The single CFD simulation without the depressurization phase took about 3 weeks (time step=0.025 sec) to receive results for 30 sec of a single transient case, using 16 parallel CPUs. Therefore, it should be underlined that the CFD simulation of exchange flow phenomena in a full-scale reactor model would be much longer and require powerful computational resources.

9. Future work

Even though obtained results point direction for exact modeling of the mitigation concept, several further steps are recommended to be investigated before method implementation:

1. Detailed lower plenum and core models application in the CFD model.
2. System structural analysis with active lower plenum injection.
3. Exact influence of depressurization phase on the subsequent D-LOFC stages.
4. Investigation of mitigation system operation during extended period of time that will include molecular diffusion and natural circulation in the reactor core.
5. Validation of baseline results with results from the HTTF facility experiments.
6. Detailed system design of the proposed mitigation method.
7. Mitigation concept implementation on the HTTF and its validation.

If all above recommendations would be fulfilled, then final mitigation concept for the MHTGR can be established and successfully implemented in the commercial design.

References

1. Anderson N. A., 2006, *Coupling RELAP5-3D and FLUENT to Analyze a Very High Temperature Reactor (VHTR) Outlet Plenum*, Master Thesis, Texas A&M University.
2. Ball S., 2006, *Sensitivity studies of modular high-temperature gas-cooled reactor postulated accidents*, Nuclear Engineering and Design, 236, pp. 454–462.
3. Ball S., Richards M., Shepelev S., 2008, *Sensitivity Studies of Air Ingress Accidents in Modular HTGRs*, Nuclear Engineering and Design, 238, pp. 2935-2942.
4. Ben-Dor G., Igra O., Elperin T., 2001, *Handbook of Shock Waves, Volume 1*, Academic Press.
5. Benjamin, T. B., 1968, *Gravity Currents and Related Phenomena*, Journal of Fluid Mechanics, 31, part 2, pp. 209-243.
6. Boer B., Kloosterman J. L., Damian F., Peniguel C., 2008, *Assessment of VHTR Core Design with Regard to Fuel Temperature Loss of Forced Cooling Conditions*, RAPHAEL Report, European Commission..
7. Brudieu M., Kadak A. C., 2006, *Blind Benchmark Predictions of Nacok Air Ingress Tests Using Computational Fluid Dynamics*, Proceedings HTR2006: 3rd International Topical Meeting on High Temperature Reactor Technology, Johannesburg, South Africa.
8. Cadell S. R., 2012, *Development of a Binary Mixture Gas Composition Instrument for Use in a Confined High Temperature Environment*, Doctoral Thesis, Oregon State University.
9. CD-adapco, STAR-CCM+ Version 6.04.014 User Guide.
10. Celik I. B., Ghia U., Roache P. J., Freitas C. J., Coleman H. W., Raad P. E., 2008, *Procedure for Estimation and Reporting of Uncertainty Due to Discretization in CFD Applications*, ASME Journal of Fluids Engineering, 130(7), pp.078001.

11. Corson J. R., 2010, *Development of MELCOR Input Techniques for High Temperature Gas-Cooled Reactor Analysis*, Master Thesis, Texas A&M University.
12. Davis C., Siefken L., Oh Chang H., 2005, *Assessment of RELAP5-3D for Analysis of Very High Temperature Gas-Cooled Reactors*, NURETH-11.
13. Dos Santos Nogueira H. I., 2013, *Experimental Characterization of Unsteady Gravity Currents Developing over Smooth and Rough Beds*, PhD Thesis, University of Coimbra.
14. El-Genk M. S., Tournier J-M. P., 2012, *Validation of gasification model for NBG-18 nuclear graphite*, Nuclear Engineering and Design, 250, pp. 142-155.
15. El-Genk M. S., Tournier J-M. P., 2013, *Transient gasification in an NBG-18 coolant channel of a VHTR prismatic fuel element*, Progress in Nuclear Energy, 64, pp. 16-30.
16. El-Genk M. S., Tournier J-M. P., Travis B. W., 2012, *Graphite Oxidation Simulation in HTR Accident Conditions*, Final and 3rd Year Technical Report, Institute of Space and Nuclear Power Studies, New Mexico.
17. Epiney A., Mikityuk K., Chawla R., 2010, *Heavy-gas injection in the Generation IV gas-cooled fast reactor for improved decay heat removal under depressurized conditions*, Nuclear Engineering and Design, 240, pp. 3115-3125.
18. Ferng Y. M., Chi C.W., 2012, *CFD Investigating the Air Ingress Accident Occurred in a HTGR Simulation of Thermal-hydraulic Characteristics*, Nuclear Engineering and Design, 245, pp. 28-38.
19. Fuller E. L., Okoh J. M., 1997, *Kinetics and Mechanisms of the Reaction of Air with Nuclear Grade Graphite: IG-110*, Journal of Nuclear Materials, 240, pp. 69-72.
20. Gao Z. H., Xu J. J., Qian Y. H., Li M. S., 2014, *Effects of Surface Temperature, Flow Velocity and Ambient Pressure on the Oxidation of Graphite at 1400°C-200°C in O₂*, Corrosion Science, 78, pp. 269-275.

21. General Atomics Energy Multiplier Module Technical Fact Sheet, online access: 04/30/2013,
<http://www.ga.com/docs/em2/pdf/FactSheetTechnicalFactSheetEM2.pdf>
22. General Atomics, 1996, Gas-Turbine Modular Helium Reactor (GT-MHR) Conceptual Design Description Report, Project No. 7658, San Diego.
23. Generation IV International Forum, 2002, *Generation IV Roadmap: R&D Scope Report for Gas-Cooled Reactor Systems*, GIF-004-00.
24. Generation IV International Forum, 2002, *A Technology Roadmap for Generation IV Nuclear Energy Systems*, GIF-002-00.
25. Generation IV International Forum, *Generation IV Roadmap: Description of Candidate Gas-cooled Reactor Systems Report. Appendix C: Very-High-Temperature Reactor (VHTR) Systems Summary Report*, GIF-016-00.
26. Haque H., 2008, *Consequences of Delayed Air Ingress Following a Depressurization Accident in a High Temperature Reactor*, Nuclear Engineering and Design, 238, Issue 11, pp. 3041-3046.
27. Hishida, M., Fumizawa, M., Takeda, T., Ogawa, M., Tekenaka, S., 1993, *Researches on Air Ingress Accidents of the HTTR*, Nuclear Engineering and Design, 144, pp. 317-325.
28. Hishida, M., Takeda, T., 1991, *Study on Air Ingress During an Early Stage of a Primary-Pipe Rupture Accident of a High-Temperature Gas-Cooled Reactor*, Nuclear Engineering and Design, 126, pp. 175-187.
29. Huang W. H., Tsai S. C., Chiu I. C., Chen C. H., Kai J. J., 2014, *The Oxidation Effects of Nuclear Graphite During Air-ingress Accident*, Nuclear Engineering and Design, 271, pp. 270-274.
30. Incropera F. P, DeWitt D. P., 1981, *Fundamentals of Heat Transfer*, John Wiley & Sons.

31. International Atomic Energy Agency, 2001, *Current Status and Future Development of Modular High Temperature Gas Cooled Reactor Technology*, ISSN 1011-4289.
32. International Energy Agency, 2014, *Key World Energy Statistics*, Report, France.
33. Janse van Rensburg J. J., Kleingeld M., 2011, *An integral CFD approach for the thermal simulation of the PBMR Reactor Unit*, Nuclear Engineering and Design, 241, pp. 3130– 3141.
34. Janse van Rensburg J.J., Kleingeld M., 2011, *CFD applications in the Pebble Bed Modular Reactor Project: a decade of progress*, Nuclear Engineering and Design, 241, pp. 3683– 3696.
35. Keller, J. J. and Chyou, Y. P., “*On the Hydraulic Lock-Exchange Problem*,” Journal of Applied Mathematics and Physics, Vol. 41, 1991.
36. Kim E. S., No H. C., 2006, *Experimental Study on the Oxidation of Nuclear Graphite and Development of an Oxidation Model*, Journal of Nuclear Materials, 349, pp. 182-194.
37. Kim E. S., No H. C., Kim B. J., Oh C. H., 2008, *Estimation of Graphite Density and Mechanical Strength Variation of VHTR During Air-ingress Accident*, Nuclear Engineering and Design, 238, pp. 837-847.
38. Kim E. S., No H. C., Kim B., Oh C. H., 2007, *Estimation of Graphite and Mechanical Strength Variation of VHTR during Air Ingress Accident*, Nuclear Engineering and Design, 238.
39. Kim S., Yadav M. S., Talley J. D., Ireland A., Bajorek S. M., 2013, *Separate effects experiments for air-ingress in helium filled vessel*, Experimental Thermal and Fluid Science, 49, pp. 1-13.
40. Kundu K., Cogen I. M., 2004, *Fluid Mechanics*, Third Edition, Elsevier.

41. Kunitomi K., Katanishi S., Takada S., Takizuka T., Yan X., 2004, *Japan's Future HTR – the GTHTTR300*, Nuclear Engineering and Design, 233, Issues 1-2, pp. 309-327.
42. Lemmon E. W., Jacobsen R. T., Penoncello S. D., Friend D. G., 2000, *Thermodynamic Properties of Air and Mixtures of Nitrogen, Argon and Oxygen from 600 K to 2000 K at Pressures to 2000 MPa*, Journal of Physical and Chemical Reference Data, 29, pp. 331-385.
43. Libby P. A., 1996, *Introduction to Turbulence*, Taylor & Francis.
44. Lowe R. J., Rottman J. W., Linden P. F., 2005, *The non-Boussinesq lock exchange problem. Part 1. Theory and Experiments*, Journal of Fluid Mechanics, 537, pp. 101-124.
45. Magnussen, J., 2011, *Pressurized Effects on Density-Difference Driven Stratified Flow: CFD Model of a DCC Even in the HTGR*, M.S. Thesis, Oregon State University.
46. Marsh, H. (1989). *Introduction to Carbon Science*. London, UK. Butterworths.
47. Martineau R. C., Berry R. A., 2009, *A Preliminary Investigation of Rapid Depressurization Phenomena Following a Sudden DLOFC in a VHTR*, INL/EXT-09-15634.
48. Maruyama S., Fujimoto N., Sudo Y., Murakami T., Fujii S., 1994, *Evaluation of Core Thermal and Hydraulic Characteristics of HTTR*, Nuclear Engineering and Design, 152, Issues 1-3, pp. 183-196.
49. McCarty R. D., 1973, *Thermodynamic Properties of Helium 4 from 2 to 1500 K at Pressures to 10^8 Pa*, Journal of Physical and Chemical Reference Data, 2, pp. 923-1041.
50. Mears L. D., Goodjohn A. J., 1989, *The Status of High-Temperature Gas-Cooled Reactor Development and Design*, IAEA Bulletin, 3.

51. Mok K. M., Jeong K.K, Yeh H., 2003, *Experimental Observations of the Flow Structures at Gravity Current Fronts*, International Conference on Estuaries and Coasts November 9-11, Hangzhou, China.
52. Neylan A. J., 1986, *The Modular High-Temperature Gas-Cooled Reactor (MHTGR)*, GA Technologies, Technical Committee Meeting on Gas-Cooled Reactors and Their Applications, Germany.
53. Nogueira H. I. S., Adduce C., Alves E., Franca M. J., 2013, *Analysis of Lock-exchange Gravity Currents Over Smooth and Rough Beds*, Journal of Hydraulic Research, 51, No. 4, pp. 417–431.
54. Oh Chang H., Davis C., Siefken L., Moore R., No H. C., Kim J., Park G. C., Lee J. C., Martin W. R., 2006, *Development of Safety Analysis Codes and Experimental Validation from a Very High Temperature Gas Cooled Reactor*, Final Report, Idaho National Laboratory, INL/EXT-06-01362.
55. Oh Chang H., Kang H. S., Kim E. S., 2011, *Air-ingress analysis: Part 2—Computational fluid dynamic models*, Nuclear Engineering and Design, 241, pp. 213–225.
56. Oh Chang H., Kim E. S., 2010, *Isothermal Air Ingress Validation Experiments at Idaho National Laboratory: Description and Summary of Data*, INL/EXT-10-19727.
57. Oh Chang H., Kim E. S., 2010, *Validations of CFD Code for Density-Gradient Driven Air Ingress Stratified Flow*, ICONE 18-29807, pp. 201-209.
58. Oh Chang H., Kim E. S., 2012, *Conceptual Study on Air Ingress Mitigation for VHTRs*, Nuclear Engineering Design, 250, pp. 448-464.
59. Oh Chang H., Kim E. S., Kang H. S., 2012, *Natural Circulation Patterns in the VHTR Air-ingress accident and Related Issues*, Nuclear Engineering and Design, 249, pp. 228–236.

60. Oh Chang H., Kim E. S., No H. C., Cho N. Z., 2008, *Experimental Validation of Stratified Phenomena, Graphite Oxidation, and Mitigation Strategies of Air Ingress Accidents*, INL/EXT-08-14840.
61. Oh Chang H., Kim E. S., No H. C., Cho N. Z., 2011, *Final Report on Experimental Validation of Stratified Flow Phenomena, Graphite Oxidation, and Mitigation Strategies of Air Ingress Accidents*, Idaho National Laboratory, Report INL/EXT-10-20759.
62. Oh Chang H., Kim E. S., Schultz R., Petti D., Kang H. S., 2009, *Computational Fluid Dynamics Analyses on Very High Temperature Reactor Air Ingress*, INL/CON-09-15336.
63. Oh Chang H., Kim E. S., Schultz R., Petti D., Liou C. P., 2008, *Implications of Air Ingress Induced by Density-Difference Driven Stratified Flow*, INL/CON-08-13821.
64. Oh Chang H., Kim E., Kim J., Schultz R., Petti D., 2009, *Effect of Reacting Surface Density on the Overall Graphite Oxidation Rate*, ICAPP 2009, preprint.
65. Oh Chang H., Kim E.S., 2010, *Air Ingress Analysis: Computation Fluid Dynamic Models*, Idaho National Laboratory.
66. Oh Chang H., Kim E.S., 2011, *Air Ingress Analysis: Part 1.Theoretical Approach*, Nuclear Engineering and Design, 241, pp. 203–212.
67. Oh Chang H., Moore, R. L., Merrill B. J., Petti D. A., 2001, *Air Ingress Analyses on a High Temperature Gas-Cooled Reactor*, ASME International Mechanical Engineering Congress and Exhibition.
68. *Preliminary Safety Information Document for the Standard MHTGR*, 1992, HTGR-86024, Rev. 13, Stone & Webster Engineering Corp.
69. *Probabilistic Risk Assessment for the Standard Modular High Temperature Gas Cooled Reactor*, 1988, DOE HTGR 8601 Rev 5 General Temperature, General Atomics.
70. Rathakrishnan E., 2010, *Applied Gas Dynamics*, John Wiley & Sons.

71. Reyes J. N., Groome J. T, Woods B. G, Jackson B., Marshall T.D., 2010, *Scaling Analysis for the High Temperature Gas Reactor Test Section (GRTS)*, Nuclear Engineering and Design, 240, pp. 397-404.
72. Riemke R., Davis C., Schultz R., 2006, *RELAP5-3D Code Includes ATHENA Features and Models*, ICONE 14-89217.
73. Roache P. J., 1988, *Verification and Validation in Computational Science and Engineering*, Hermosa, Albuquerque.
74. Schultz R., 2007, *Next Generation Nuclear Plant Methods Technical Program Plan*, INL/EXT-06-11804.
75. Schultz R., 2008, *Meeting the Thermal-Hydraulic Analysis Needs for Advanced Gas Reactor Systems*, Proceedings of the 4th International Topical Meeting on HTR Technology, Washington DC, USA.
76. Schultz R., Bayless P. D., Johnson R. W., McCreery G. E., Tartano W., Wolf J. R., 2010, *Studies Related to the Oregon State University High Temperature Test Facility: Scaling, the Validation Matrix, and Similarities to the Modular High Temperature Gas-Cooled Reactor*, INL/EXT-10-19803.
77. Shin J. O., Dalziel S. B., Linden P. F., 2004, *Gravity Currents Produced by Lock Exchange*, Journal of Fluid Mechanics, 521, pp. 1-34.
78. Shropshire D. E., Stephen Herring J., 2004, *Fuel-Cycle and Nuclear Material Disposition Issues Associated with High-Temperature Gas Reactors*, ANES 2004, Miami Beach, Florida.
79. Simpson J. E., 1982, *Gravity Currents in the Laboratory*, Atmosphere and Ocean, Annual Reviews of Fluid Mechanics, 14, pp. 213-234.
80. Sun X., 2009, *Investigation of Countercurrent Helium-air Flows in air Ingress Accidents for VHTRs*, Reactor Concepts RD&D, U.S Department of Energy.

81. T. Takeda., 2004, *Research and Development on Prevention of Air Ingress during the Primary-Pipe Rupture Accident in the HTTR*, Nuclear Engineering Design, 233, pp. 197-209.
82. Takeda T., 1997, *Air Ingress Behavior During a Primary-pipe Rupture Accident of HTGR*, JAERI- 1338, Japan Atomic Energy Research Institute.
83. Takeda T., Hishida M., 2000, *Study on the Passive Safe Technology for the Prevention of Air Ingress During the Primary Pipe Rupture Accident of HTGR*, Nuclear Engineering and design, 200, pp. 251-259.
84. Takeda T., Nomura M., Yanagawa N., Funatani S., 2014, *Study on control method of natural circulation by injection of helium gas*, Nuclear Engineering and Design, 271, pp. 417-423.
85. The American Society of Mechanical Engineers, 2009, *Standard for Verification and Validation in Computational Fluid Dynamics and Heat Transfer*, American National Standard, ASME V&V 20-2009.
86. Todreas N. E., Kazmi M. S., 1990, *Nuclear Systems I Thermal Hydraulic Fundamentals*, Hemisphere Publishing Corporation.
87. Tu J., Yeoh G. H., Liu C., 2008, *Computational Fluid Dynamics*, Elsevier.
88. Turner J. S., *Buoyancy Effects in Fluids*, 1973, Cambridge Monographs on Mechanics and Applied Mathematics, Cambridge University Press, pp. 70-74.
89. United States Nuclear Regulatory Commision, 2008, *Next Generation Nuclear Plant Phenomena Identification and Ranking Tables (PIRTs) Volume 2: Accident and Thermal Fluids Analysis PIRTs*, NRC Library, <http://www.nrc.gov/reading-rm.html>, online access: 05/27/2015.
90. United States Nuclear Regulatory Commision.2007, *Next Generation Nuclear Plant Phenomena Identification and Ranking Tables (PIRTs) Volume 1: Main Report*, NRC Library, <http://www.nrc.gov/reading-rm.html>, online access: 05/27/2015.

91. Utberg Jr., J. E., 2013, *Nitrogen Concentration Sensitivity Study of the Lock Exchange Phenomenon in the High Temperature Test Facility*, M.S. Thesis, Oregon State University.
92. Vafai K., 2005, *Handbook of porous media*, Second Edition, Taylor & Francis.
93. VHTR Cooperative Agreement, 2009, *Phenomena Identification and Ranking*, Program Review Meeting, Oregon State University.
94. Vilim R. B., Feldman E. E., Pointer W. D., Wei T. Y. C., 2004, *Initial VHTR Accident Scenario Classification: Models and Data, Status Report*, Nuclear Engineering Division, Argonne National Laboratory.
95. Von Karman, T., "The Engineer Grapples with Nonlinear Problems," Bull. Am. Math. Soc., Vol. 46, 1940, pp.615–683.
96. Whites F., 2006, *Fluid Mechanics*, McGraw-Hill Companies; 6th edition.
97. Windes W., Strydom G., Smith R., Kane J., 2014, *Role of Nuclear Grade Graphite in Controlling Oxidation in Modular HTGRs*, Idaho National Laboratory Report.
98. Xiaowei L., Jean-Charles R., Suyan Y., 2004, *Effect of Temperature on Graphite Oxidation Behavior*, Nuclear Engineering and Design, 227, pp. 273-280.
99. XiaoWei L., XiaoTian L., Li S., ShuYan H., 2011, *Transient pressure analysis for the reactor core and containment of a HTGR after a primary loop pressure boundary break accident*, Chinese Science Bulletin, Vol. 56, No. 23, pp. 2486–2494.
100. Yan, X. L., Takeda, T., Nishihara, T., Ohashi, K., Kunitomi, K., Tsuji, N., 2008, "A Study of Air Ingress and Its Prevention in HTGR," Nuclear Technology, 163.
101. Yih S., Guha C. R., *Hydraulic Jump in a Fluid System of Two Layers*, Wiley Online Library, access online: 04/30/2013, <http://onlinelibrary.wiley.com>.
102. Yurko J. P., (2010), *Effect of Helium Injection on Diffusion Dominated Air Ingress Accidents in Pebble Bed Reactors*, Master of Science, Massachusetts Institute of Technology.

103. Zhai T., 2003, *LOCA and Air Ingress Accident Analysis of a Pebble Bed Reactor*, Master of Science Thesis in Nuclear Engineering at the Massachusetts Institute of Technology.
104. Zuber, N. (1991). "Appendix D: Hierarchical, Two-Tiered Scaling Analysis." An Integrated Structure and Scaling Methodology for Severe Accident Technical Issue Resolution (NUREG/CR-5809).



This work of this dissertation was supported by the INSPE Project: Innovative Nuclear and Sustainable Power Engineering. INSPE project has been co-financed by the European Social Fund.